Winter 2005

Melting and Solidification Study of Indium and Bismuth Nanocrystals Using Reflection High-Energy Electron Diffraction

Mohamed K. Zayed
Old Dominion University

MELTING AND SOLIDIFICATION STUDY OF INDIUM AND

BISMUTH NANOCRYSTALS USING REFLECTION HIGH-

ENERGY ELECTRON DIFFRACTION

By

Mohamed K. Zayed

A Dissertation Submitted to the Faculty of Old Dominion University in
Partial Fulfillment of the Requirement for the Degree of

DOCTOR OF PHILOSOPHY

ELECTRICAL ENGINEERING

OLD DOMINION UNIVERSITY

December 2005

Approved by:

Hani E. Elsayed-Ali (Director)

Karl H. Schoenbach (Member)

Mounir Laroussi (Member)

Svetozar Popovic (Member)

ABSTRACT

MELTING AND SOLIDIFICATION STUDY OF INDIUM AND BISMUTH NANOCRYSTALS USING REFLECTION HIGH-ENERGY ELECTRON DIFFRACTION

Mohamed K. Zayed
Old Dominion University, 2005
Director: Dr. Hani E. Elsayed-Ali

As technology begins to utilize nanocrystals for many chemical, biological, medical, electrical, and optoelectrical applications, there is a growing need for an understanding of their fundamental properties. The study of melting and solidification of nanocrystals is of interest to fundamental understanding of the effect of reduced size and crystal shape on the solid-liquid phase transition. Melting and solidification of as-deposited and recrystallized indium and bismuth nanocrystals were studied using reflection high-energy electron diffraction (RHEED). The nanocrystals were thermally deposited on highly oriented 002-graphite substrate at different deposition temperatures. The growth dynamics of the nanocrystals was studied using *in situ* RHEED while the morphology and size distributions were studied using *ex situ* real image technique (atomic force microscopy (AFM) or scanning electron microscopy (SEM)). RHEED observation during deposition showed that 3D nanocrystals of indium are directly formed from the vapor phase within the investigated temperature range, 300 K up to 25 K below the bulk melting point of indium. On the other hand, bismuth condensed in the form of supercooled liquid droplets at temperatures above its maximum supercooling point, 125 K below the bulk melting point of bismuth. Below the maximum supercooling point, bismuth condensed in the solid phase. Post deposition real images showed that the formed nanocrystals have morphologies and size distributions that depend on the

deposition temperature, heat treatment, and the amount of the deposited material. As-deposited nanocrystals are found to have different shapes and sizes, while those recrystallized from melt were formed in similar shapes but different sizes.

The change in the RHEED pattern with temperature was used to probe the melting and solidification of the nanocrystals. Melting started early before the bulk melting point and extended over a temperature range that depends on the size distribution of the nanocrystals. Nanocrystals at the lower part of the distribution melt early at lower temperatures. With the increase in temperature, more nanocrystals completely melt with the thickness of the liquid shell on the remaining crystals continuing to grow. Due to size increase after melting, recrystallized bismuth nanocrystals showed a melting range at temperatures higher than that of as-deposited. However, recrystallized indium nanocrystals showed an end melting point nearly equal to that of the recrystallized ones except for the 1.5-ML film which showed an end melting point ~10 K higher than that of as-deposited. Within the investigated thickness range, all nanocrystals were completely melted below or at the bulk melting point without observed superheating. The characteristic melting point of the nanocrystal ensemble, the temperature at which the rate of their melting with temperature is the highest, showed a linear dependence on the reciprocal of the average crystal radius, in accordance with different phenomenological theoretical models. During solidification, all nanocrystals showed supercooling relative to their melting point and to the bulk melting point. For Bi, the amount of liquid supercooling was found to decrease linearly with the reciprocal of the average crystallite size.

ACKNOWLEDGMENTS

I would like to express my gratitude and appreciation to my research advisor, Dr. Hani Elsayed-Ali for his constant supports, guidance, and encouragement. His vast knowledge, scientific understanding, and research expertise added considerably to my graduate experience. I would like also to thank the members of my Ph.D. committee, Dr. Karl Schoenbach, Dr. Mounir Laroussi, and Dr. Svetozar Popovic, for their help and support.

During my stay in Norfolk, Virginia and my work at the Physical Electronics Research Institute (PERI), I met with many people who became an extended family to my family in Egypt. I thank all of them and I acknowledge their friendships. I also would like to thank all my colleagues and friends either at PERI laboratories or back home in Bani-Swaif Egypt. Many thanks go to Mr. Mohamed S. Hegazy for his discussion and suggestions during my thesis work.

Also, I would like to thank my family for the support they provided me through my entire life. Words fail to express my deep gratitude to my mother whose love and prayers were the only wings to fly me to USA. I would not be who I am today without the endless love she offered and the sacrifices she made.

I am sincerely thankful and grateful to my wonderful wife for all the effort and the sacrifices she made during the years I spent working on my dissertation. Her endless patience, magnificent support, and wise understanding was essential for this work to be achieved.

Finally, this dissertation is dedicated to my beloved daughter, Mennah, and my son, Saifullah.

TABLE OF CONTENT

LIST OF FGURES

CHAPTER I

INTRODUCTION*

Over the past decades, there has been an increased interest in investigating the fundamental physical and chemical properties of nanometer-sized crystals [1-4]. As technology begins to utilize nanocrystals for many chemical, biological, medical, electrical and optoelectrical applications, there is a growing need for an understanding of their fundamental properties [2,5,6]. Moreover, understanding the fundamental properties of nanocrystals is essential from a fundamental point of view as well as for several applications [1-4]. Since nanocrystals show properties that are different from ther corresponding bulk, the size dependent study of these properties gives an idea about how these properties evolve to those of the bulk as the size approaches a macroscopic scale [4]. This knowledge would increase the control over the material properties by controlling their sizes, and hence design materials with optimal properties that satisfy industrial and other technical needs [6-8].

The thermodynamics of the melting and solidification phase transitions is among the properties that are significantly affected by the crystal size [9-12]. On the opposite to bulk melting, which is considered as a first order transition, melting and solidification of nanometer-size crystal suggests a continuum-melting scenario and/or a presence of meta-stable states during the transition [13,14]. While surface pre-melting is favorable for large particles, continuum melting through formation of hexatic states, liquid-like and solid-like, is favorable for lower size crystals and two-dimensional islands [15,16]. In general, as the crystal size is reduced, the first-order phase transition nature of the bulk melting

---

* The reference model of this work follows the SPIE format.

becomes indistinct and the process spreads over a finite temperature range [13-15]. Moreover, the melting point and the latent heat of fusion also significantly decrease [17,18]. When the size gets small enough, the melting point undergoes strong non-monotonic variations with size [19,20]. Geometrical shell, stable geometrical structural configuration, and electronic shell, stable structures correspond to complete electron shells analogous to those responsible for the stability and inertness of rare gases, and may form clusters of exceptional stability and hence, local maximum melting points could occur [21]. However, sodium clusters showed a melting point that has an irregular variation with the number of atoms within the cluster in a pattern that has not yet been interpreted and leaves an open question [20]. In spite of these complications, melting and solidification studies of nanometer-size crystals offer an opportunity to understand the finite-size analogue of the bulk first-order phase transition, and hence, explore any stable and meta-stable states that might exist during the transitions. Much effort is needed before a clear understanding of that process is achieved.

It is generally believed that the surface plays an important role in determining the melting behavior of small and large crystals [22-24]. At a temperature below the bulk melting point, T_0, defect free solids start to show a liquid-like layer at the surface, which acts as a nucleation site from which the melt propagates throughout the crystal [24]. Due to the effect of surface melting and the finite size, the melting point of nanometer-sized crystals is expected to be lower than that of the bulk. However, suppressing surface melting of a solid crystal by coating with, enclosing by, or embedding in another higher melting point material not only prevents the melting point depression, but also drives the material to superheat above its equilibrium melting point [25-27]. Moreover, due to

surface energy anisotropy of solid crystals, surface melting has an orientation dependent behavior [28]. Based on the surface orientation, the crystal may show surface melting, incomplete melting or crystal superheating. Close packed structures or high packed crystal surfaces such as fcc(111) remain completely solid up to T_m and can even superheat to a temperature above T_m [29-31]. Small crystals bounded by non-melting or close packed facets also show superheating for an extended amount of time [32,33]. In fact, the shape and the surfaces or interfaces of the particles with the host material or with the substrate determine the melting and solidification behavior of the nanocrystals [32-36]. For nanocrystals deposited on an inert substrate, the melting behavior is determined mainly by the external surface orientation and morphology of the nanocrystal. Nanocrystals with low external energy facets show maximum stability and higher surface melting nucleation barrier as in the extensive {111} faceted platelet shaped crystals [35]. On the other hand, high external energy shaped crystals favor surface melting formation, and hence show melting point depression.

With the goal of designing materials with specific property, nanotechnology seeks preparation techniques that offer size control with low cost [1,5,6]. The appropriate preparation technique can be selected based on the nature/type of the nanocrystals and on the specific applications that these nanocrystals are prepared for [37]. There are different techniques that have been employed to prepare nanocrystals, either as an assembly, nanoparticles incorporated in a host matrix, or nanostructure components. These methods can be categorized as direct deposition, mechanical milling, chemical methods, and gas aggregation methods [37,38]. Mechanical milling is suitable for commercial production of nanoparticle powders of a single or composite material for industrial applications [39].

It is also suitable for preparing nanometer-sized crystals embedded in a host matrix for the study of fundamental properties [38,40]. Chemical techniques such as sol-gel, electrochemical, spray pyrolysis and other solution-based methods have been used extensively for inexpensive and easy preparation of metallic, semiconductor, and organic assembled nanocrystals [41-43]. In these techniques, normally the nanocrystals are prepared and studied in two different chambers. Formation of an oxide layer or ambient contamination, which will alter the intrinsic properties of the nanocrystals, is possible when the nanocrystal are transferred to the testing chamber. Therefore, it is of considerable importance to prepare and study these nanocrystals *in situ* in ultrahigh vacuum in a clean environment. Conventional deposition techniques such as molecular beam epitaxy (MBE), chemical and physical vapor deposition (CVD and PVD) and pulsed laser deposition are good techniques for the preparation of nanocrystals and quantum dot structures. Atomic deposition techniques including ionized beam deposition, high-energy cluster beam deposition and low energy cluster beam deposition are methods that are used effectively to deposit size selective atomic clusters [3,44].

While many techniques are now known to produce nanostructures, there are quite few that are involved in characterizing and measuring the melting and solidification properties of such small collections of atoms. Transmission electron microscopy (TEM) is a standard technique for studying the structural and melting properties of nanometer-sized crystals [16,45]. Using this technique, the melting temperature of nanocrystals is monitored by the loss of crystalline structure with increasing temperature. The size-dependent melting property of a thermally deposited assembly of nanocrystals can be studied by monitoring clusters with different sizes. In a different approach, dark field

microscopy is used to determine the melting point of individual particles by noting the temperature at which the dark field image greatly dims [32-35]. However, the high-energy beam used in these techniques may influence the melting process or introduce an uncertainty in measuring the sample temperature [45]. X-ray diffraction was used for melting and solidification studies of nanometer-sized metallic particles [46]. Peak intensity variations with temperature as well as the line profile changes with temperature were used to monitor the melting of the small particles. The difficulty in using this method is the determination of the particle size distribution, especially for the smaller particles. Electron diffraction was also used to study the melting and solidification of thermally evaporated island films deposited on carbon substrates [47,48]. By monitoring the integral intensity of one of the diffraction patterns as a function of temperature, the film melting point was measured. *Ex situ* real image technique is normally used along with diffraction technique to study the size-dependent melting. Differential scanning calorimetry (DSC) is another technique used to investigate solid-liquid transitions of nanocrystals and clusters [17-19]. Using DSC, the heat capacity and the latent heat of fusion of the deposited nanocrystals were directly measured as a function of temperature. Also, a technique based on laser irradiation of free metal clusters produces calorimetric data not affected by substrate influence or by the environment was also used [17]. Other non-conventional techniques such as electric field emission and γ–γ correlation, Raman spectroscopy were used to study the nanocrystal melting [49-51].

RHEED is among the more powerful techniques that are used to study surface phase transitions as well as melting and solidification of nanocrystals. RHEED is a sensitive surface-structural tool suitable for studying surface dynamics. The RHEED

geometry facilitates *in-situ* monitoring during thin film growth and hence mechanisms of surface diffusion, thin film nucleation and growth, and surface phase transitions could be better understood. Based on the surface features, RHEED could be operated in its pure reflection mode or in its transmission reflection mode [52]. The nearly grazing angle characteristic of RHEED makes the beam spread over a few mm^2 of the sample causing negligible localized heating. Because of the transmission nature of the electron diffraction through surface roughness, it is probing the "bulk" structure up to a thickness corresponding to the electron inelastic mean free path (IMFP). By measuring the relative intensity, shape, inclination, and sharpness of the spot or streaks, RHEED patterns can give information about the lateral grain size and the electron penetration depth of a well-textured small-grained polycrystalline thin film [53]. Theoretical interpretation of the diffraction pattern can be used to obtain the shape of islands [54]. Time-resolved RHEED also provides the ability to monitor the evolution of the surface structure, morphology, and temperature during a fast laser-initiated surface phase transition [55]. By monitoring the temporal evolution of the diffraction streak intensity, information is obtained on the mean-square vibrational amplitude of the surface atoms and the structural integrity of the surface.

Few elements are suitable for melting and solidification studies in ultrahigh vacuum (UHV). The element or the compound should have a low partial vapor pressure near the melting point, otherwise the surface will be covered with vapor near the melting point and the crystal can simply evaporate. Moreover, in case of embedded or encapsulated nanocrystals, the observed superheating, if it is found, will be a combination of the equilibrium melting point elevation due to pressure increase inside the cell and the

superheating by surface melting suppression [56]. The former may be dominated if the nanocrystal material has a high vapor pressure near the melting point. Indium and bismuth nanocrystals are chosen for this study because of their reasonable melting points and their extremely low partial vapor pressure near the melting point [24]. A subset of Bi nanocrystals was reported to show few degrees superheating, while the rest showed melting point depressions [34]. Beside the difference in crystallite shape and size distribution, the effect of the preparation and testing techniques on the obtained results is still a question. Also indium is a metallic element compared to bismuth, which is a semi-metallic element. Moreover, bismuth has a negative volume change upon melting; it expands as it is solidified, while indium shows the normal volume increase upon melting.

In this work, melting and solidification of indium and bismuth nanocrystals are studied under the same preparation conditions and with the same investigation technique, RHEED. The nanocrystals are prepared using thermal evaporation in UHV on a highly oriented pyrolytic graphite (HOPG) substrate. Because of unique physical and chemical properties, HOPG surface is chemically inert, generally homogeneous, easily prepared, and usually free of extrinsic defects [57]. Ex-situ real images such as scanning electron microscope (SEM) and atomic force microscope (AFM) are used to study the crystal shape and size of the deposited indium and bismuth nanocrystals. The normalized intensity of a selected RHEED spot as a function of temperature is used to monitor the melting and solidification of the nanocrystals. The mechanisms by which such small collections of atoms melt and solidify are discussed. The supercooling and the possibility of superheating of the nanocrystals are also studied.

As-deposited nanocrystals may show unusual crystal morphologies as a result of the substrate interaction, the preparation conditions, crystal size, or annealing treatments. Recrystallized nanocrystals can have shapes and external surface morphologies that differ from the as-deposited nanocrystals, and hence, have different melting and solidification behaviors. The melting and solidification of as-deposited nanocrystals is investigated relative to those recrystallized from melt. After deposition, equilibrium shaped nanocrystals are formed by recrystallizing from melt, i.e. the film is heated to a temperature above the equilibrium melting point and slowly cooled down to a temperature below its supercooling temperature. As-deposited samples are investigated immediately after preparation without any heat treatment. The effects of crystal size and crystal shape on the melting of nanocrystals are studied.

The thesis is organized in six chapters including this introductory chapter. Chapter two gives a theoretical background covering the basic physics and fundamental theories of bulk melting, surface melting, and melting of small particles. Theories of heterogeneous and homogenous solidification as well as the phenomena of superheating and supercooling are also briefly reviewed in this chapter. Chapter three gives the experimental and basic foundations necessary to understand and interpret RHEED patterns. The variation of RHEED intensity in dynamic processes that occur during film growth and during surface phase transition is also mentioned in chapter 3. The results on the melting and solidifications studies of indium and bismuth nanocrystals are presented in chapter 4 and chapter 5, respectively. Although there are only minor differences between the ways these two experiments were done, the experimental methodology is presented in each chapter. Finally, chapter 6 concludes the thesis where the main results

of this work are summarized. The basic calculations for RHEED operated in its pure reflection mode performed for selected graphite, indium, and bismuth surfaces are illustrated in appendix A. Appendix B shows how to use information in chapter 3 to index the transmission-RHEED patterns of indium and graphite. Technical information about the used UHV system, how to operate it, and how to collect and analyze RHEED images are given in appendices C and D.

References of chapter I

[1]   J. Jortner and C. N. R. Rao, "Nanostructured advanced materials: perspectives and directions," Pure Appl. Chem.74, 1491–1506 (2002).

[2]   C. N. R. Rao, G. U. Kulkarni, P. J. Thomas, and P. P. Edwards, "Size-dependent chemistry: properties of nanocrystals," Chem. Eur. J. 8, 28-35(2002).

[3]   P. Jensen, "Growth of nanostructures by cluster deposition: experiments and simple models," Rev. Mod. Phys. 71, 1695-1735 (1999).

[4]   L. D. Marks, "Experimental studies of small particle structures," Rep. Prog. Phys. 57, 603-649 (1994).

[5]   L. Mazzola, "Commercializing nanotechnology," Nature Biotech. 21, 1137-1143 (2003).

[6]   M.-P. Pileni, "Nanocrystals: fabrication , organization and collective properties," C.R. Chimie 6, 965-978 (2003).

[7]   J. D. Budai, C. W. White, S. P. Withrow, M. F. Chisholm, J. Zhu, and R. A. Zuhr, "Controlling the size, structure and orientation of semiconductor nanocrystals using meta-stable phase recrystallization," Nature 390, 384-386 (1997).

[8]   J. Schmelzer, S.A. Brown, A. Wurl, and M. Hyslop, "Finit-size effects in the conductivity of cluster assembled nanostructures," Phys. Rev. Let. 88, 226802-2:1-4, (2002).

[9]   V. M. Samsonov, N. Y. Sdobnyakov, and A. N. Bazulev, "Size dependence of the surface tension and the problem of Gibbs thermodynamics: extension to nanosystems," Coll. and Surf. A: Phys.chem. Eng. Asp. 239, 113-117 (2004).

[10]   Z. L. Wang and J. S. Yin, "Self-assembly of shape-controlled nanocrystals and their *in-situ* thermodynamic properties," Mat. Sci. and Eng. A 286, 39- 47 (2000).

[11]   Q. Jiang, Z. Zhang, and J. C. Li , "Melting thermodynamics of nanocrystals embedded in a matrix," Acta Mater. 48, 4791-4795 (2000).

[12]   Q. Jiang, L. H. Liang, and J. C. Li, "Thermodynamic superheating of low-dimensional metals embedded in matrix," Vacuum 72, 249-255(2003).

[13]   V. N. Ryzhov and E. E. Tareyeva, "Melting in two dimension: first-order versus continues transition," Physica A 314, 396-404 (2002).

[14]   R. Kofman, P. Cheyssac, Y. Lereah, and A. Stella, "Melting of clusters approaching 0D," Eur. Phys. J. D 9, 441-444 (1999).

[15]   S. J. Zhao, S. Q. Wang, D. Y. Cheng, and H. Q. Ye, "Three distinctive melting mechanisms in isolated nanoparticles," J. Phys. Chem. B 105, 12857-12860 (2001).

[16]   M. Mitome, "In-situ observation of melting of fine lead particles by high-resolution electron microscopy," Surf. Sci. 442, L953–L958 (1999).

[17]   M. Schmidt, R. Kusche, W. Kronmüller, B. von Issendorff, and H. Haberland, "Experimental determination of the melting point and heat capacity for a free cluster of 139 sodium atoms," Phys Rev. Lett. 79, 99-102 (1997).

[18]   S. L. Lai, J. Y. Guo, V. Petrova, G. Ramanath, and L. H. Allen, "Size-dependent properties of small tin particles: nanocalorimetric measurements," Phys. Rev. Lett. 77, 99-102 (1996).

[19] Y. Efremov, F. Schiettekatte, M. Zhang, E. A. Olson, A. T. Kwan, R. S. Berry, and L. H. Allen, "Discrete periodic melting point observations for nanostructure ensembles," Phys Rev. Lett. 85, 3560-3563 (2000).

[20] M. Schmidt, R. Kusche, B. von Issendorff, and H. Haberland, "Irregular variations in the melting point of size-selected atomic clusters," Nature 393, 238-240 (1998).

[21] F. Calvo and F. Spiegelmann, "Geometric size effects in the melting of sodium clusters," Phys Rev. Lett. 82, 2270-2273 (1999).

[22] J. G. Dash, "History of the search for continuous melting," Rev. Mod. Phys. 71, 1737-1743 (1999).

[23] J. F. van der Veen, "Melting and freezing at surfaces," Surf. Sci. 433–435, 1-11 (1999).

[24] J. F. van der Veen, B. Pluis, and A. W. D. van der Gon, in *Chemistry and Physics of Solid Surfaces VII*, Springer-Veilag, pp. 455-490 (1988).

[25] F. Banhart, E. Hernández, and M. Terrones, "Extreme superheating and supercooling of encapsulated metals in fullerenlike shells," Phys. Rev. Lett. 90, 185502(1-4) (2003).

[26] L. Zhang, Z. H. Jin, L. H. Zhang, M. L. Sui, and K. Lu, " Superheating of confined Pb thin film," Phys. Rev. Let. 85, 1484-1487 (2000).

[27] J. Zhong, L.H. Zhang, Z. H. Jin, M.L. Sui, and K. Lu, "Superheating of Ag nanoparticles embedded in Ni matrix," Acta Mater. 49, 2897-2904 (2001).

[28]   B. Pluis, A. W. D. van der Gun, J. W. M. Frenken, and J. F. van der Veen, "Crystal-face dependence of surface melting," Phys. Rev. Let. 59, 2678-2681 (1987).

[29]   J. W. Herman and H. Elsayed-Ali, "Time-resolved structural studies of the Low index faces of lead," Phys. Rev. B 49, 4886-4897 (1994).

[30]   E. A. Murphy and H. Elsayed-Ali, "Superheating of Pb(111)," Phys. Rev. Lett. 69, 1228-1231 (1992).

[31]   G. Bilalbegovic, " Structural and meta-stability of superheated Al(111)," Phys. Rev. B 55, 16450-16454 (1992).

[32]   M. Blackman, S. J. Peppiatt, and J.R. Samples, " Superheating of bismuth," Nat. Phys. Sci. 239, 61-62 (1972).

[33]   J. J. Mètois, and J.C. Heyraud, " The overheating of lead crystals," J. Phys. (France) 50, 3175-3179 (1989)

[34]   S. J. Peppiatt, "The melting of small particles. II. bismuth," Proc. R. Soc. Lond. A 345, 401-412 (1975).

[35]   G. D. T. Spiller, "Time-dependent melting and superheating of lead crystallites," Phil. Mag. A 46, 535-549 (1982).

[36]   V. B. Storozhev, "The solid-liquid phase transition of nanoparticles in contact with solid surfaces," Surf. Sci. 397, 170-178 (1998).

[37]   C. N. R. Rao, G. U. Kulkarni, P. J. Thomas, V. V. Agrawal, U. K. Gautam, and M. Ghosh, "Nanocrystals of metals, semiconductors and oxides: novel synthesis and applications," Current Science 85, 1040- 1045 (2003).

[38]   P. Moriarty, "Nanostructured materials," Rep. Prog. Phys. 64, 279-381 (2001).

[39] C. Suryanarayana, "Mechanical alloying and milling," Prog. Mat. Sci. 46, 1-184 (2001).

[40] H. W. Sheng, K. Lu, and E. Ma, "Melting and freezing behavior of embedded nanoparticles in ball-milled Al-10wt%M (M= In, Sn, Bi, Cd, Pb) mixitures," Acta Mater. 46, 5195-5205 (1998).

[41] O. Masala and R. Seshadri, "Synthesis routes for large volume of nanocrystals," Annu. Rev. Mater. Res. 34, 41–81 (2004).

[42] C. B. Murray, Shouheng Sun, W. Gaschler H. Doyle, T. A. Betley, and C. R. Kagan, "Synthesis and characterization of monodisperse nanocrystals and close packed Nanocrystal assemblies," IBM J. Res. & Dev. 45, 47-56 (2001).

[43] K. Okuyama and I.W. Lenggoro, "Preparation of nanoparticles via spray route," Chem. Eng. Sci. 58, 537–547 (2003).

[44] A. Perez, P. Melinon, V. Dupuis, P. Jensen, B. Prevel, J. Tuaillon, L. Bardotti, C. Martet, M. Treilleux, M. Broyer, M. Pellarin, J. L. Vaille, B. Palpant, and J. Lerme, "Cluster assembled materials: a novel class of nanostructured solids with original structures and properties," J. Phys. D: Appl. Phys. 30, 709–721 (1997).

[45] J. M. Howe, T. Yokota, M. Murayama, and W. A. Jesser, "Effects of heat and electron irradiation on the melting behavior of Al–Si alloy particles and motion of the Al nanosphere within," J. Electron Microscopy 53, 107–114 (2004).

[46] K. F. Peters, J. B. Cohen, and Y.-W. Chung, "Melting of Pb nanocrystals," Phys. Rev. B 57, 13430-13438 (1998).

[47] V. P. Skripov, V. P. Koverda, and V. N. Skokov, "Size effect on melting of small particles," Phys. Stat. Sol. A 66, 109-118 (1981).

[48] M. Takagi, "Electron-diffraction study of liquid-solid transition of thin metal Films," J. Phys. Soc. Japan 9, 359 (1954).

[49] R. Wfirschum, "Nuclear spectroscopy of nanocrystalline metals and alloys," Nanostructured Materials. 6, 93-104 (1995).

[50] T. Castro, R. Reifenberger, E. Choi, and R. P. Andres, "Size-dependent temperature of individual nanometer-sized metallic clusters," Phys. Rev. B 42, 8548-8556 (1990).

[51] G. Krausch, T. Detzel, H. N. Bielefeled, R. Fink, B. Luckscheiter, R. Platzer, U. Wöhormann, and G. Schatz, "Growth and melting behavior of thin In films on Ge(100),"Appl. Phys. A 53. 324-329 (1991).

[52] W. Braun, In *Applied RHEED reflection high-energy electron diffraction during crystal growth,*" Springer, Berlin, (1999).

[53] J. W. Hartman, R. T. Brewer, and H. A. Atwater, "Reflection high-energy electron-diffraction analysis of polycrystalline films with grain size and orientation distributions," J. Appl. Phys. 92, 5133-5139 (2002).

[54] H. Hsu and Y.L. Wang, "Electron diffraction profile and size distribution islands on a surface," Chin. J. Phys. 39, 441-452 (2001).

[55] B. Lin and H. Elsayed-Ali, "Temperature dependent reflection electron diffraction study of In(111) and observation of laser induced transient superheating," Surf. Sci. 498, 275-284 (2002).

[56] N. X. Sun, H. Lu, and Y. C. Zhou, "Explanation of the melting behavior of embedded particles; equilibrium melting point elevation and superheating," Phil. Mag. Let. 76, 105-109 (1997).

[57]   G. M. Wang, J. J. BelBruno, S. D. Kenny, and R. Smith, "Interaction of silver adatoms and dimers with graphite surfaces," Surf. Sci. 541, 91-100 (2003).

CHAPTER II

MELTING AND SOLIDIFICATION OF SOLID CRYSTALS

II.1.   Introduction

Melting and solidification are of the most ubiquitous first order phase transitions in nature that have been extensively studied by both theory and experiment [1-12]. In spite of the tremendous work published over the past decades, questions, arguments, and controversies, in some cases, are indistinctively clarified [4-8]. Superheating and supercooling are often observed, despite being a reversible first order transition of unique transition point [9-12]. While observations of superheated solid crystals are rare, supercooling of liquid melt is quite common. Also, the amount of superheating, if it is found, is not equal to the supercooling amount. The asymmetric solid-liquid transition behavior in the bulk crystals and its behavior in nanometer-sized clusters, as well as the formulation of an atomic scale comprehensive theory still need a consolidate theoretical and experimental effort before a clear and deep understanding is achieved.

This chapter briefly reviews the theoretical foundation of the solid-liquid phase transition in its forward and backward (melting and solidification) directions. Fundamental theories of bulk melting, surface melting, and melting of small particles are discussed. Theories of heterogeneous and homogenous solidification as well as the phenomena of superheating and supercooling are also presented.

II.2.   Melting of solid crystals

Melting is the transformation of the material from the solid to the liquid state at a specific point of temperature and pressure. Across the transition region, the system

absorbs a quantity of energy equal to the latent heat of fusion while its temperature remains unchanged. However, an abrupt change in some physical properties such as density, heat capacity, electrical and thermal conductivities, diffusivity and elastic properties occur [1-3]. It is a first order transition since the first derivative of Gibbs free energy, G (P,T), with respect to the temperature T and pressure P discontinues. The equilibrium melting point, T_0, is then defined as the temperature and pressure at which the solid and liquid phases coexist in equilibrium, i.e. the two phases have equal values of G, and approximately have equal derivatives, which could be written as [2,3]

$$\frac{\partial G_s(P,T)}{\partial T}dT + \frac{\partial G_s(P,T)}{\partial P}dP = \frac{\partial G_l(P,T)}{\partial T}dT + \frac{\partial G_l(P,T)}{\partial P}dP.$$ (2.1)

Using some basic thermodynamic concepts such as $\frac{\partial G(P,T)}{\partial T} = -S$, $\frac{\partial G(P,T)}{\partial P} = V$, and

$T_0\Delta S_m = L$ with $\Delta S_m = (S_s - S_l)$, one can derive a relation of the melting point as a function of the state variables P and V [2],

$$\frac{T - T_0}{T_0} = \frac{\Delta V \Delta P}{L},$$ (2.2)

where ΔS_m is the entropy change upon melting, and S is the system entropy. The subscripts s and l refer to the solid and liquid states, respectively. The entropy is a measure of the randomness of the system, while L is the latent heat of fusion. Eq. (2.2) is the known Clausius and Clapeyron equation that gives the shift in the melting temperature due to any increase ΔP in the applied pressure, while ΔV is the volume change upon melting. For most substances where ΔV is positive, the melting temperature increases with increasing pressure, however, there is a maximum in the melting temperature as a function of pressure, which corresponds to $\Delta V = 0$ [2]. Materials with negative volume

change upon melting showed melting curves with negative slopes, a decrease in the melting point as the applied pressure is increased, throughout the solid-liquid coexistence curve. A generic P-T phase diagram of a single element system is shown in Fig. 2.1.
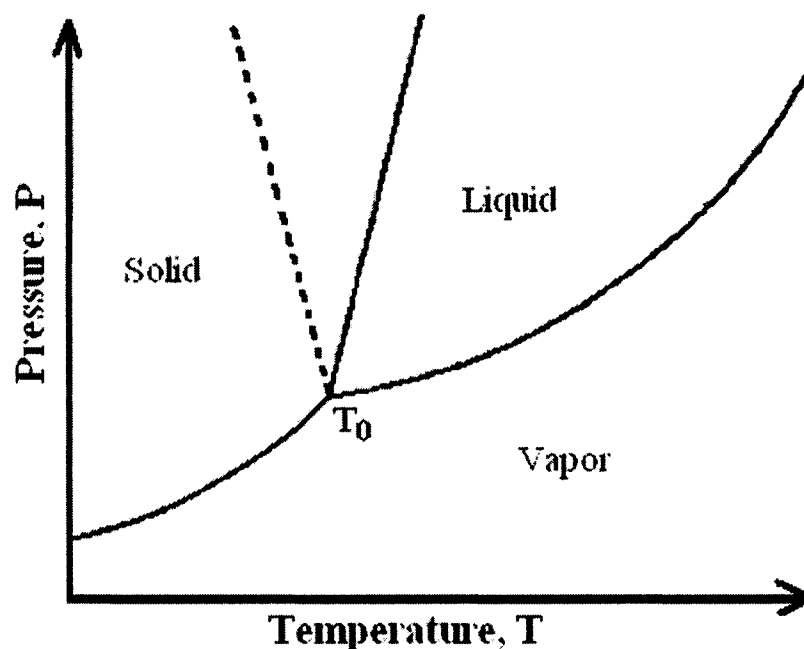
FIG. 2.1. A generic P-T phase diagram of a single element system showing the solid-liquid coexisting line for positive volume change upon melting, solid line, and negative volume change upon melting, dot line. T_0 is the equilibrium melting point or it is the triple point of the system.

In fact, thermodynamic concepts give a macroscopic definition of melting without any microscopic notion of the melting mechanisms or kinetics. Even though there is no generally accepted picture of how solids melt at an atomistic level, there are many melting mechanisms and scenarios that have been proposed and tested during the past decades. Homogeneous melting is one of the mechanisms that assumes that melting occurs homogeneously throughout the crystal as a result of vibrational or mechanical instabilities of the lattice or as a catastrophic generation of lattice defects [1-3]. Surface melting, which is the formation of a surface liquid layer at a temperature below T_0 that

diverges throughout the solid as T_0 is approached, is another scenario that becomes accepted and observed with many different surface sensitive techniques [13-15]. Nanometer-sized crystals showed melting behaviors that could not be explained by any of the existing melting mechanisms or models [16,17]. Efforts are being exerted to develop a melting scenario explaining such behavior [18]. In the sections below, the thermodynamics of these different melting realizations will be briefly reviewed.

II.2.1. Criteria of bulk melting

Since the melting of crystalline solids is seen as a first order phase transition, homogenous melting theories have arisen to provide a microscopic description of melting as a sudden transformation of the solid into liquid. Vibrational lattice instability was of the earliest ideas used to introduce an atomistic understanding of the solid behavior at the onset of melting [19,20]. An empirical relation was used to relate the vibrational motion of the crystalline lattice to the solid temperature, and hence postulate a condition of melting. Generally, the crystalline lattices start to vibrate with increasing amplitude as the material is heated up. Melting is then attributed to the presence of strong lattice vibrations and the material melts when the amplitude of the thermal atomic vibrations reaches a maximum value, a fraction of its nearest neighbor distance. In other words, when this maximum amplitude is reached, no further increase of thermal energy is possible without transitional movement of the atoms from their positions. The mean-square amplitude of thermal vibration, $\langle u^2 \rangle$, is directly proportional to the absolute temperature according to [2,18],

$$\left\langle u^2 \right\rangle = \frac{k_B T}{\beta_{atom}} = \frac{3\hbar^3 T}{mk_B\Theta^2} \text{ , with } k_B\Theta = \hbar\sqrt{\frac{\beta_{atom}}{m}} \tag{2.3}$$

k_B is the Boltzmann's constant, Θ is the Einstein temperature, m is the atomic mass of the material, h is Blanck's constant and β_{atom} is the atomic spring constant, a measure of the elastic stiffness of a material, and it is usually determined by low-temperature heat-capacity measurements [2]. The temperature at which the atoms would begin to melt is estimated to be [2,18],

$$T_{melting} = \frac{(0.083)^2 \quad \Omega^2 \quad m \quad k_B\Theta_D^2}{3 \quad \hbar^2}, \tag{2.4}$$

where Θ_D is Debye temperature and Ω is the molar volume. The significance of the factor 0.083 is that the material is supposed to melt when the vibrational amplitude reaches 8.3%, (~10%) of the nearest neighbor distance, the condition that is known as Lindemann criterion. The ratio between the mean square vibrational amplitude and the interatomic distance is taken to be material independent. However, continuous testing suggested that this ratio depends on the crystal structure and on the nature of the interatomic force [2]. In other words, Lindemann's criterion holds well within each group of crystals that have the same structure and the same type of interacting potential. Beside the fact it has a non-generic nature, Lindemann's theory of melting describes melting as an individual atomic property without mentioning the liquid phase [21]. Also, Lindemann's rule, as a catastrophic theory, implies lattice instability at the melting and hence crystals can not be superheated without changing the maximum attainable amplitude [22]. However, there is growing evidence that crystals can be superheated to temperatures above their equilibrium melting points [8-10].

Mechanically, the liquid differs from a crystal in having zero resistance to the shear stress. Therefore, there must be a point at which the shear modulus of the solid vanishes and hence the material undergoes a solid-liquid phase transition. Based on this fact, Born in 1939 formulated the mechanical criterion of melting that melting should be accompanied by the loss of shear rigidity [23,24]. By increasing the temperature, the distances between the atoms in the solid phase are increased due to thermal expansion; hence the restoring forces between the atoms are reduced. The elastic stiffness tensor C_{ijkl} relates the stress tensor σ_{ij} and the strain tensor ε_{kl} by Hooke's law,

$$\sigma_{ij} = C_{ijkl}\,\varepsilon_{kl} \qquad (i,j,k,l = x,y,z). \tag{2.5}$$

Since each index can vary from 1 to 3 there are 81 elastic constants implied by C_{ijkl}, but because of the symmetry properties of the stress and strain tensors that $\sigma_{ij} = \sigma_{ji}$ and $\varepsilon_{kl} = \varepsilon_{lk}$ resulting in $C_{ijkl} = C_{ijlk} = C_{jikl} = C_{jilk}$, the most general elastic stiffness tensor has only 21 non-zero independent components. For cubic crystals, they are reduced to three components only named as linear, bulk, and shear moduli symbolled as C_{11}, C_{12}, and C_{44}, respectively. These isothermal elastic moduli can be theoretically calculated by [25],

$$C_{ijkl} = \frac{k_B T}{V_0} \delta^{-1}\left(\varepsilon_{ij}\varepsilon_{kl}\right), \tag{2.6}$$

where $\delta\left(\varepsilon_{ij}\varepsilon_{kl}\right)$ is the canonical delta function of the strain elements ε_{ij} and ε_{kl}, and V_0 is the volume of the sample at zero strain. The mechanical instability conditions of vanishing the rigidity modulus for defect and surface free crystals is then found to be [23-25],

$$C_{11} + 2C_{12} > 0,\ C_{11} - C_{12} > 0,\ C_{44} > 0 \tag{2.7}$$

According to Born, C_{12} goes to zero first and the melting temperature can be found from the condition $C_{44} = 0$. These conditions are valid for vanishing external stress only for a perfect infinite crystal, but a real crystal with boundaries and bulk defects undergoes thermodynamic melting before it reaches the mechanical melting point [26,27]. In other words, the rigidity catastrophe would work if the crystal could be superheated to a temperature above the bulk melting temperature [28].

It is proven that thermal creation and annihilation of lattice defects introduce new local modes of vibration, soften the solid, and break down its long-range order structure [29,30]. Therefore, melting might be seen as a progressive generation of crystal lattice defects such as vacancies and intrinsic dislocations at temperatures close to the melting point. The proliferation and the interaction of different types of crystal defects eventually lead to complete isotropy and the resulting state corresponds to that of a proper liquid. The temperature where the defect concentration jumps or shows a sharp increase is identified as the melting temperature. In other words, when defect concentration density, $\rho_{disl.}$, exceeds critical value, the lattice of the solid becomes unstable and a melting transition occurs. In a molecular dynamics simulation, where dislocations near melt were modeled as non-interacting strings on a lattice and move in a closed random walk, the relation between the melting point, T_m, the shear modulus, M_s, the Wigner-Seitz volume, v_{WS}, the coordination number, z, and the critical density of dislocations, $\rho_{disl}(T_m)$, is given by (in units where Boltzman constant k_B equal to unity) [31],

$$T_m = \frac{\eta \lambda M_s \, v_{WS}}{8\pi \ln(z-1)} \ln\left(\frac{\alpha^2}{4 b \rho_{disl}(T_m)}\right), \text{ and} \tag{2.8}$$

$$\rho_{disl}(T_m) = \frac{(0.61 \pm 0.20)}{b^2}.$$

(2.9)

The Wigner-Seitz cell is a primitive cell that displays the full symmetry of the lattice and shows a minimum volume cell with atomic density per cell equal to unity, b is the length of the shortest perfect-dislocation Burgers vector, η, is 1 for a screw dislocation and $\approx 3/2$ for an edge dislocation, $\lambda = \left(b^3/v_{WS}\right)$, and α is a constant that accounts for non-linear effects in the dislocation core with a value of 2.9 [31].

Similar to theories of crystal growth, discussed later, melting can be seen as a process that could nucleate at crystal defects either homogeneously, interior to the crystal at vacancies, interstitials, dislocations, and impurities, or heterogeneously at the grain boundaries, interfaces, and free surfaces [32,33]. The nucleus starts to grow forming a liquid drop or sphere that propagates into the solid at a velocity depending on the degree of superheating. The temperature at which the nucleation rate increases very rapidly is considered to be the critical melting point. For homogenous melting, this temperature is found to be above the thermodynamic melting temperature for various elements, $\sim 1.2\,T_0$ [32]. For low-dimensional material, whose dimensions are less than the critical nucleation size, the calculated temperature is anticipated to be very high. However, in case of heterogeneous melting, surface melting is favorable and hence melting point depression is the most favorable [13,14]. In fact, homogenous nucleation melting is considered an upper limit of the crystal superheating, while heterogeneous melting leads to surface melting and melting point depression.

I.2.2. Surface melting

Surface melting, formation of a liquid-like layer on the top of numerous solid crystals below the bulk melting point have been studied and confirmed in both theory and experiment [13-15]. Surface melting occurs because the combined interfacial energy of the solid-liquid (γ_{sl}) and liquid-vapor interfaces (γ_{lv}) is less than that of the solid-vapor interface (γ_{sv}) [3,13]. This means that, above a certain temperature, it is energetically favorable for the surface to form a thin disordered layer between the ordered solid and the vapor. However, if γ_{sv} is less than the sum of γ_{sl} and γ_{lv}, then it is energetically favorable for the system to stay dry and be transferred directly into the vapor phase [3].

Surface melting involves the formation of a thin disordered surface layer at temperatures below T_0 [3]. The thickness of the disordered layer increases with temperature and diverges as T_0 is approached via the movement of the melt front from the surface into the interior of the solid. The disordered topmost layer doesn't form a true liquid because it is affected by the presence of crystalline order in the solid underneath, i.e. it always contains some crystalline order and has properties intermediate between those of the solid and the liquid. It is usually referred to as a "quasi-liquid" because it has the following properties: i) the surface atoms are dislodged from their lattice sites resulting in a strong reduction of crystalline order; ii) the mobility of the atoms of the surface film is enhanced with respect to the solid, to such an extent, that diffusivity at the surface could be even larger than in bulk liquid, iii) the density and the surface roughness of the melted film are close to the values expected for bulk liquid [3,13]. In fact, surface melting implies that the thickness of the formed liquid or quasi-liquid disordered layer

increases without limit as the temperature approaches T_0. If this thickness remains finite as the temperature increases to T_0, the term incomplete melting is more often used [3].

Surface melting has been indirectly supported by different melting theories. Although the Lindemann's vibrational instability-melting criterion is formulated to describe the homogenous melting, it is the first to point out and inspire the phenomenon of surface melting. Surface atoms have a reduced number of neighbor atoms and hence, are loosely bound. They could also have much higher vibrational amplitude than bulk atoms, and hence, lower melting point than the bulk [2,3]. In other words, Lindemann criterion is fulfilled for a surface at a temperature far below T_0. This argument points to the important role that surfaces may play in the melting process, and provides a simple description of surface melting. Nucleation and growth theory of melting also considered surface melting. Based on this theory, melting is believed to nucleate either homogeneously, interior to the crystal, or heterogeneously, at crystal exterior. Heterogeneous nucleation sites provide lower activation energy and/or minimum barrier for liquid phase formation than any other sites throughout the crystal [32,33]. Furthermore, free surface appears to be the most likely site melt may initiate from in the case of well-prepared single crystals [3].

Using thermodynamics concepts, one can deduce a theoretical expression of the liquid layer thickness as a function of temperature. The following derivation is adapted from Ref. 3. The free energy per unit area of a surface after creation of a quasi-liquid layer of thickness ℓ between the solid and vapor phase near T_m is

$$\gamma = \gamma_{sq} + \gamma_{qv} + L\ N\left(1 - \frac{T}{T_0}\right) \tag{2.10}$$

where γ_{sq}, γ_{qv} are the free energies per unit area of the solid/quasi-liquid and quasi-liquid/vapor interfaces, respectively. L is the latent heat of melting per atom and N is the number of atoms per unit area in the quasi-liquid layer of thickness ℓ such that $N = n\,\ell$ and n is the atomic concentration. The last term in the above equation represents the free energy associated with the undercooled quasi-liquid layer considering that the latent heat involved in the solid/quasi-liquid transition is approximately equal to the latent heat involved in the solid/ liquid transition. The specific free energy for the quasi-liquid/vapor interface, γ_{qv}, will lie between the specific free energy of the liquid/vapor interface γ_{lv} and the specific free energy of the perfect solid/vapor interface γ_{sv} (the surface without the quasi-liquid layer). The specific free energy γ_{sq} will be smaller than the solid/liquid specific interface energy γ_{sl}, so it may be written as

$$\gamma_{qv} = \gamma_{lv} + M\left(\gamma_{sv} - \gamma_{lv}\right) \quad \text{or} \quad \gamma_{sq} = \gamma_{sl}\left(1 - M\right). \tag{2.11}$$

M is the effective crystalline order parameter, normalized such that it is unity for the solid crystal and zero for true liquid. For M, one could take the Fourier component of the density having the periodicity of crystal lattice. The order parameter in the quasi-liquid film thickness:

$$M = e^{-\ell/\ell_0} = e^{-N/N_0} \tag{2.12}$$

where $N_0 = n\,\ell_0$ is a constant of microscopic dimensions, of the order of 10^{15} atoms/ cm^2 and ℓ_0 is of the order of the interlayer spacing. Eqs. (2.11) and (2.12) are appropriate for a system governed by short-range forces. They also satisfy the following boundary conditions,

$$\begin{cases} (i) \quad \ell \to \infty, quasiliquid\ becomes\ true\ liquid \Rightarrow M \to 0, and\ \gamma_{qv} \to \gamma_{lv} \\ (ii) \quad \ell \to 0, quasiliquid\ vanishes \quad \Rightarrow\ M \to 1,\ \gamma_{qv} \to \gamma_{sv}, and\ \gamma_{qv} = 0 \end{cases} \tag{2.13}$$

Substituting Eqs (2.11) and (2.12) into (2.10) yields

$$\gamma = \gamma_{sq} + \gamma_{qv} + L \ N\left(1 - \frac{T}{T_0}\right) + (\gamma_{sv} - \gamma_{sl} - \gamma_{lv})e^{-N/N_0} .$$

(2.14)

The number of atoms in the quasi-liquid layer at equilibrium is obtained by minimizing γ with respect to N, resulting in

$$N_{eq.}(T) = N_0 \quad ln\left(\frac{T_0 \, \Delta\gamma}{(T_0 - T)L \, N_0}\right) ,$$

(2.15)

where $\Delta\gamma = \gamma_{sv} - \gamma_{sl} - \gamma_{lv}$ is the specific interfacial free energy at temperature T. Then the number of equilibrium melted atoms in the quasi-liquid layer increases logarithmically as T approaches T_0. Considering long-range forces $N_{eq.}(T)$ was found to grow asymptotically as $|T_0 - T|^{1/(p+1)}$, the obtained form is

$$N_{eq.}(T) = \left(\frac{T_0 \, \Delta\gamma N_0 p}{(T_0 - T)L}\right)^{1/(p+1)} - N_0 \quad ,$$

(2.16)

where p is a constant with a value of 2 for non-retarded van der Waals interactions. It is easily deduced from Eq. (2.15) or (2.16) that the necessary condition for surface melting is the number of atoms in the quasi-liquid layer at equilibrium is not zero and has a positive value that is

$$\Delta\gamma = \gamma_{sv} - \gamma_{sl} - \gamma_{lv} > 0 .$$

(2.17)

This condition is similar to solid wetted by its won melt where the solid-liquid contact or wetting angel, θ, is given by $cos \ \theta = \gamma_{sv} - \gamma_{sl}/\gamma_{lv}$. If $\theta < 90$, which implies $\gamma_{sv} > \gamma_{sl}$, then the liquid wets the surface and if $\theta > 90$, this implies that $\gamma_{sv} < \gamma_{sl}$ and the melt doesn't wet the surface. One can treat surface melting as a surface completely wetted with its liquid, while the un-wetted surface implies superheating [34].

Normally, γ_{lv} is calculated based on model surfaces having average density, while

γ_{sv} has surface density or orientation dependence. For most metals the anisotropy is small,

but it can lead to a large energy variation and hence dramatic change in melting behavior.

The surface melting criteria has the same orientation dependence as γ_{sv}. The value of γ_{sv}

not only determines the melting behavior of the surface but also the equilibrium shape of

the grown crystals [35,36]. Based on the surface orientation, the crystal may show surface

melting, incomplete melting, or crystal superheating [37,38]. Close packed or high dense

crystal surfaces such as fcc(111) remain completely solid and can even superheat to a

temperature above T_m [39-41]. Small crystals bounded by non-melting or close packed

facets also showed superheating for an extended amount of time [42,43].

II.2.3. Melting of small crystals

It is now believed that any property of any physical system may change even

dramatically as a function of the physical dimension of that system [44]. For small

crystals, composed of a countable number of atoms each, the high proportion of atoms at

the surface make an important contribution to the particle's total energy. Accordingly,

each time one atom is added to the cluster, the clusters attain new atomic arrangements

that are energetically favorable at low dimension while it might be forbidden in the bulk

[45]. After a certain size, the concentric layers of atoms are added in such a way that the

overall symmetry of the clusters is left unchanged [45]. With the structure geometry

change, all other physical properties are expected to change including the characteristic

melting point of the material.

Melting of small particles attracted interest long before the early days of modern cluster science. The first attempts made for theoretical understanding the melting of small particles were made within a macroscopic framework using thermodynamic concepts such as surface energy. There are many phenomenological models describing the melting point size dependence of nanometer-sized crystals [46-54]. All of them predict a linear or semi-linear relation between the melting point of the crystals and the reciprocal of its radius. These models can be summarized as; the homogenous melting (HM) model [47,48], liquid skin (LS) model [46-49], nucleation and growth (NG) model [32,50], the liquid- drop (LD) model [51], surface-phonon instability (SPI) model [52], and the lattice vibration-based (LV) model [53,54]. All of these models assumed spherical particles and drop the shape effect by adapting an orientation independent value of the solid/vapor interfacial energy. In HM model, the melting point is the point at which the melt and the solid coexist homogenously in equilibrium. According to this model, the size dependence of the melting point is described by [46,47],

$$\Delta T = T_0 - T_m = \frac{2\,T_0}{\rho_s\,L\;r}\left[\gamma_s - \gamma_l\left(\frac{\rho_s}{\rho_l}\right)^{2/3}\right],$$
(2.18)

where T_0 is the bulk melting point, T_m is the melting point of a cluster of radius r, L is the latent heat of fusion, and γ_s, γ_l, ρ_s, and ρ_l are the surface energy per unit area and the density of the solid and liquid phases. An extra interfacial energy should be added to account for the substrate-nano-crystal interaction. Based on this type of interaction, the cluster may have a different melting point.

The LS model considers a core of solid particles covered with its liquid melt. The melting point of this nano-crystal is then defined as the point where the core is in

equilibrium with the liquid skin at its critical thickness [46-49]. The thickness of the liquid layer is used as an adjustable parameter to match the model prediction with the experimental results. The relation between the melting point and the crystal size is found to be [46-49],

$$\Delta T = T_0 - T_m = \frac{2\,T_0}{L}\left[\frac{\gamma_s}{\rho_s(r-\delta)} + \left(\frac{\gamma_l}{r} + \frac{\Delta P}{2}\right)\left(\frac{1}{\rho_s} + \frac{1}{\rho_l}\right)\right], \quad (2.19)$$

where δ is the adjustable liquid thickness and ΔP is the difference between the vapor pressure at the surface of the liquid layer of radius r and that at a flat surface, which in many cases could be neglected. In NG model, melting is thought to nucleate either at homogeneous sites interior to the crystal or at heterogeneous sites such as the crystal surface. For heterogeneous nucleation, melting is started by forming a nucleation of a liquid layer at the surface and moves into the solid as a slow process with definite activation energy. The temperature range where the solid and liquid can coexist in equilibrium, and hence a nucleus liquid can grow, is defined as [49,50],

$$T_m = T_0 - \frac{2T_0}{Lr}\alpha_{NG} \;,\; \text{where}\; \gamma_{sl} < \alpha_{NG} < \frac{3}{2}\left(\gamma_{sv} - \gamma_{lv}\frac{\rho_s}{\rho_l}\right) \quad (2.20)$$

Outside this range, only single phase, either solid or liquid, can exist. For a confined crystal, melting can nucleate homogeneously from the crystals interior and superheating is possible [8,32]. In this case, NG model can be used to derive the upper limit of crystal superheating when heterogeneous melting is avoided. The relationship between the melting point and the critical size of a spherical molten nucleus r_c is then derived using the analogy between crystal growth from the melt and melt growth in a solid. This relation is found to be [32],

$$T_m - T_0 = \frac{T_0}{L}\left(\frac{2\gamma_{sl}}{r_c} + \Delta E\right), \qquad\qquad (2.21)$$

where ΔE is the change in strain energy per unit volume resulting from the volume change upon melting. Because a higher homogeneous nucleation per unit volume is required for small crystals, this model predicts that the degree of superheating increases with decreased crystal size. This type of melting does not apply to the unconfined nanocrystals presently studied.

In LD model, empirical relations between cohesive energy, surface tension, and melting temperature is used in an analogy to the liquid-drop model used in describing the nucleus structure. An expression for the size-dependent melting for low-dimensional systems is derived such that [51],

$$T_m = T_0\left(1 - \frac{\beta}{r}\right) \qquad\qquad (2.22)$$

where β is a surface energy dependent constant. SPI model assumes that the mean phonon frequency of the particles varies linearly with the number of defects and surface sites produced in the nanoparticle [52]. A relation between the particle melting point and its radius is found to have a form similar to that of Eq. (2-22). However, in this case, the constant β is varied depending on the bulk melting temperature and the energy of formation of intrinsic defects. LV model is another approach that does not include any adjustable parameter [53-55]. It is based on Lindemann's criterion and Mott's expression of the vibrational entropy, which gives a melting point size-dependent formula as [53-55],

$$\frac{T_m}{T_0} = \exp\left[\frac{-(\alpha-1)}{(\frac{r}{\xi})-1}\right] \text{ with } \alpha = \frac{2}{3}\frac{S_m(\infty)}{K_B} + 1 \text{ and } \xi = (3-d)h \qquad (2.23)$$

where $S_m(\infty)$ is the vibration entropy of melting of the bulk crystal, ξ is a critical radius at which all atoms of the nanocrystal are located on the surface, K_B is Boltzmann's constant, h is the atomic diameter, and d is a constant that depends on the crystal dimension ($d = 0$ for nano-crystals, 1 for nanowires, and 2 for thin films).

II.3. Melt solidification

It has been acknowledged that solidification processing plays an important role, not only for improving the performance of a given product through optimizing its macro- and micro-structure, but also in developing novel materials as well [56]. Macroscopically, solidification is the transformation of the material from liquid melt into solid as the heat content of the melt is reduced. It is a process that is driven by the lowering of the free energy of the system across the liquid-solid phase transition. Close to the equilibrium transition point, the liquid phase remains metastable and a structural fluctuation is required to cause the appearance of the first nucleus of the solid phase [57,58]. However, it is the solid-liquid interfacial energy that controls the nucleation criterion and determines the nucleation and transition rates. Under a given condition, if the probability of creating a nucleus is homogeneous throughout the system, the nucleation is defined as homogeneous nucleation; otherwise it is heterogeneous [59]. The presence of foreign sites such as container walls, substrate surface, and impurities facilitate nucleation and increase its formation probability. Because the energy of heterogeneous nucleation formation is lower than that of the homogenous one, and because it is experimentally

impossible to eliminate all the heterogeneous sites, nucleation has the heterogeneous nature rather than the homogeneous nature in most cases.

In any case, formation of stable nuclei able to grow is essential for solidification. This process depends on the free energy need to be invested to generate a critical nucleus. Critical nucleus is a nucleus of size beyond which spontaneous nucleation growth is energetically favorable. There are different theoretical approaches developed to understand the nucleation kinetics and to determine the size and energy barrier of the stable nuclei [60-63]. Classical nucleation theory (CNT) is a theory that has been used to predict the properties of the critical nucleus from macroscopic measuring quantities using phenomenological thermodynamics. Other approaches, mainly simulation and computation methods, use microscopic models to represent the system's structure and derive its macroscopic properties from first principles. Of these methods, the density functional theory (DFT) that assigns an interacting potential between all the particles of the system and calculates the free energy density of the system, which will depend on the density of particles at that location [61,62]. By minimizing the obtained free energy density functional, thermodynamic relationships that determine all the thermodynamic properties of the system can be derived. These relationships can be used to evaluate the properties of stable and metastable phases at a given temperature and pressure, the structure of the phase diagram, or the surface tension between coexisting phases. However, because of the usage of potential functions that might not represent the real situation well, and that modeling might also contain adjustable parameters, these techniques are sometimes considered to be of empirical or semi-empirical nature [63].

Although CNT is usually criticized for ignoring the effect of curvature on surface free energy and for predicting a finite barrier as the spinodal is approached, it is still the basis for understanding the dynamics of every first-order transition. Moreover, it is considered the essential foundation even for the more sophisticated simulations, which might use many of its concepts either for comparison or for some parameters adjustment. In this section, the homogeneous and heterogeneous solidification will be discussed according to CNT.

II.3.1. Homogeneous solidification

Containerless strictly pure melt in which the melt is confined by its own surface tension and contains no impurity can be homogeneously solidified via homogeneous nucleation formation [59-61]. The thermodynamic precondition for nucleation and growth of the solid phase is that the system must be in supersaturation, which occurs when $\Delta\mu = \mu_l - \mu_s > 0$, μ is the chemical potential of the system, i.e. the system in a supercooled metastable phase [59]. When $\Delta\mu < 0$, the system is said to be undersaturated and hence crystals will re-melt or disintegrate, while the two phases are in equilibrium if $\Delta\mu = 0$. At temperatures not far below the melting temperature, the chemical potential difference between solid and liquid is given by [56,60],

$$\Delta\mu = \Delta T\, S_m,\tag{2.24}$$

where $\Delta S_m = (S_s - S_l)$ is the entropy of melting per unit volume, and ΔT is the supercooling amount. In fact, the difference in chemical potential between the two phases is the thermodynamic driving force for solidification initiations or nucleation. The widely accepted kinetic model of nucleation (within the cluster approach) is based on the

successive "chain reaction" between atoms to form multi-atomic clusters, which are consecutively joined by further atomic monomers/atoms to form stable nuclei [59]. However, the cluster formation and hence the nucleation process is an energy activated process in which an energy barrier needs to be prevailed over. The homogeneous Gibbs free energy change, ΔG_r^{hom}, upon forming a nucleus sphere with radius r inside the liquid melt, assuming constant and isotropic surface tension, is given by [56,61,62],

$$\Delta G_r^{hom} = -\frac{4}{3}\pi r^3 \Delta G_{sl} + 4\pi r^2 \gamma_{sl},$$ (2.25)

where $\Delta G_{sl} = G_l - G_s = \left(L\Delta T/T_0\right)$ is the bulk free energy difference per unit volume between the supercooled liquid and the formed solid, L is the latent heat of fusion, and γ_{sl} is the surface tension of the solid-liquid interface. The gain in free energy associated with the formation of a volume of stable nucleus is competing with the cost of creating a solid-liquid interface. The interfacial term increases as r^2 and the volume term increases as r^3. Therefore, it should be a certain critical radius, r_c, at which the free energy is maximum. Fig 2.2 shows a schematic of the thermodynamic nucleation kinetics and the formed energy barrier at the critical nucleus.

Using the equilibrium condition, $\Delta G_r^{hom} = 0$, one can find the value of r_c and the energy barrier for nucleation, $\Delta G_{r_c}^{hom}$, to be

$$r_c = \frac{2\gamma_{sl} T_0}{L(\Delta T)}, \text{ and } \Delta G_{r_c}^{hom} = \frac{16\gamma_{sl}^3 T_0^2}{3L^2 (\Delta T)^2}.$$ (2.26)

If $r > r_c$, the system decreases its free energy by excess solidification, while if $r < r_c$, the system lowers its free energy by excess melting. A nucleus will be stable if it has a radius larger than or equal to r_c.
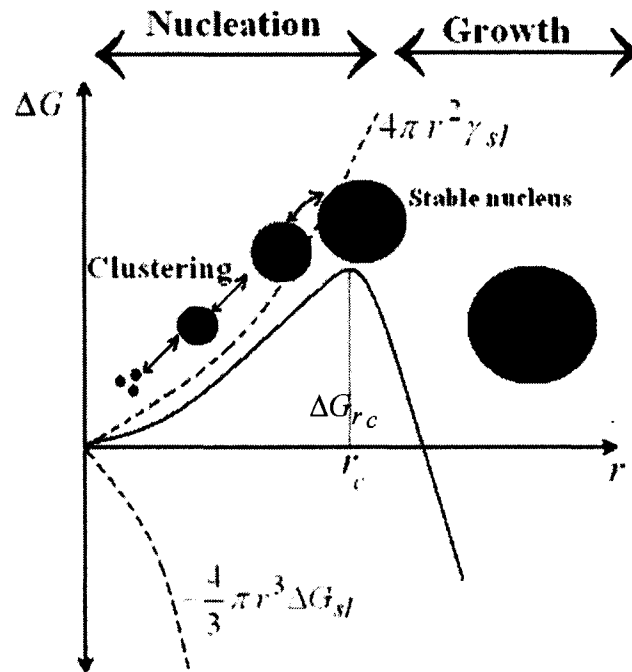
FIG. 2.2. A schematic diagram represents the thermodynamic nucleation kinetics. The free energy change of a nucleus sphere consists of an energy released volume term, varies as r^2, and an energy obstacle interfacial term, varies as r^3. At a certain critical radius, r_c, a stable nucleation is formed and starts to grow. For a stable nucleus, an energy barrier height ΔG_{r_c} needs to be overcome, [after Ref 56 and 59].

After formation of a stable nucleus, the second stage in the solidification mechanism is the growth of the formed nucleus. The growth rate is determined by the transport of monomers, clusters, or atoms through the liquid to the solid phase boundary and by the dissipation rate of the released latent heat or cooling rate [56]. Therefore, in addition to the energy barrier for nucleus formation, an energy barrier account for the transport processes in the liquid is introduced (the diffusion activation energy). It is

generally assumed that the rate of homogeneous nucleation, j_{hom}, can be modeled by an

Arrhenius-type dependence, where the sum of the two energy barriers $\Delta G_{r_c}^{hom}$ and ΔE_D

is used as an activation energy for the process [56,59-61],

$$j_{hom} = C_0 \, exp\left(-\frac{\Delta G_{r_c}^{hom} + \Delta E_D}{k_B T}\right), \quad or \tag{2.27}$$

$$j_{hom} = f_0 \, C_0 \, exp\left(-\frac{16\gamma_{sl}^3 \, T_0^2}{3L^2 k_B T} \frac{1}{(\Delta T)^2}\right), \tag{2.28}$$

where C_0 is the number of atoms per unit volume, ΔE_D is the diffusion activation

energy, and k_B is the Boltzmann's constant. The parameter f_0, which depends on the

vibration frequency of the atoms, activation energy of diffusion in the liquid, and the

surface area of the critical nuclei, is taken to be constant $\sim 10^{11}$ [56]. The energy barrier

depends on ΔT and varies from an infinite value near the bimodal (the point at which the

original phase becomes thermodynamically unstable) to zero near the spinodal where the

system becomes unstable to arbitrarily small fluctuations of the new phase [59]. Because

of the exponential dependence on a rapidly varying free-energy barrier height,

homogeneous rates are extraordinarily sensitive to thermodynamic conditions of

temperature and pressure, as well as to small variations in intermolecular potentials.

Moreover, the situation is more complicated in mixtures where species of different

diffusion rates are present, and thus the growth rate is controlled by the diffusion rate of

all species within the mixture [64].

II.3.2. Heterogeneous solidification

Heterogeneous nucleation is the most common and naturally found mechanism in initiating most of the first-order phase transitions. Foreign surfaces in contact with a melt can induce nucleation, and hence solidification occurs at degrees of supersaturation lower than those required for spontaneous or homogeneous nucleation [59,62]. In other words, the presence of these heterogeneous sites acts as catalytic surfaces that decrease the activation energy and increase the nucleation process and solidification rate. Using a phenomenological procedure similar to that adapted for homogeneous nucleation, the free energy change associated with the formation of a solid nucleus of radius r on top of an impurity surface is found to be [56,60,62],

$$\Delta G_r^{het} = -\frac{4}{3}\pi r^3 \Delta G_{sl} + 4\pi r^2 \gamma_{sl} + A_{sf}\,\gamma_{sf} + A_{lf}\,\gamma_{lf}, \qquad\qquad (2.29)$$

where $A_{sf}, A_{lf}, \gamma_{sf}$, and γ_{lf} are the heterogeneous interfacial areas and interfacial free energies per unit length of solid-foreign (sf) and liquid-foreign (lf) interfaces. This formulation is based on the assumption that the system has a nonisotropic surface energy and the nucleus has a spherical cap-like shape. Using the analogy between heterogeneous nucleation and a wetting of a foreign surface by three a phase (solid, liquid and gas) system, one can find heterogeneous free energy change, ΔG_r^{het}, upon forming a nucleus of radius r to be,

$$\Delta G_r^{het} = \left(-\frac{4}{3}\pi r^3 \Delta G_{sl} + 4\pi r^2 \gamma_{sl}\right)S(\theta), \qquad\qquad (2.30)$$

where $S(\theta) = \dfrac{(2+\cos\theta)(1-\cos\theta)^2}{4}$. Using the equilibrium condition to find the energy

barrier for heterogeneous nucleation and compare it with the obtained form of

homogeneous nucleation, one can easily find that,

$$\Delta G_{r_c}^{het} = \Delta G_{r_c}^{hom} S(\theta).$$

(2.31)

Since $S(\theta)$ has a numerical value ≤ 1, the energy barrier for heterogeneous nucleation

will always be less than that for homogeneous nucleation. Moreover, $S(\theta)$ depends only

on θ which in turns depends on the nature of the melt-solid-foreign surface interaction.

This means that the energy barrier for heterogeneous nucleation is sensitive to the type of

the heterogeneous surfaces and the shape of the nucleus [59,62]. Since heterogeneous

sites are stochastic in nature, it is hard to account for them, except for known surface or

container wall. The heterogeneous growth rate, similar to homogenous process, is

normally given by,

$$j_{het} = C_0 \exp\left\{-\left(\frac{\Delta G_{r_c}^{hom} + \Delta E_D}{k_B T}\right) S(\theta)\right\} = j_{hom} \exp(-S(\theta)), \text{ or}$$

(2.32)

$$j_{het} = f_0 C_0 \exp\left\{\left(-\frac{16\gamma_{sl}^3 T_0^2}{3L^2 k_B T}\frac{1}{(\Delta T)^2}\right)(-S(\theta))\right\}.$$

(2.33)

Because of the exponential dependence on $S(\theta)$, the value of heterogeneous growth rate

is much larger than that of the homogenous rate. Because of the ubiquitous of the

heterogeneous sites, real systems always solidified heterogeneously.

II.4. Asymmetry between melting and solidification

Although nucleation during solidification usually requires some undercooling, melting normally occurs at the equilibrium melting temperature without superheating. Supercooling is the presence of the material in a liquid phase at a temperature lower than its melting point, while superheated crystals reserve their long-range order at temperatures above T_0 and have unusual high atomic mean-vibrational amplitude. On the opposite of supercooling, superheating of crystalline solid is rare and the superheating amount, $(\Delta T)^+$, is always less than that of the observed supercooling amount, $(\Delta T)^-$. This phenomenon is known as the phenomenological kinetic asymmetry between melting and solidification [65].

The phenomenological kinetic asymmetry between melting and solidification is supposed to originate from the presence or the absence of an energy barrier for new phase formation, which is different for melting and solidification [65]. Melting is initiated at surfaces or interfaces where nucleation of the liquid phase is unnecessary, i.e. there is no energy barrier for melting, while freezing of a melt has to overcome an energy barrier [3,13]. For a given element or system the energy barrier is mainly due to the volume expansion during melting, whereas it could be negligible during freezing [56]. The activation energy of atomic diffusion during melting is much smaller than that during freezing, due to the higher transition temperature of melting. Thus, it results an asymmetry not only in the transition point but also in the transition rates [9,56,65]. Moreover, the increase in free energy of the system upon solidification may be able to maintain the liquid phase in a metastable state almost indefinitely at temperature below

T_m [56]. In fact, these factors make it impossible to have a symmetric melting and freezing behaviors.

The section below introduces a survey on both supercooling and superheating phenomena observed during solid-liquid phase transition. The current understanding and the theoretical and experimental approaches are also reviewed.

II.4.1. Superheating of solid crystals

Superheating of solid crystals is not common because surface melting is energetically favorable for many solid surfaces. Surface melting eliminates the barrier for nucleation of the liquid phase and paves the way for further melting [3,13]. This implies that crystal superheating, under ordinary circumstances, is impossible. In other words, crystal superheating is possible only if surface melting is suppressed. Thus, several experimental ways have been developed to suppress surface melting and superheat the solid above the equilibrium melting point [66-70]. One way is to embed the metal crystal into another metal with a higher melting temperature, as observed for small Pb precipitates in Al that could superheat up to 62 K [68]. In these types of experiments, the interface between the crystallites and the host matrix play an essential role in their melting behavior. Those with coherent or semi-coherent interfaces showed superheating, while the randomly orientated crystallites showed melting point depression [69]. Coating the crystal by a higher melting material is another technique used to superheat solid crystals. Ag spheres coated by a few monolayers of Au were found to superheat by 25 K for a period of 1 min [70].

Solids with a highly viscous melt such as quartz can be superheated up to several hundred degrees above the bulk melting point [71]. The solid liquid transition is then

limited by the liquid propagation velocity rather than by the heat flow. Superheating of metal crystals, in that sense, is more difficult because metals have low viscous liquid and some of its surfaces show surface melting [1,3]. In this case, the melting process is heat flow limited. On the other hand, if the heating is so intense that the temperature rise at the interface is faster than the liquid propagation velocity, the solid may be driven into a highly superheated metastable state. Using laser heating, superheating by 120 K for Pb(111), 90 K for Bi(0001), and even 15 K for the incompletely melted Pb(100) have been found [39,72,73]. Superheating of these surfaces was achieved from bypassing the melting temperature via large heating and cooling rates of about 10^{11} K/s.

It was also found that some close-packed metal surfaces remain solid and may superheat above the melting point [42,43,74]. Growing some crystallites that bounded by non-melting facets is another attempt to superheat small crystals [42,43]. Non-equilibrium octahedral lead crystallites deposited on graphite made up of the {111} facets and small round parts exhibit superheating by several degrees for several hours [74].

Several attempts have been made to estimate the upper limit of superheating. Starting from the normal definition of the bulk melting point, the temperature at which the free energy of the solid equals that of the liquid, one can extend the idea to estimate the superheating limit. Fecht and Johnson proposed a thermodynamic stability limit for the superheated crystal in terms of an entropy catastrophe [75]. Their critical isentropic temperature, T_m^s, is the temperature at which the entropy of the superheated crystal equals that of the liquid phase. The numerical value of this isentropic temperature, T_m^s, for Al is found to be 1.38 T_m above the bulk melting temperature. Furthermore, the value T_m^s is

calculated for most of the periodic table elements, and it is found that T_m^s could be as high as twice the normal melting point [32].

Isochoric catastrophic temperature, T_m^v, the temperature at which the volume of the superheated crystal equal to that of the liquid melt, rigidity catastrophic temperature, T_m^r, the temperature at which the shear modulus vanishes, and the Isenthalipic superheating limit temperature were claimed to be the maximum superheating temperatures the crystalline solid may withstand [28]. Lu and Li have proposed another homogenous nucleation catastrophe for crystal superheating [32]. They have found that if heterogeneous nucleation centers are avoided and the crystal is melted due to homogenous melting centers only then a massive homogenous nucleation catastrophe occurs at a critical superheating temperature, T_m^K, estimated to be $\sim$ 1.2 T_m for Al. The upper limit temperature for crystal superheating due to the rigidity catastrophe, T_m^r, is found to be below the instability limits defined by the volume isochoric catastrophe, T_m^v, and the entropy catastrophe T_m^s. However, the superheating observed experimentally in metallic crystals, which is about 1.1T_0, is evidently far below these proposed instability limits that range from 1.3T_0 to 2.0T_0 [32]. The homogenous nucleation catastrophe limit T_m^K is well above the experimental observed superheating of metal crystals and it is the lowest stability limit of the superheating crystals at all.

In spite of the abovementioned ideas for estimating the upper limit of the superheating temperature, none of them agree with the experimentally observed one. However, the massive homogenous catastrophe is considered to be the closest one to the real. Moreover, none of these theories discussed the time period that a solid may remain

between the melting temperature T_0 and a thermodynamic critical temperature T_m^c. However, the possibility of long-term existence of a substance can be governed by the following rule: for any abnormal physical state such as the crystal superheating, either the duration of existence of such a state is very small or the penetration into this region is limited [7].

II.4.2. Supercooling of liquid melt

Because of the presence of energy barrier for solid nucleation enlarged by the volume change upon solidification and the release of latent heat, melted materials normally stay in the liquid phase below T_0 without solidification. Since the height of this energy barrier decreases as the amount of supercooling increases, see Eq. (2.26) and (2.31), the melt stays in this metastable supercooling state until the due point, the point at which spontaneous solidification occurs, is reached. A structure fluctuation, formation and disintegration of small size metastable nucleus or the presence of dynamical size distribution, is assumed to be the characteristic feature during supercooling [57,58]. The metastable nature of the supercooled melt also provides the possibility of metastable phases or structure formation, while a stable phase is formed only after the due point.

The due point or supercooling point and hence $(\Delta T)^-$ is determined mainly by the nucleation type. In other words, supercooling is limited by the presence of impurities within or at the surface of the liquid that act as heterogeneous sites for nucleation [57]. For systems where heterogeneous nucleation is dominant, usually small undercooling amounts are observed [59]. Nevertheless, if heterogeneous nucleation is suppressed,

eliminated, or avoided, for instance by containerless processing of pure liquids such that of water suspension in oil, liquid phase can be significantly supercooled [76].

In addition to the heterogeneous impurity sites, supercooling showed a thermal history dependent [57,68,69]. Thermal history is a wide expression that includes all experimental parameters involved in the melting and solidification process such as heating and cooling rates, melt overheating above T_0, the liquid overheating period, and number of heating and cooling cycles [57]. In fact, the effect of the heat treatment or thermal history on the supercooling results from its role in reducing or removing the active nucleation sites of the container wall-melt interface, and its influence on the melt structure [57,59]. Immediately above or exactly at T_0 the system is not in a true liquid phase, however, it is a combination of melted liquid and insoluble metallic clusters. In other words, even the system is in the molten state, the short-range structure remains the same as that of the solid. The complete destroy of the short-range structures or complete dissolution/melting of the remaining clusters is temperature and time dependent [77,78]. Also, these clusters can act as solid seeds or these short-range liquid structures can evolve to the solid phase with zero free energy barriers if the system is cooled immediately after reaching T_0. If the system is completely melted and the short-range structure is completely destroyed, either by overheating the melt above T_0 or by increasing the liquid overheating period, a larger supercooling would be attained. A linear relation between the amount of supercooling and the amount of liquid overheating at some cooling conditions are sometimes observed [78]. Different supercooling rates can also lead to different amounts of supercoolings with a significantly large supercooling achieved at a higher

cooling rate where nucleation is considered as a rate limited process [77,78]. The nucleation is retarded due to the low heat dissipation and/or diffusion rates.

The amount of supercooling, $(\Delta T)^-$, is found to show size and be mass dependent [80,81]. Generally speaking, the lower the size the lower the supercooling point and the higher the amount of supercooling. Therefore, one might divide the melt into large number of isolated droplets or confined the liquid in highly porous media with porous size in the nanometer range to avoid nucleation and to attain large amounts of supercooling. This is simply because of the increase of the surface to volume ratio as the droplet size is increased. Moreover, one might think that droplets with sizes lower than critical nucleation size may remain liquefied with significant amounts of supercooling. In fact, the concept of critical size relevant to the solidification of bulk liquid doesn't apply. However, a shift in the supercooling point is thermodynamically favorable and below this point nuclei of any length will tend to grow [81,82]. Using a thermodynamic treatment similar to heterogeneous nucleation of Eq. (2.29) using a cylindrical-like container of height h and radius R, the critical supercooling temperature, T_s^*, and the amount of supercooling are estimated to be [81,82],

$$(\Delta T)^- = T_0 - T_s^* = \frac{2\Delta\gamma V_M T_0}{L R},$$ (2.34)

where $\Delta\gamma$ is the difference between the solid/wall and liquid/wall interfacial energies, L is the latent heat of fusion, and V_M is the molar volume. This equation emphasizes the linear relation between $(\Delta T)^-$ and the reciprocal of the porous radius, $(1/R)$.

Based on CNT for heterogeneous nucleation, the cluster size is related to the amount of supercooling in an Arrhenius-like relationship, Eq. (2.34). Assuming that the

droplet diameter d, which is given by $d = j_{het}A_d$, where A_d is the surface area of a droplet, and using Eq. (2.33), the dependence of the amount of supercooling on the droplet size can be given by,

$$\ln d = C + C' \left\{ \frac{1}{T(\varDelta T)^2} \right\},$$

(2.35)

where C and C' are constants that depend on the catalytic effect of the heterogeneous nucleus and the melt properties. Thus, CNT suggests a linear relation between $(\ln d)$, and $(1/\varDelta T^2)$. However, experimental testing of such relation of pure lead, tin, and bismuth showed that a linear relation is held between the logarithmic diameter of the liquid drop $(\ln d)$ and $(\varDelta T/T_0)$ not $(1/\varDelta T^2)$. Droplet sizes in the range of 10 μm to 2030 μm were tested, and an empirically relation is formulated to fit the obtained measuring date such that [83],

$$\ln d = A - B \frac{(\Delta T)^-}{T_0},$$

(2.36)

where A and B are constant coefficients. The droplet sizes are measured in control atmospheric environment using an optical microscope. In another experimental approach, the droplet geometrical size, $d = (m/\rho)^3$, m is the mass, and ρ is the substance density, is calculated based on accurately weighted samples and assuming cubic geometry [79]. This supercooling-size dependence is found to satisfy a relation similar to Eq. (2.36). For island film condensate, $(\varDelta T)^-$ was found to depend essentially on the substrate type and on the droplet size. The dependence of the contact angle, θ, and hence the $(\varDelta T)^- n$ on the droplet size, in fact, arises from the dependence of the droplet-substrate interfacial

energy $\gamma_{du}(R)$, and the liquid phase surface energy of the droplet $\gamma_l(R)$, on the droplet

radius R. This dependence can be approximated by [80],

$$cos\theta = cos\theta^{\infty} - \frac{\alpha}{R} + \frac{\beta^{'}}{2R} \frac{\gamma_{du}^{\infty}}{\gamma_l^{\infty}} \frac{1}{sin\theta},$$ (2.37)

where α and $\beta^{'}$ are positive parameters of the order of the inter-atomic distances

determining the size dependence of specific energies of the corresponding interface

boundaries, and the subscript ∞ denoting the bulk values.

II.5. References of chapter II

[1]   J. G. Dash, "History of the search for continuous melting," Rev. Mod. Phys. **71**, 1737-1743 (1999).

[2]   J. H. Bilgram, "Dynamics at the solid-liquid transition: experiments at the freezing point," Phys. Rep. (Review Section of Physics Letters) **153**, 1-89 (1987).

[3]   J. F. van der Veen, B. Pluis, and A. W. D. van der Gon, *Chemistry and Physics of Solid Surfaces VII*, (Springer-Veilag, 1988) chap. 16.

[4]   S. R. Phillpot, S. Yip, and D. Wolf, "How do crystal melt?," Comp. Phys. **3**, 20-31 (1989).

[5]   K. Lu and Z. H. Jin, "Melting and superheating of low dimensional materials," Current Open. Sol. State Mater. Sci. **5**, 39-44 (2001).

[6]   R. W. Cahn, "Melting from within," Nature **413**, 582-583 (2001).

[7]   A. D. Suprun and M. A. Razumova, "Long-term existence of a solid surface under temperature above melting point. Is it Possible?," Appl. Phys. A **67**, 237-239 (1998).

[8]   Z. H. Jin and K. Lu, "To what extent a crystal can be superheated?," NanoStruct. Mat. **12**, 369-372 (1999).

[9]   S. Luo and D. C. Swift, "On asymmetry between superheating and supercooling in solid-liquid transitions: Landau models," J. Chem. Phys. **121**, 7387-7389 (2004).

[10]   E. Poniatowski, R. Serna, C. N. Afonso, M. Jouanne, J. F. Morhange, P. Bosch, and V. H. Lara, "Hysteresis in the melting kinetics of Bi nanoparticles," Thin Solid Films **453/454**, 467-470 (2004).

[11]   F. Banhart, E. Hernández, and M. Terrones, "Extreme superheating and supercooling of encapsulated metals in fullerenlike shells," Phys. Rev. Lett. **90**, 185502:1-4 (2003).

[12]   S. Luo, T. J. Ahrens, T. Çaḡin, A. Strachan, W. A. Goddard III, and D. C. Swift, "Maximum superheating and undercooling: systematics, molecular dynamics simulations, and dynamic experiments," Phys. Rev. B **86**, 134206:1-10 (2003).

[13]   J. F. van der Veen, "Melting and freezing at surfaces," Surf. Sci. **433/435**, 1-11 (1999).

[14]   J. W. M. Frenken and   J. F. van der Veen, "Observation of surface melting," Phys. Rev. Lett. **54**, 134-137 (1985).

[15]   M. Polcik, L. Wilde, and J. Haase, "Surface melting of Al(110) studied by surface extended x-ray absorption fine structure," Surf. Sci. **405**, 112-120 (1998).

[16]   Y. Efremov, F. Schiettekatte, M. Zhang, E. A. Olson, A. T. Kwan, R. S. Berry, and L. H. Allen, "Discrete periodic melting point observations for nanostructure ensembles," Phys. Rev. Lett. **85**, 3560-3563 (2000).

[17]   M. Schmidt, R. Kusche, B. von Issendorff, and H. Haberland, "Irregular variations in the melting point of size-selected atomic clusters," Nature **393**, 238-240 (1998).

[18]   F. Calvo and F. Spiegelmann, "Geometric size effects in the melting of sodium clusters," Phys Rev. Lett. **82**, 2270-2273 (1999).

[19]   F. A. Lindemann, "The calculation of molecular vibrational frequencies," Z. Phys. **11**, 609-612 (1910).

[20]   Y. Ida, "Theory of melting based on lattice instability," Phys. Rev. B **187**, 951-958 (1969).

[21]   H. Kleinert and Y. Jiang, "Defect melting models for cubic lattices and universal laws for melting temperatures," Phys. Lett. A **313**, 152-157 (2003).

[22]   Z. H. Jin, P. Gumbsch, K. Lu, and E. Ma, "Melting mechanisms at the limit of superheating," Phys. Rev. Lett. **87**, 055703:1- 4 (2001).

[23]   M. Born, "Thermodynamics of crystals and melting," J. Chem. Phys. **7**, 591-603 (1939).

[24]   J. Wang, J. Li, S. Yip, D. Wolf, and S. Phillpot, "Unifying two criteria of Born: elastic instability and melting crystals of homogeneous crystals," Physica A **240**, 396-403 (1997).

[25]   A. Kanigel, J. Adler, and E. Polturak, "Influence of point defects on the shear elastic coefficients and on the melting temperature of Copper," Int. J. Mod. Phys. C **12**, 727-737 (2001).

[26]   J. Wang, S. Yip, S. R. Phillpot, and D. Wolf, "Crystalline instabilities at finite strain," Phys. Rev. Lett. **71**, 4182-4185 (1993).

[27]   J. Wang, J. Li, and S. Yip, "Mechanical instabilities of homogeneous crystals," Phys. Rev. B **52**, 12627-12635 (1995).

[28]   J. L. Tallon, "A hierarchy of catastrophe as a succession stability limits for the crystalline state," Nature (London) **342**, 658-660 (1989).

[29]   F. H. Stillinger and T. A. Weber, "Point defects in bcc crystals: structures, transition kinetics, and melting implications," J. Chem. Phys. **81**, 5095-5103 (1984).

[30]   L. Jacobst and H. Kleinert, "Monte Carlo study of defect melting in three dimensions," J. Phys. A: Math. Gen. **17**, L361-L365 (1984).

[31]   L. Burakovsky, D. L. Preston, and R. R. Silbar, "Melting as a dislocation-mediated phase transition," Phys. Rev. B **61**, 15011-15018 (2000).

[32]   K. Lu and Y. Li, "Homogenous nucleation catastrophe as a kinetic stability limit for superheated crystal," Phys. Rev. Lett. **80**, 4474-4477 (1998).

[33]   M. Iwamatsu, "Homogenous nucleation for superheated crystals," J. Phys. Condens. Matter. **11**, L1-L5 (1999).

[34]   F. D. Di Tolla, "Interplay of melting, wetting, overheating, and faceting on metal surfaces: theory and simulation," Surf. Sci. **377/379**, 499-503 (1990).

[35]   J. C. Heyraud and J. J. Mètois, "Surface free energy anisotropy measurement of indium," Surf. Sci. **177**, 213-220 (1986).

[36]   J. C. Heyraud and J. J. Mètois, "Equilibrium shape and temperature: lead on graphite," Surf. Sci. **128**, 334-342 (1983).

[37]   G. Bilalbegovic and E. Tosatti, "Incomplete melting of the Au(110) surface," Phys. Rev. B **48**, 11240-11248 (1993).

[38]   P. Carnevali, F. Ercolessi, and E. Tosatti, "Melting and nonmelting of the Au(111)surfaces," Phys. Rev. B **36**, 6701-6704 (2000). .

[39] E. A. Murphy and H. Elsayed-Ali, "Superheating of Pb(111)," Phys. Rev. Lett. **69**, 1228-1231 (1992).

[40] G. Bilalbegovic, "Structural and metastability of superheated Al(111)," Phys. Rev. B **55**, 16450-16454 (1992).

[41] B. Pluis, A. W. D. van der Gun, J. W. M. Frenken, and J. F. van der Veen, "Crystal-face dependence of surface melting," Phys. Rev. Lett. **59**, 2678-2681 (1987).

[42] M. Blackman, S. J. Peppiatt, and J. R. Samples, "Superheating of bismuth," Nat. Phys. Sci. **239**, 61-62 (1972).

[43] J. J. Mètois and J.C. Heyraud, "The overheating of lead crystals," J. Phys. (France) **50**, 3175-3179 (1989).

[44] M. F. Hochella, "Nanoscience and technology: the next revolution in the earth sciences," Earth and Planetary Sci. Lett. **203**, 593-605 (2002).

[45] T. P. Martin, "Shells of atoms," Phys. Rep. **273**, 199-241 (1996).

[46] G. L. Allen, R. A. Bayless, W. W. Gile, and W. A. Jesser, "Small particle melting of Pure metals," Thin Solid Films **144**, 297-308 (1986).

[47] Ph. Buffat and J.–P. Borel, "Size effect on the melting temperature of gold particles," Phys. Rev. A **13**, 2287-2298 (1976).

[48] T. Castro, R. Reifenberger, E. Choi, and R. P. Andres, "Size-dependent temperature of individual nanometer-sized metallic clusters," Phys. Rev. B **42**, 8548-8556 (1990).

[49] M. Zhang, M. Yu. Efremov, F. Schiettekatte, E. A. Olson, A. T. Kwan, S. L. Li, T. Wisleder, J. E. Greene, and L. H. Allen, "Size-dependent melting point

depression of nanostructures: Nanocalorimetric measurements," Phys. Rev. B **62**, 10548-10557 (2000).

[50]   K. K. Nanda, S. N. Sahu, and S. N. Behera, "Liquid-drop model for size dependent melting of low dimensional systems," Phys. Rev. A **66**, 013208 (2002).

[51]   H. Reiss, P. Mirable, and R. L. Whetten, "Capillarity theory for the coexistence of liquid and solid clusters," J. Phys. Chem. **92**, 7241-7246 (1998).

[52]   M. Wautelet, "Estimation of the variation of the melting temperature with the size of small particles, on the basis of a surface-phonon instability model," J. Phys. D: Appl. Phys. **24**, 343-346 (1991).

[53]   L. H. Liang, J. C. Li, and Q. Jiang, "Size-dependent melting depression and lattice contraction of Bi nanocrystals," Physica B **334**, 49-53 (2003).

[54]   Q. Jiang, L. H. Liang, and J. C. Li, "Thermodynamic superheating and relevant interface stability of low-dimentional metallic crystals," J. Phys.: Condens. Matter. **13**, 565-571 (2001).

[55]   M. Zhao, X. H. Zhou, and Q. Jiang, "Comparison of different models for melting point change of metallic nanocrystals," J. Mater. Res. **16**, 3304-3308 (2001).

[56]   D. A. Porter and K. E. Easterling, *Phase Transformation in Metals and Alloys*, Van   Nostrand Reinhold (UK) Co. Ltd, (Molly Millars lane, Wokingham, Berkshire, England, 1984).

[57]   Z. Zhou, W. Wang, and L. Sun, "Undercooling and metastable phase formation in a $Bi_{95}Sb_5$ melt," Appl. Phys. A **71**, 261-265 (2000).

[58]   S. Tabakova and F. Feuillebois, "On the solidification of a supercooled liquid droplet lying on a surface," J. Coll. & Interf. Sci. 272, 225-234 (2004).

[59]   X. Y. Liu, Generic mechanism of heterogeneous nucleation and molecular interfacial effects, in *Advances in Crystal Growth Research*, K. Sato, K. Nakajima, and Y. Furukawa, ed. (Elsevier Science B.V., Amsterdam 2001).

[60]   J. D. Gunton, "Homogeneous nucleation," J. Statist. Phys. 95, 903-923 (1999).

[61]   D. W Oxtoby, "Homogeneous nucleation: theory and experiment," J. Phys: Condens. Matter. 4, 7627-7650 (1992).

[62]   V. Talanquer and D. W. Oxtoby, "Nucleation on a solid substrate: a density functional approach," J. Chem. Phys. 104, 1483-1492 (1996).

[63]   R. M. Nyquist, V. Talanquer, and D. W. Oxtoby, "Density functional theory of nucleation: a semi-empirical approach," Chem. Phys. 103, 1176-1179 (1995).

[64]   P. Demo, A. M. Sveshnikov, K. Nitsch, M. Rodová, and Z. Kožíiek, "Determination of time characteristics of solidification of supercooled halied melts from measurements of its electrical," Mater. Phys. Mech. 6, 43-48 (2003).

[65]   J. Zhong, Z. H. Jin, and K. Lu, "Melting, superheating, and freezing behavior of indium interpreted a nucleation-and-growth model," J. Phys.: Condens. Matter. 13, 11443-11452 (2001).

[66]   L. Zhang, Z. H. Jin, L. H. Zhang, M. L. Sui, and K. Lu, "Superheating of confined Pb thin film," Phys. Rev. Lett. 85, 1484-1487 (2000).

[67]   J. Zhong, L.H. Zhang, Z. H. Jin, M.L. Sui, and K. Lu, "Superheating of Ag nanoparticles embedded in Ni matrix," Acta Mater. 49, 2897-2904 (2001).

[68] L. Grbåek, J. Bohr, E. Johnson, A. Johnson, L. Sarholt-Kristensen, and H. H. Andersen, "Superheating and supercooling of lead precipitates in aluminum," Phys. Rev. Lett. **64**, 934-937 (1990).

[69] H. W. Sheng, G. Ren, L. M. Peng, Z. Q. Hu, and K. Lu, "Superheating and melting point depression of Pb nanoparticles embedded in Al matrices," Phil Mag. Lett. **73**, 179-189 (1997).

[70] J. Daeges, H. Gleiter, and J. H. Perepezko, "Superheating of metal crystals," Phys. Lett. A **119**, 79-82 (1986).

[71] D. R. Uhlmann," On the internal nucleation of melting," J. Non-cryst. Solids **41**, 347-357 (1980).

[72] J. W. Herman and H. Elsayed-Ali, "Time-resolved structural studies of the low index faces of lead," Phys. Rev. B **49**, 4886-4897 (1994).

[73] E. A. Murphy, H. E. Elsayed–Ali, and J. W. Herman, "Superheating of Bi(0001)," Phys. Rev. B **48**, 4921-4924 (1993).

[74] G. D. T. Spiller, "Time dependent melting and superheating of lead crystallites," Phil. Mag. A **46**, 535-549 (1982).

[75] H. J. Fecht and W. L. Johnson, "Entropy and Enthalpy Catastrophe as a Stability Limit For Crystalline Material," Nature (London) 334, 50-51 (1988).

[76] M. Akyurt, G. Zaki, and B. Habeebullah, "Freezing phenomena in ice-water systems," Energy Conversion and Management **43**, 1773-1789 (2002).

[77] V. D. Aleksandrov and S. A. Frolova, "Supercooling of In_2Bi and InBi melts," Inorganic Mat. **40**, 227-230 (2004).

[78]   H. Y. Tong and F. G. Shi, "Dependence of supercooling of a liquid on its overheating," J. Chem. Phys. **107**, 7964-7966 (1997).

[79]   V. D. Aleksandrov and V. A. Postnikov, "The effect of sample mass on the crystallization supercooling in bismuth melt," Tech. Phys. Lett. **29**, 287-289 (2003).

[80]   S.V. Dukarov, "Size and temperature effects on wetting in supercooled vacuum condensates," Thin Solid Films **323**, 136-140 (1998).

[81]   D. D. Awschalom and J. Warnock, "Supercooled liquids and solids in porous glasses," Phys. Rev. B **35**, 6779-6785 (1987).

[82]   J. Warnock, D. D. Awschalom, and M. W. Shafer, "Geometric supercooling of liquids in porous glass," Phys. Rev. Lett. **57**, 1753-1756 (1986).

[83]   T. Takahashi and W. A. Tiller, "The supercooling dependence for nucleation of some metals on the liquid drop size," Acta Metall. **17**, 643-650 (1969).

CHAPTER III

REFLECTION HIGH-ENERGY ELECTRON DIFFRACTION

III.1. Introduction

Reflection high-energy electron diffraction (RHEED) has become an essential technique in many surface related areas. Unlike other techniques that give information on a particular local area of the surface, RHEED gives a statistical view over a large area of the top few monolayers of the surface with minimal interference with its intrinsic properties [1-5]. The high-energy electrons along with the nearly grazing incident angle results in a high elastic scattering cross-section, narrow penetration depth, and a fairly wide probed area, which makes RHEED an ideal surface sensitive technique for static and dynamic studies [1-3]. Static RHEED patterns can provide information on structure, orientation, and morphology for any crystalline surface [6-8]. On the other hand, real-time dynamic RHEED is used routinely to monitor the growth of thin and ultra-thin epitaxial layers [9-11]. The dynamic studies were also extended to include gas-surface interaction kinetics and surface chemistry [12]. Also, RHEED is considered among the most useful techniques to probe surface dynamics such as surface reconstruction, roughing, and surface melting, under conventional and laser heating [4-6].

The energetic RHEED electrons interact strongly with the periodic potential of the crystal surface atoms producing a powerful very sensitive structural characterization tool.[1-3] Unfortunately, this strong interaction may involve non-linear scattering processes such as multiple scattering, and excitations of surface plasmons, which make it difficult for the theory to account for [13]. Because of the diffraction complexities and the lack of

a precise theoretical realization of RHEED, qualitative information is normally extracted from the obtained data [2,3,14]. Since the RHEED theory is out of the scope of this dissertation, this chapter will briefly give an introduction to the fundamentals and basics of experimental RHEED along with the basic calculations used to interpret RHEED patterns. Information in this chapter is used to index RHEED patterns of bismuth, indium, and graphite in the reflection and the transmission modes as shown in appendix A and B.

III.2. Basic RHEED setups and operations

The simple setup, easy operation, low maintenance costs, ability for *in situ* monitoring, compatibility with vacuum deposition reactors and processes, and the high surface sensitivity are the reasons behind RHEED popularity among the surface science community [1-3]. The main parts of any standard RHEED system are: an electron gun with a high voltage source, a phosphor screen, an image capturing camera and software for image analysis. Medium to ultra-high vacuum environment is also needed for operation, however, high pressure RHEED was also developed [15]. For high-pressure operation, the traveling path of the electrons in the high-pressure region is kept as short as possible to minimize scattering losses. Fig. 3.1 shows a schematic diagram of typical RHEED components.

The electron gun produces a collimated nearly mono-energetic (5-100 keV) electron beam that strikes the crystal surface at a grazing incident angle ($\leq 5°$). These electrons are scattered by the periodic potential of the crystal surface, which results in a characteristic diffraction pattern of the surface that is displayed on the phosphor screen. The pattern is then captured with a suitable charge-coupled device (CCD) camera. By changing the incident and azimuth angles or by rocking the sample to change the electron

angle of incident, valuable information on the average long-range order of the top surface layers of the sample could be obtained. For example, when RHEED intensity is measured as a function of the glancing angle, which is called RHEED rocking-curve, detailed information about the surface potential and the atomic position up to a few layers underneath the surface can be obtained [16]. In dynamic studies, manual changing of the glancing angle is inconvenient; therefore, a RHEED apparatus with a magnetic deflector composed of two pairs of magnetic coils has been developed [17-19]. A computer algorithm was then used to control the electron path and allow rapid and accurate measurement of the rocking curves [17]. Structural phase transition and thermal vibration of surface atoms were studied [17-19].
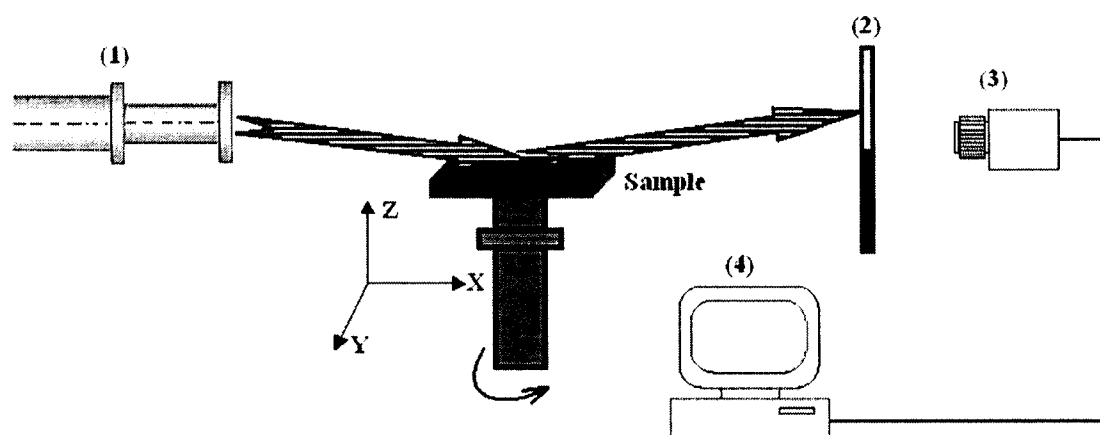
FIG. 3.1. Schematic diagram of the basic RHEED components, 1) electron gun, 2) phosphor screen, 3) CCD camera, and 4) software image analyzer.

For qualitative RHEED analysis, rocking curves are usually measured either by tilting the sample or by rocking the electron beam. Convergent-beam RHEED (CB-RHEED) is an alternative way to obtain a rocking curve in single shot RHEED pattern

[20,21]. The incoming beam is focused onto the sample forming a cone-like incident beam. The CB-RHEED pattern contains many diffracted orders for each incidence angle and azimuth within the illuminating cone. The drawback of CB-RHEED is that two-dimensional image recording is required, and an imaging energy filter is necessary to utilize the advantage of parallel detection [20].

In some RHEED applications, an energy filter is added to separate the inelastic diffuse background from the elastic contribution of the scattered electrons [22]. This energy filtering improves the shape of the RHEED patterns and increases the signal-to-background ratio. The improved RHEED pattern along with electron energy loss spectroscopy measurements can be used to *in situ* measure the chemical states and/or chemical composition of some surfaces and interfaces [22]. Time-resolved RHEED is another RHEED modification that provides the ability to monitor the evolution of the surface structure, morphology, and temperature during a fast laser-initiated transition or during ultra-thin film deposition [23,24]. In pomp-probe time resolved RHEED, a photo activated RHEED electron gun, instead of conventional continues filament based gun, is used to generate an electron pulse that is synchronized with a heating laser pulse. Using a beam splitter, a laser beam is split into two parts, one is used for heating the sample, pump, and the other is converted into UV by nonlinear crystal and used for the photo-cathode of the RHEED gun for electron beam generation. By changing one of the laser paths, pump or probe, one can capture images before, during, and after laser surface heating. The temporal evolution of the diffraction intensity is monitored to obtain information on the mean-square vibrational amplitude of the surface atoms and the structural integrity of the surface.

III.3. Laue condition and RHEED patterns

RHEED diffraction patterns are produced when the scattered electrons satisfy simultaneously the conditions of constructive interference and elastic scattering [1-3]. In other words, the path difference between the scattered interfering beams is a multiple integers of its wavelength and that the incident and diffracted beam momentums are equal. For energetic electrons as in RHEED, the relativistic electron wavelength λ, measured in Å, is given by the following expression [3],

$$\lambda = \frac{h}{\sqrt{2m_0 qV + \left(\frac{qV}{c}\right)^2}} \cong \frac{12.3}{\sqrt{V(1 + 1.95 \times 10^{-6}V)}},$$

(3.1)

where m_0 is the electron rest mass, q is its charge, and V is the accelerating potential measured in volts. Considering the scattering geometry shown in Fig. 3.2, the elastic scattering condition can be generally written as,

$$\left|\delta_1 \hat{n}_i\right| + \left|\delta_2 \hat{n}_s\right| = m \lambda .$$

(3.2)

Where $\hat{n}_i$ and $\hat{n}_s$ are unit vectors in the incident and scattering directions respectively, and δ_i and δ_s are scalar distances. By finding the values of the scalar distances δ_i and δ_s from the scattering geometry of Fig. 3.2, Eq. (3.2) becomes,

$$d_{hkl} \cos \theta_i + d_{hkl} \cos \theta_s = m \lambda .$$

(3.3)

If the reciprocal space is considered, the wave vector K_j where $K_j = \frac{2\pi}{\lambda} \hat{n}_j$, j $= i$ or s, can be taken to represent the beam momentum and direction, and the interplaner distance vector d_{hkl} is then equivalent to the reciprocal lattice vector G_{hkl}, normal to the surface

but with lower magnitude such that $G_{hkl} = \dfrac{2\pi}{d_{hkl}}$. The reciprocal space formulation of Eq.

(3.3) could be deduced such that,

$$|K_i| \ |G_{hkl}| \cos\theta_i + |K_s| \ |G_{hkl}| \cos\theta_s = m \text{ , or} \tag{3.4}$$

$$-K_i \bullet G_{hkl} + K_s \bullet G_{hkl} = m \text{ .} \tag{3.5}$$

The negative sign is simply because K_i has a negative component in the G_{hkl} - direction,

and the dark dot sign is used to indicate the dot product.
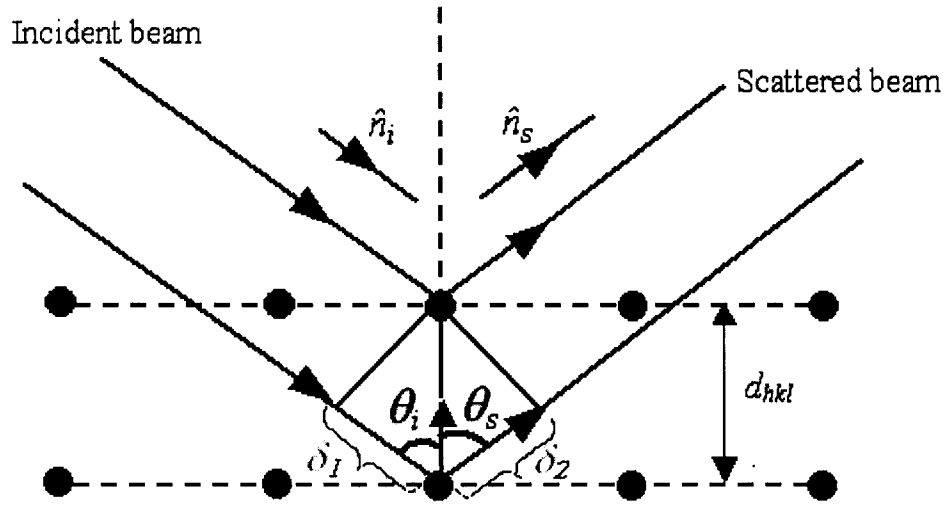
FIG. 3.2. A schematic representation of an elastic scattering process in real space. The necessary condition for constructive interference is that the path difference between the incident and scattered beam equal to an integer multiple of the wavelength of the scattered beam.

Eq. (3.5) can be written in a simplified form as,

$$\Delta K \bullet G_{hkl} = m , \tag{3.6}$$

where $\Delta K = K_s - K_i$. Thus, the bright spots observed at the phosphor screen are an

arrangement of points in the reciprocal space governed by Laue condition, Eq. (3.6). This

condition emphasizes the quantization or periodicity of the ΔK component in the G_{hkl}

direction, and that ΔK is in parallel direction to G_{hkl}. In other words, the possible

changes in the wave vector matches the periodicity of the reciprocal lattice vector. For

some proposes the right hand side of Eq. (3.6) is taken to be $2m\pi$ to represent the phase

periodicity of the scattering wave. Using a simple scattering geometry in the reciprocal

space, Fig. 3.3, one can directly get to the same Laue condition such that,

$$K_s = K_i + G_{hkl}, \text{ where } G_{hkl} = mG_{hkl}, \tag{3.7}$$

Thus $\Delta K = G_{hkl}$. $\tag{3.8}$
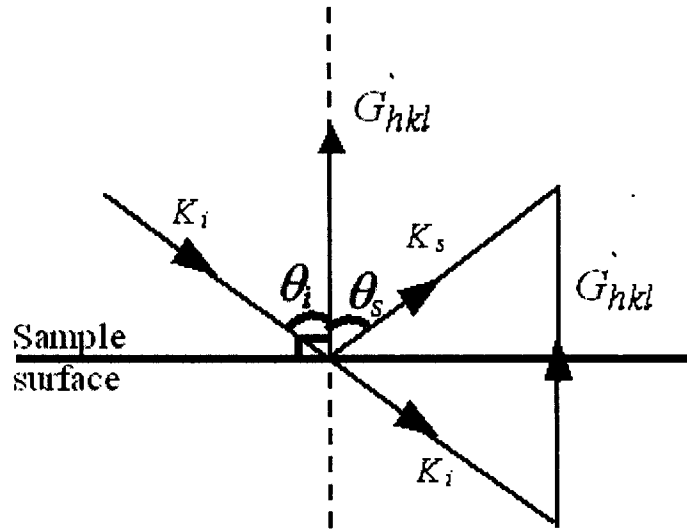
FIG. 3.3. A geometrical representation of the scattering process in the reciprocal space. The illustration shows the necessary condition for constructive interference, $\Delta K = G_{hkl}$.

III.4. Static RHEED analysis

III.4.1 Surface orientation

As mentioned before, a RHEED pattern is the intersection of the reciprocal lattice

rods with the Ewald sphere projected on the phosphor screen. Provided that the radius of

the Ewald sphere is much larger than the inter-rods distances, one can use the principle of

similar triangles to relate the streak spacing on the screen to its corresponding lateral rod

spacing in the reciprocal space [3,14]. Fig. 3.4 is a schematic diagram showing a plane view of the relation between the inter-spacing of the reciprocal lattice rods of the zeroth order and the spacing of the observed RHEED streaks. The zeroth order Laue zone is defined as the rods along the direction perpendicular to the incident beam that contains the origin. The origin is the point at which the electron beam hits the surface. By utilizing the principle of similar triangle, using Fig. 3.8, one can find that $W/L \approx a^*/|K_j|$, and the reciprocal lattice vector $\underline{a}^*$ is then given by:

$$a^* = \frac{2\pi W}{\lambda L} , \qquad (3.9)$$
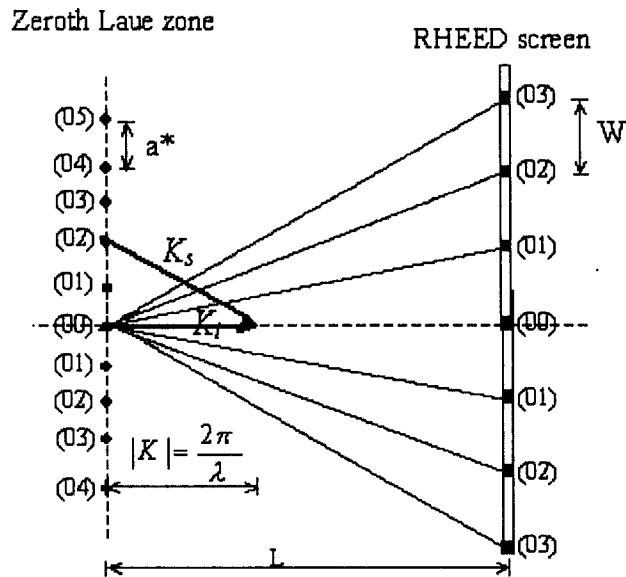
FIG. 3.4. The relation between the inter-spacing of reciprocal lattice rods of the zeroth order and the spacing of the observed RHEED streaks, one can use the principle of similar triangle to find the azimuthal orientation of the sample relative to the beam incident direction, [After Ref. 3].

where W is the streak separation, L is the sample to screen distance, λ is the electron wavelength. Surface orientation at a particular azimuth of the sample with respect to the incident beam can be determined. Moreover, azimuthal plots, set of intensities of a diffracted beam measured at fixed polar angle while the azimuthal angle is varied, and rocking curves are used to determine the atomic arrangement at the surface and surface symmetry [2,3,14,17].

III.4.2. Surface morphology

For surface scattering, where the diffraction pattern results from two-dimensional (2D) lattice structure, the reciprocal lattice net is a set of infinitely long rods extending normal to the surface and having the periodicity of the surface unit mesh [25]. Conceptually, elastic scattering condition is satisfied at a sphere of radius $(2\pi/\lambda)$, Ewald sphere, and Laue condition of constructive interference is satisfied at the intercepts of Ewald sphere with the reciprocal lattice rods where $\Delta K = G_{hkl}$. Thus, RHEED pattern is the projection of the intercepts of the Ewald sphere with the 2D reciprocal lattice rods on the screen. Figure 3.5(a,b) shows a side and a top view of the Ewald sphere-reciprocal rods intercepts and their projections on a RHEED screen. For a perfect surface, RHEED pattern is expected to consist of spots lying on an arc (Laue ring), arising from such intersection, Fig. 3.5(c). The spots tend to be streaked to some extent because the radius of Ewald sphere is much larger than the inter-rod spacing for typical RHEED energies [2]. Moreover, thermal vibrations, lattice imperfections, and instrumental effects cause the reciprocal lattice rods to have a finite thickness, while the Ewald sphere itself has some finite thickness, due to divergence and dispersion of the electron beam [6].
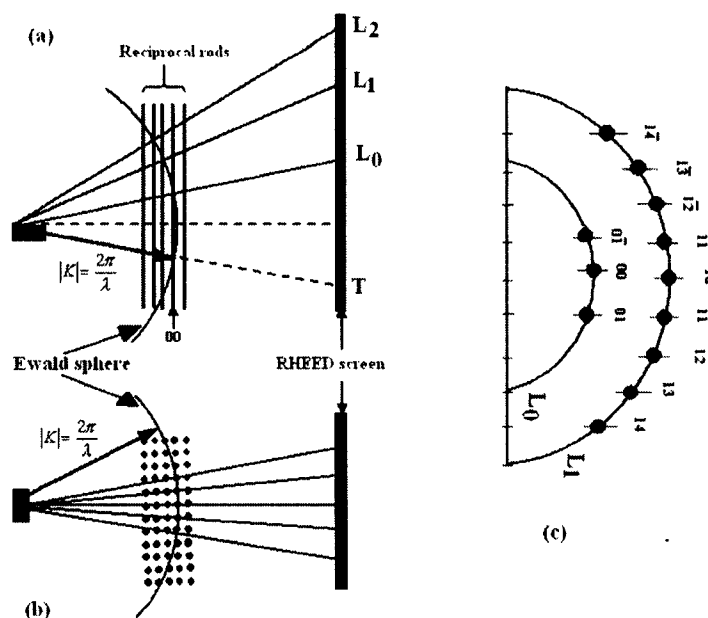
FIG. 3.5. Side view, (a), and top view, (b), of the Ewald sphere-reciprocal rods intercepts and their projection on a RHEED screen. (c) RHEED pattern of a perfect surface, spots arranged in an arcs (Laue rings, L_i and i is the zone order) arising from such intersection where the condition of elastic scattering and constructive interference is satisfied [After Ref. 1,3,14].

While the RHEED pattern of a perfect surface consists of spots located on a circumference of Laue rings, a rough surface or a non-clean surface may show patterns consisting of many spotty features due to the electron transmission through surface asperities or adatom clusters [2,3]. Furthermore, RHEED from an amorphous surface gives a pattern with no diffraction features, only a diffuse background is observed. Therefore, the first important information provided by RHEED, without any calculation, is about the flatness and perfection of the crystalline surfaces. Like many diffraction techniques, RHEED can also differentiate between single crystal and polycrystalline surfaces. Spots arranged in half circles are observed for single crystal surfaces, while concentric half rings are observed in the case of polycrystalline surfaces [26]. Rings with uniform intensity

mean that the grains are randomly oriented, however, if the polycrystalline film

exhibits a fiber-like texture, broken rings are expected instead [26]. Figure 3.6

schematically summarizes some of these surface morphologies and their expected

RHEED patterns.
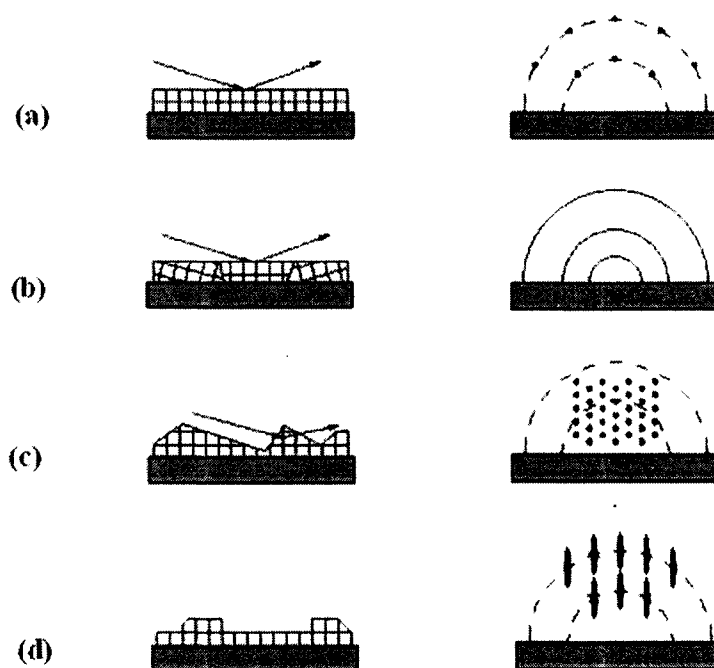
FIG. 3.6. Schematic illustration of some different surface morphologies and its expected RHEED pattern; a) spots on Laue rings for atomically flat surface, b) concentric rings for polycrystalline or randomly oriented crystallites, c) transmission like pattern, spots arranged in a line or in a special shape, for three-dimension oriented asperities, and d) elongated streaks on Laue rings for two-dimension crystallites, [After Ref. 2].

III.4.3. Transmission RHEED

Because of the glancing incidence of RHEED, the component of the electron

momentum perpendicular to the surface is small and so is the normal penetration depth

[3]. Also, the forward electron scattering is increased and the electrons travel a

substantial distance through the solid, in according with their mean free path. Since the

path-length of RHEED electrons is relatively high, few nm in metallic crystals, the

electron beam may pass through small surface features and cause true bulk-like diffraction. A transmission spot pattern that has no relation to the surface Laue rings, but represents a cut through the reciprocal lattice of the asperite structure, can be clearly distinguished. In this context, RHEED probes only a layer given by its inelastic mean free path (IMFP). The IMFP represents the average path length that an electron travels between two successive inelastic interactions [27]. IMFP depends on the electron kinetic energy and the nature of the solid traveling through. However, most elements show similar IMFP-electron energy dependence [28]. A general equation for the IMFP is given by [27,28],

$$\lambda_i = \frac{E}{E_p^2 \left(\beta \ln(\gamma E) - \dfrac{C}{E} + \dfrac{D}{E^2} \right)} \, . \tag{3.10}$$

At energies above 100 eV Eq. (3.4) reduces to [27],

$$\lambda_i = \frac{E}{E_p^2 \beta \ln(\gamma E)} \, , \tag{3.11}$$

where, λ_i is the IMFP, E is the energy, $E_p = \sqrt{\rho N_v / M}$ is the generalized plasmon energy, N_v is the number of valence electrons (per atom or molecule), ρ is the density of the material and M is the atomic mass. The material dependent constants β, γ, C, and D can be estimated from measurable quantities of the material using empirical or semi-empirical theoretical expressions [28]. Even though there was no physical justification for universality, the IMFP-electron energy curve became known as the IMFP "universal curve". Figure 3.7 shows the IMFP-electron energy curves calculated for graphite, indium, and bismuth, constants β, γ, C, and D are calculated based on the empirical relations given in Ref. [28]. Electrons with ~10 keV energy would be able to penetrate

islands or aspirites with ~ 10 nm width of graphite, indium, or bismuth without

significant loss due to inelastic collisions. Transmission RHEED can probe only an over-

layer of ~10 nm maximum dimension, in the electron traveling path direction, of these

systems.
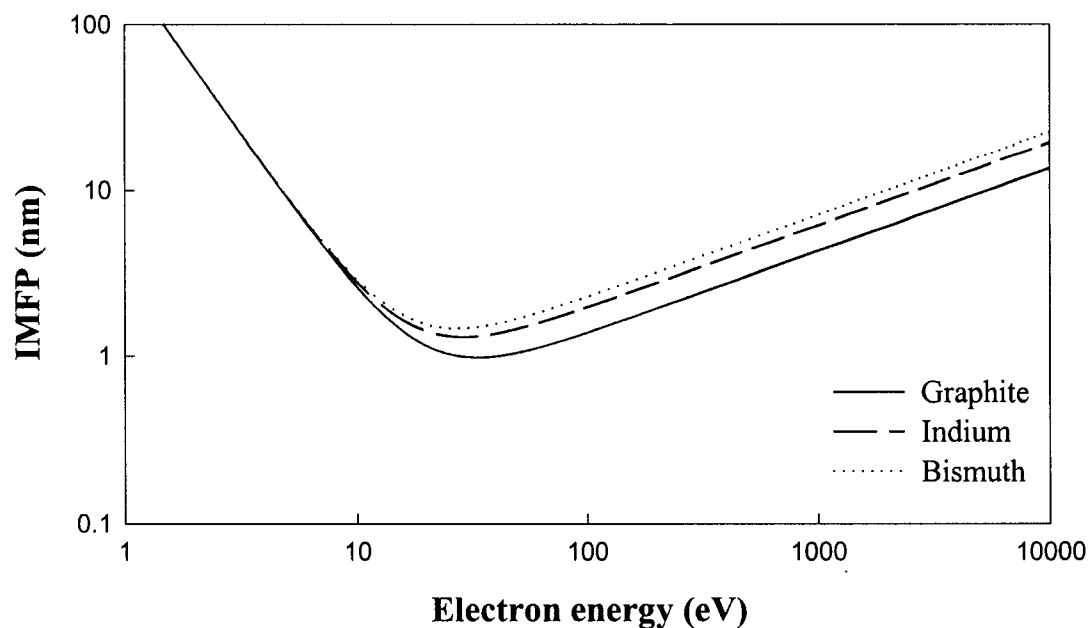
FIG. 3.7. A log-log plot of the IMFP variation with electron energy as calculated for graphite, indium, and bismuth.

Transmission RHEED patterns can be used to obtain structural information on

rough surfaces and 3D-island films. The patterns are similar to those obtained by the

selected area electron diffraction (SAED), where the transmission electron microscope

(TEM) is switched to the diffraction mode and a small area aperture is used to selectively

obtain a transmission diffraction pattern of a particular location of a very thin sample. [29]

In the case of transmission RHEED, only half of the diffraction spots are seen, the other

half is covered by the crystal shadow. Fig. 3.8 shows a schematic representation of

transmission-reflection geometry of RHEED. The spots in the transmission RHEED

patterns are formed according to Bragg's condition, however, because θ is very small and

$\sin\theta \cong \theta$ in radian, Bragg's equation is rewritten as [29],

$$2d_{hkl} \cdot \theta_{hkl} = \lambda. \qquad (3.12)$$
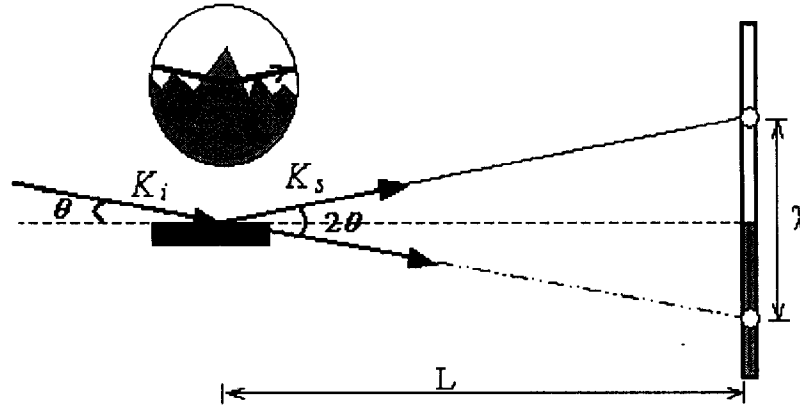
FIG. 3.8. A schematic diagram represents the transmission-reflection geometry of RHEED.

From the geometry of transmission RHEED, Fig. 3.7, the angle θ can be related to the

origin-to-spot distance χ, using the approximation of $\tan\theta \cong \theta$ in radian, as

$$2\theta_{hkl} = \frac{\chi}{L}, \qquad (3.13)$$

where L is the sample-to-screen distance. The interplaner distance, d_{hkl}, of a particular

set of planes, represented by a single spot on the screen, can be estimated as

$$d_{hkl} = \frac{\lambda L}{\chi}. \qquad (3.14)$$

By measuring the spot-to-origin distances, the value of the interplaner distances, d_{hkl}, of

a different family of planes within the diffraction zone can be obtained. The diffraction

zone is the zone that contains two or more diffraction planes satisfying the zone equation [29],

$$hu + kv + lw = 0,$$ (3.15)

where (hkl) is any plane located in the $[uvw]$ zone. The electron beam is taken to be parallel to the axis of the zone. This means that only the planes that make right angles with the direction of the electron beam will be seen. It is clear that changing the zone axis, through changing the azimuthal orientation of the crystal, changes the diffraction pattern. However, low symmetry crystals may have many zones that look very similar to each other. Diffraction patterns attained at two or more zone axes are necessary for unambiguously correct and accurately index. The indexing can be done manually using the stereograph or automatically by using a computer program. A manual indexing procedure is discussed in appendix B for crystals with prior knowledge of their crystal structures.

III.5. Dynamic RHEED

The RHEED ability to resolve and detect the atomic arrangement of the surface arises from the fact that a RHEED pattern represents a cut through the surface reciprocal lattice rods. Surface structural modifications, either by surface defect formation or by adatoms deposition, will alter the arrangement of these rods. This will directly appear as a change in the spot intensity or in the shape of the diffraction pattern. RHEED patterns are widely used to study the surface [4,7,8].

Based on the operating condition and surface morphology, the RHEED pattern can be obtained either at the in-phase or at the out-of-phase conditions [2]. At the in-phase condition the diffraction pattern is most sensitive to surface order, while at the out-

of-phase condition RHEED is more sensitive to lattice defects [30]. In the in-phase condition, the angle of incidence and electron energy are set such that the electrons scattered from surface layers separated by one atomic step interfere constructively. At this condition, the change in the specular spot intensity is sensitive to the order within the topmost layers of the probed surface. Indeed, the temporal change of the specular intensity has been effectively used to control film thickness within an atomic layer using the well-known phenomenon of RHEED oscillations [9-11]. RHEED oscillations indicate layer-by-layer film growth where the maximum of the RHEED intensity is reached when the growing film form a complete well-ordered monolayer (ML) film. The intensity continuously decays if the growing film forms 3D islands [31]. The pattern is then transferred from spots/streaks arranged on a Laue ring to a transmission spot array reflecting the crystal symmetry of the deposited film. The evolution of randomly oriented or oriented 3D clusters continuously decreases the RHEED intensity attributed to surface diffraction.

When RHEED incident angle θ is made such that $2d\sin\theta = (n+1/2)\lambda$, where d is the monolayer step height, λ is the electron wavelength, and n is an integer, the electrons scattered from regions differing in height by 1 ML are 180° out of phase and interfere destructively. In this out-of-phase condition, RHEED pattern is more sensitive to the surface defects. In electron diffraction experiments, the electron-phonon interaction and the elastic scattering of electrons from surface defects such as steps, vacancies, and disordered adatoms appear as diffused intensity background in the diffraction pattern [32,34]. The diffuse intensity background can be measured in RHEED and low energy electron diffraction (LEED) experiments using the ratio R, which is defined as [34],

$$R = \frac{I_{back}}{I_{peak} - I_{back}}.$$ (3.16)

Where I_{back} is the RHEED background intensity measured at a location away from the diffraction peaks, and I_{peak} is the peak intensity of a diffraction order. Under the out-of-phase condition the ratio R is found to be very sensitive to surface defects while almost independent of defect density if it is measured in the in-phase condition.[34] By measuring the background ratio R, the adatom/vacancies density can be estimated as a function of temperature. The background intensity or surface defect density in terms of the ratio R is normally used to probe surface phase transitions such as roughing and surface melting [4,35,36].

In addition to the structural sensitivity, the RHEED pattern is also sensitive to temperature. The scattered electrons are influenced by the vibrational motion of the surface atoms resulting in a decrease in the spot intensity as the temperature is increased. This is because the intensities measured include elastic as well as inelastic electron scattering such as phonon scattering. The effect of thermal vibration on elastically diffracted electrons was accounted for in the Debye-Waller theory, as in x-ray diffraction. For $T \gg \Phi_D$, Φ_D is the Debye temperature, the intensities in the Bragg peaks fall off exponentially such that [37,38],

$$I = I_0\, e^{-2M}$$ (3.17)

Where I and I_0 are the intensity of the diffracted beam at temperature T and for the rigid lattice, respectively. This equation predicts intensity decreased by a factor of e^{-2M}, called Debye-Waller factor, as the temperature increases due to electron diffuse scattering. M is a quantity dependent on the characteristics of the crystal, electron wavelength, and the

angle of scattering. For the independent harmonic approximation, the exponent $2M$ is

related to the mean-square lattice vibrational amplitude $\langle \upsilon \rangle^2$ such that,

$$2M = |\Delta K|^2 \langle \upsilon \rangle^2, \tag{3.18}$$

where ΔK is the change in electron wave vector due to scattering. At the high

temperature limit, $\langle \upsilon \rangle^2$ is given by [39],

$$\langle \upsilon \rangle^2 = \frac{3N\hbar^2}{mk_B} \frac{T}{\Phi_D}, \tag{3.19}$$

where N is the Avogadro's number, $\hbar$ is Planck's constant divided by 2π, m is the atomic

mass, k_B is Boltzmann's constant, and T is the absolute temperature. Equations (3.17)-

(3.19) are normally applied to estimate the surface temperature from the intensity of the

RHEED pattern after proper calibrations [40,41]. In fact, the RHEED intensity offers an

in situ non-contact temperature measuring technique that can work efficiently for clean

surfaces in many situations such as film growth and surface processing. RHEED intensity

can also be used to measure the surface transient temperature in laser heating where the

temperature raise is very fast and RHEED response almost simultaneously. By measuring

the normalized RHEED intensity of the specular spot as a function of surface temperature

using conventional heating, the transient surface temperature due to laser irradiation can

be estimated.

III.6. References of chapter III

[1] W. Braun, in "*Applied RHEED: reflection high-energy electron diffraction during Crystal growth,*" Springer, Berlin, (1999).

[2] M. G. Lagally, D. E. Savage, and M. C. Tringides, in "*Reflection high-energy electron diffraction and reflection electron imaging of surfaces*", ed. P. K. Larsen, Plenum, New York (1988).

[3] J. E. Mahan, K. M. Geib, G. Y. Robinson, and R. G. Long, "A review of the Geometrical Fundamentals of reflection high-energy electron diffraction with application to silicon surface," J. Vac. Sci. Technol. A8, 3692-3700 (1990).

[4] B. Lin and H. Elsayed-Ali, "Temperature dependent reflection electron diffraction study of In(111) and observation of laser induced transient superheating," Surf. Sci. 498, 275-284 (2002).

[5] Z. H. Zhang, P. Kulatunga, and H. E. Elsayed-Ali, "Reflection high-energy electron-diffraction study of melting and solidification of Pb on graphite," Phys. Rev. B 56, 4141-4148 (1997).

[6] B. A. Joyce, J. H. Neave, B. J. Dobson, and P. K. Larsen, "Analysis of reflection high-energy electron diffraction data from reconstructed semiconductor surfaces," Phys. Rev. B 29, 814-819 (1984).

[7] Q. Fu, E. Tchernychova, and T. Wagner, "Texture of molybdenum thin films on $SrTiO_3(100)$: a RHEED study," Surf. Sci. 538, L511-L517 (2003).

[8] S. Jo, Y. Gotoh, T. Nishi, D. Mori, and T. Gonda, "Surface structures of lead deposited on Mo(110) surface," Surf. Sci. 454-456, 729-735 (2000).

[9]   J. Massies and N. Grandjean, "Real-time control of the molecular beam epitaxy of nitrides," J. Crys. Growth **201-202**, 382-387 (1999).

[10]   J. R. Arthur, "Molecular beam epitaxy," Surf. Sci. **500**, 189-217 (2002).

[11]   B. A. Joyce and T. B. Joyce, "Basic studies of molecular beam epitaxy: past, present and some future directions," J. Cryst. Growth **264**, 605 -619 (2004).

[12]   B. A. Joyce, N. Ohtani, S. M. Mokler, T. Shitara, J. Zhang, J. H. Neave, and P. N. Fawcett, "Applications of RHEED to the study of growth dynamics and surface chemistry during MBE," Surf. Sci. **298**, 399-407 (1993).

[13]   H. Nakahara, T. Hishida, and A. Ichimiya, "Inelastic electron analysis in reflection high-energy electron diffraction condition," Appl. Surf. Sci. **212-213**, 157–161 (2003).

[14]   M. Dabrowska-Szata, "Analysis of RHEED pattern from semiconductor surfaces," Mat. Chem. Phys. **81**, 257–259 (2003).

[15]   D. H. A. Blank, G. J. H. M. Rijnders, G. Koster, and H. Rogalla, "In-situ monitoring during pulsed laser deposition using RHEED at high pressure," Appl. Surf. Sci. **127**, 633–638 (1998).

[16]   N. L. Yakovlev, P. A. Maksym, and J. L. Beeby , "Ionic potential analysis of RHEED rocking curves from fluoride structures," Surf. Sci. **529**, 319-328 (2003).

[17]   Y. Shigeta and Y. Fukaya, "Structural phase transition and thermal vibration of surface atoms studied by reflection high-energy electron diffraction," Surf. Sci. **237**, 21-28 (2004).

[18] Y. Shigeta, Y. Fukaya, H. Mitsui, and K. Nakamura, "Observation of RHEED rocking curves during Si/Si(111) film growth," Surf. Sci. **402-404**, 313- 317 (1998).

[19] Y. Fukaya and Y. Shigeta, "Fast measurement of rocking curve of reflection high-energy electron diffraction by using quasi-1D convergent beam," Surf. Sci. **530**, 175-180 (2003).

[20] J. M. Zuo, U. Weierstall, L. M. Peng, and J. C. H. Spence, "Surface structural sensitivity of convergent-beam RHEED: Si(001)2×1 models compared with dynamical simulations ," Ultramicroscopy **81**, 235-224 (2000).

[21] U. Weierstall, J. M. Zuo, T. Kjørsvik, and J. C. H. Spence, "convergent-beam RHEED in a dedicated UHV diffraction camera and applications to Si reconstructed surfaces," Surf. Sci. **442**, 239-250 (1999).

[22] P. Staib, W. Tappe, and J. P. Contour, "Imaging energy analyzer for RHEED: energy filtered diffraction patterns and In-situ electron energy loss spectroscopy," J. Crys. Growth **201**, 45-49 (1999).

[23] X. Zeng and H. E. Elsayed-Ali , "Time-resolved electron diffraction study of the Ge(100)-(2×1)-(1×1) phase transition," Surf. Sci. **497**, 373-384 (2002).

[24] P. Sandström, E. B. Svedberg, J. Birch, and J.-E. Sundgren, "Time-resolved measurements of the formation of single-domain epitaxial Ni films on MgO(111) substrates using in-situ RHEED analysis," Surf. Sci. **437**, L767–L772 (1999).

[25] A. Zangwill, *"Physics at Surfaces,"* Cambridge university press, Great British (1996).

[26]   S. Andrieu and P. Frechard, "What information can be obtained by RHEED applied on polycrystalline films?" Sur. Sci. **360**, 289-296 (1996).

[27]   W. S. M. Werner, C. Tomastik, T. Cabela, G. Richter, and H. Störi, "Electron inelastic mean free path measured by elastic peak electron spectroscopy for 24 solids between 50 and 3400 eV," Surf. Sci. **470**, L123-L128 (2000).

[28]   J. Powell, A. Jablonski, I. S. Tilinin, S. Tanuma, and D. R. Penn, "Surface sensitivity of auger-electron spectroscopy and x-ray photoelectron spectroscopy," J. Elect. Spect. Rel. Phen. **98-99**, 1-15 (1999).

[29]   M. De Graef, *"Introduction to conventional transmission electron microscope,"* UK university press, Cambridge, (2003).

[30]   P. I. Cohen, P. R. Pukite, J. M. Van Hove, and C. S. Lent, "Refelction high energy electron diffraction studies of epitaxial growth on semiconductor surfaces," J. Vac. Sci. Technol. A **4**, 1251-1258 (1986).

[31]   N. C. Holland, "A simple model for MBE growth controlled by group III atomic migration," J. Cryst. Growth **251**, 29-34 (2003).

[32]   G. Meyer-Ehmsen, "Real-space dynamic calculation of diffuse RHEED intensities from disordered surfaces," Surf. Sci. Lett. **395**, L118-L195 (1998).

[33]   H.-.N. Yang and T.-M. Lu, "Enhancement of thermal diffuse scattering by surface defects," Phys. Rev. B **44**, 11457-11464 (1991).

[34]   H.-.N. Yang, K. Fang, G.-C. Wang, and T.-M. Lu, "Vacancy induced disordering in the Pb(100) surface," Phys. Rev. B **44**, 1306-1310 (1991).

[35]   K. A. Elamrawi, M. A. Hafez, and H. E. Elsayed-Ali, "Atomic hydrogen-cleaned GaAs(100) negative electron affinity photocathode: surface studies with reflection

high-energy electron diffraction and quantum efficiency," J. Vac. Sci. Technol. A
18, 951-955 (2000).

[36]   Z. H. Zhang and H. E. Elsayed-Ali, " Surface morphology of laser superheated
Pb(111) ," Surf. Sci. **405**, 271-279 (199).

[37]   R. J. Weiss and C. Wilkinson, "The specific Debye-Waller factor and a search for
Antiferromagnetism in vanadium," J. Phys.: Condens. Matter **1**, 8319-8326
(1989).

[38]   J. D. Axe, "Debye-Waller factors for incommensurate structures," Phys. Rev. B
21, 4181-4190 (1980).

[39]   R. Lüscher, T. Flückiger, M. Erbudak, and A. R. Kortan, "Debye temperature of
the pentagonal surface of the quasicrystal Al-Pd-Mn," Surface Science **532-535**,
8-12 (2003).

[40]   P. Mazurek, A. Daniluk, and K. Paprocki, "Substrate temperature control from
RHEED intensity measurements," Vacuum **72**, 363-367 (2004).

[41]   V. P. LaBella, D. W. Bullock, C. Emery, Z. Ding, and P. M. Thibado, "Enabling
electron diffraction as a tool for determining substrate temperature and surface
morphology," Appl. Phys. Lett. **79**, 3065-3067 (2001).

CHAPTER IV

MELTING AND SOLIDIFICATION OF INDIUM NANOCRYSTALS

IV.1. Introduction and literature survey

The study of melting of metallic nanocrystals is of interest to fundamental understanding of the effect of reduced size and crystal shape on the melting phase transition [1-3]. The melting of nanocrystals that are free-standing, deposited on an inert substrate, embedded in a host matrix, or coated with a higher melting material have been theoretically and experimentally studied [1-14]. These nanocrystals showed structural as well as thermodynamical properties that are different from that of their own bulk materials. Some nanocrystals that are free standing or deposited on an inert substrate showed size-dependent melting point depression, in quantitative agreement with phenomenological thermodynamic models [2,5-7]. However, in other cases considerable superheating of some nanocrystals above the equilibrium bulk melting point was observed [1,3,8,9]. Embedded or coated nanocrystals have also shown a size-dependent melting point depression, in some cases, as well as several degrees superheating in others [10-14].

Melting point depression in nanocrystals and its dependence on the particle size are well demonstrated using different experimental techniques. Nanocalorimetric measurements of discontinuous indium and tin films, evaporated on amorphous silicon nitride, revealed that the melting point depression decreased linearly with the inverse of the particle size [5,15]. Indium nanocrystals showed a melting point depression by as much as 110 K for particles with 2-nm radius [5]. Scanning tunneling microscopy (STM)

and atomic force microscopy (AFM), combined with perturbed angular correlation, were used to study the melting of an ensemble of indium nanocrystals deposited on WSe_2 and Ge(100) [16,17]. The melting point was found to decrease as the mean film thickness was reduced. A reduction in the melting point as well as strong supercooling is observed for indium films deposited on Ge(100) [17]. Tsuboi *et al.* measured the size dependence of the melting point of lead thin films deposited on Al and Ge using differential scanning calorimetry [18]. They observed melting point depression as the film thickness decreased and the substrate type hardly affected the behavior. An *in situ* electron microscopy study showed that the melting point depression of indium particles deposited on cleaved MoS_2 is less than that deposited on amorphous carbon for particles of the same size [19]. *In situ* x-ray diffraction of Pb nanocrystals deposited on Si(532) showed that the melting point is inversely proportional to the average crystallite size [20]. The nanocrystals melting temperature T_m, normalized to that of the bulk, was related to the Pb crystallite diameter D by the equation $T_m = 1 - 0.62/D$ (nm). Melting point depression was also observed for gold and silver nanoclusters deposited on W(110) using field-emission current from individual clusters [6].

In addition to the abovementioned studies showing melting point depression of nanocrystals grown on different substrates, there are reports of superheating of crystallites grown on relatively inert substrates, such as graphite or carbon [8,9,21-23]. Melting of bismuth and lead thin films, consisting of individual crystallites, ware investigated using scanning electron microscopy. Depending on the individual crystallite shape, some showed a time delay sufficient to be superheated up to 7 K and 2 K for bismuth and lead respectively [8,9]. Thin platelets with extensive {0001} surfaces for

bismuth and {111} for lead were identified as those that show superheating [8,9]. An *in situ* reflection high-energy electron diffraction (RHEED) study of thermally evaporated Pb thin films on graphite revealed that some fraction of the films could be superheated by 4 ± 2 K to 12 ± 2 K above the bulk melting temperature [21]. Mètois and Heyraud were able to produce a large number of {111} faceted polyhedral Pb crystallite on graphite that superheated by 3 K [21]. Small particles of bismuth, with particle diameters from 20 nm to 150 nm, grown on carbon and on silicon monoxide showed 10 K superheating above the bulk melting temperature using electron microscopy [23]. In a time-resolved study of surface superheating using 100-200 ps laser pulses, superheating by ~120 K, ~90 K, and 73 ± 9 K for Pb(111), Bi(0001), and In(111) surfaces, respectively, were reported [24,25].

The nanocrystal shape and external surface morphology determine its melting and solidification behavior. Recrystallized nanocrystals can have shapes and external surface morphologies that differ from the as-deposited nanocrystals, and hence, the melting and solidification behaviors can differ between the two types [26,27]. Dark field electron microscopy was used to investigate the melting of bismuth crystallites in as-deposited and recrystallized bismuth films on a carbon substrate [8]. As-deposited films were found to have crystallites that are different in shape and in melting behavior from those recrystallized after melting. While a subset of the as-deposited crystallites, with elongated platelet shape, superheated by 7 K above the equilibrium bulk melting point, the recrystallized polyhedral hexagonal shaped nanocrystals in the as-deposited film showed melting point depression. Using the same technique to study the melting of lead nanocrystals, superheating by 2 K was found for extensively {111} faceted platelet-

shaped nanocrystals formed in the as-deposited films. Lead nanocrystals with other shapes melted below the bulk melting point [9]. Indeed, non-equilibrium faceted nanocrystals have greater specific surface energy than equilibrium faceted ones and hence melt first [28]. Nanocrystals bounded by external facets with minimum energy surfaces are able to superheat above the bulk equilibrium melting point. Using reflection high-energy electron diffraction, as-deposited lead films, grown on graphite at room temperature, showed superheating of up to 12 ± 2 K [21]. The observed superheating was attributed to the presence of two-dimensional (2D) {111}-oriented layers in the as-deposited film, while recrystallized films had the form of three-dimensional (3D) crystallites. When measuring the melting point and latent heat of fusion of 0.05-0.5 nm in radius tin particles using a nanocalorimetric technique, both were found to increase with the particle size. Also, the values obtained from the second heating cycle, recrystallized sample, were slightly higher than those obtained from the first heating cycle [15]. A change in the melting point upon recrystallization of embedded nanocrystals was also previously observed. An X-ray diffraction study of lead crystallites embedded in aluminum showed substantial superheating whose value depended on the heating cycle and on the inclusion size [29]. Due to annealing in previous heating cycles and possible coalescence, superheating found in the second cycle was lesser than that found in the first cycle.

The melting behavior of low-dimensional systems has been the subject of many theoretical studies based on thermodynamic models and numerical investigations based on molecular dynamics [7,30-32]. A thermodynamic model of the melting of nanoparticles in contact with a solid surface showed a melting point behavior that is

affected by the substrate surface and the contact angle between the adsorbate liquid and the substrate surface [33]. This model predicted a decrease in the nanoparticle melting temperature as the contact angle decreases; particles with contact angles more than 160° could be superheated. The size dependence of the melting point of thin films, embedded nanocrystals, or crystalline nanofibers was modeled based on the vibrational entropy of melting and Lindmann's melting criterion [31,34-36]. These models showed a decrease in the melting temperature with reduced size. In these models, superheating is only expected when the ratio between the average mean square displacement of the atoms at the surface and those within the bulk is less than one, a condition that happens only for embedded particles having coherent or semi-coherent interface with the surrounding matrix. A molecular-dynamics (MD) simulation using many-body type interaction potential showed that a confined cluster with coherent or semi coherent boundary conditions can be significantly superheated [32]. In another MD simulation, embedded tin clusters with 10-30 atoms per cluster remained solid at ~50 K above the bulk melting point [37]. Simulations of small gold particles of 100–900 atoms showed a sharp decrease in the melting temperature with the decrease in the cluster size [30].

This chapter demonstrates the experimental results and discussion of using RHEED to study the melting and solidification of as-deposited indium nanocrystals and nanocrystals recrystallized from melt. The nanocrystals were formed by evaporation on highly oriented (002) graphite. Indium nanocrystals were chosen because a nanocalorimetric study of its size dependent melting point depression was previously performed [5]. In addition, a recent study of ultrafast laser heating of In(111) has shown surface superheating [24]. The size, size distribution, and morphology were studied using

ex situ SEM or AFM. The effect of the nanocrystal shape and size on the melting behavior of indium nanocrystals is also discussed.

IV.2. Experimental Method

The experiment was performed in an ultrahigh vacuum system with base pressure $\sim 1 \times 10^{-10}$ Torr. An 8.5-kV electron gun is used to obtain the diffraction patterns. A 12x12x2-mm, (002) highly oriented pyrolytic graphite (HOPG) substrate is used. The interaction between the deposited indium and the graphite substrate is known to be of the Van der Waals type, with no chemical reaction or inter-diffusion of indium in the graphite [38,39]. An atomically clean surface of the HOPG substrate, hence clear RHEED pattern, can easily be obtained by simple cleavage. The graphite substrate is loaded in the ultrahigh vacuum chamber immediately after cleaving it in air. The substrate was mounted on a resistively heated stage capable of reaching temperatures up to 1000 K. A K-type thermocouple was used to measure the surface temperature of the substrate and the deposited film. The graphite substrate is cleaned by heating at ~ 770 K for 10 minutes, which is sufficient to obtain a clear graphite diffraction pattern. The thermocouple was calibrated to the bulk melting point of indium, the melting point of ice, and the boiling point of distilled water. This calibration was performed before the experiment and after several cycles of heating and cooling in vacuum. The accuracy of our temperature measurements is determined to be within ± 1 K near the bulk melting point of indium.

Indium is evaporated from a 99.999% pure indium wire using a heated tungsten basket. The substrate temperature is kept at ~ 423 K during deposition. To control the deposition process, a shutter is used to interrupt the indium vapor flux. The film mean

thickness is obtained by means of a quartz crystal thickness monitor, placed as close as possible to the substrate. The indium film mean thickness is also monitored from the decrease in the RHEED (00) spot intensity of the graphite substrate. A calibration curve of RHEED intensity versus mean film thickness enables accurate film thickness control. Indium thin films with different mean thickness, from 0.5 ML to 34 ML, are prepared. The spacing between each deposited ML is taken to be the indium-indium bond length, 3.25 Å. A deposition rate of 0.4 - 0.7 Å.s^{-1} is maintained by controlling the current applied to the heater filament. After deposition, the recrystallized films were heated to a temperature above the bulk melting point and slowly cooled down to a temperature below its supercooling temperature. The reappearance of the indium diffraction pattern during cooling indicates its recrystallization. The equilibrium polyherdal shaped indium nanocrystals were then formed for the recrystallized films, while the as-deposited nanocrystals grew in shapes that are dependent on the preparation conditions such as deposition rate and substrate temperature. The low indium vapor pressure near the bulk melting temperature, $< 10^{-11}$ Torr [40], allows for conducting the melting experiment with negligible atom loss by evaporation. Indium has a relatively low bulk melting point (430 K), which facilitates the melting experiment. Indium films are easily re-evaporated off the substrate at the end of the investigation, by holding the substrate at 873 K for few minutes. A clear graphite pattern is observed, which indicates complete evaporation of the deposited indium off the graphite.

A computer-controlled charged coupled device (CCD) camera is used to record the diffraction patterns that are displayed on a phosphorus screen. Melting and solidification of the grown indium nanocrystals were studied by monitoring the intensity

change of the (00) and (01) spots of the diffraction patterns as a function of temperature. The measurements were conducted by raising the sample temperature from room temperature to 450 K in ~10 minutes, and then the heating stage power is turned off letting the sample cool down to near room temperature in ~30 minutes. The RHEED patterns were recorded during heating and cooling. Each RHEED pattern is acquired in ~0.17 s, thus, temperature changes during the pattern acquisition are negligible. The thin film morphology was observed by *ex situ* SEM or AFM. The lateral and height resolutions of the AFM used are 1 nm and < 0.1 nm, respectively, as specified by the manufacturer. Our lateral resolution, however, is limited by the end-tip diameter, which was less than 10 nm.

IV.3. Results and discussion

IV.3.1. Substrate structure, and film deposition

After reaching the ultrahigh vacuum, the substrate is heated to ~ 770 K for 10 minutes to get rid of any possible adsorbed gases and obtain a clear RHEED pattern. The identification and analysis of the graphite RHEED pattern is illustrated in appendix A and B. The obtained RHEED pattern of the graphite was interpreted as an image of a three-dimensional reciprocal lattice parallel to the ⟨001⟩ direction.

As indium is deposited on the graphite substrate, the temporal change of the graphite (00) spot intensity is found to decay continuously with no intensity oscillation observed, as shown in Fig. 4.1(a). This is consistent with a 3-dimensional (3D) growth mode forming islands, as confirmed by *ex situ* SEM images. This is known to be the normal growth mode of indium thin films [5,16,17,19]. Relating the decay of the (00)

spot intensity to the film thickness, as measured by a quartz crystal thickness monitor, gives a calibration curve between the normalized (00) spot intensity and film mean thickness, as shown in Fig. 4.1(b). The decay of the (00) spot intensity with indium deposition is due to enhanced surface coverage with indium nanocrystals. Although the sticking coefficient of indium to the quartz crystal may differ from that of indium to the graphite substrate, this difference in sticking coefficient does not affect the results since the nanocrystals size distribution is measured by *ex situ* real imaging technique.
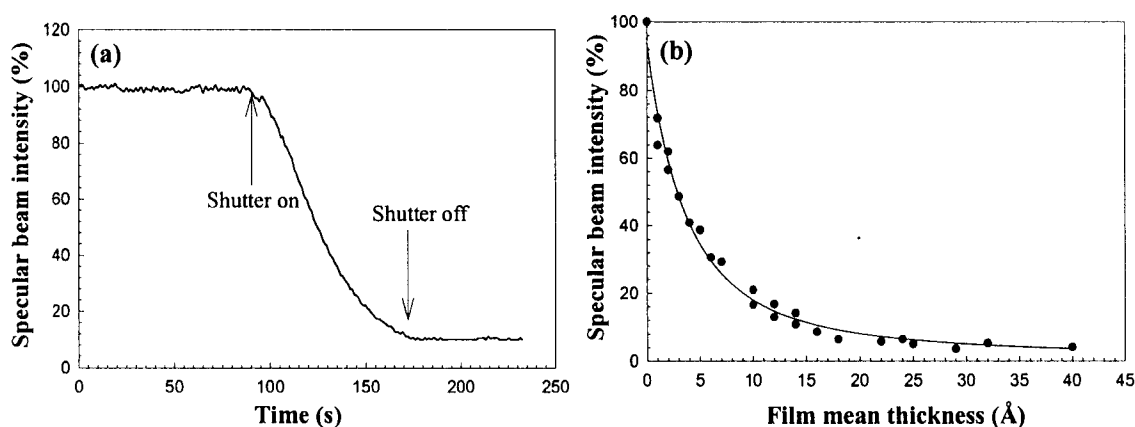
FIG. 4.1. The graphite specular peak intensity, (a) as a function of time during film deposition, (b) as a function of the indium film mean thickness as recorded by a crystal thickness monitor. The RHEED (00) beam intensity decays continuously with no oscillation indicating a 3D growth. Curve (b) enables mean film thickness control through the RHEED (00) intensity and is used for calibration.

IV.3.2. Structure and morphology of indium nanocrystals

IV.3.2.1. Nanocrystals recrystallized from melt

Figure 4.2 shows RHEED patterns of thermally evaporated indium films with different mean thickness after recrystallization from the melt. At low indium thickness, the $1.l$ and $\bar{1}.l$ graphite rods are still visible (indicated by arrows) due to low surface coverage. As the surface coverage increases, the surface area covered by nanocrystals

increases, resulting in an enhancement of the indium pattern on the expense of that of graphite. Indium gives a diffraction pattern that is characteristic of a transmission RHEED pattern. Increased 3D indium island-density with further indium deposition eventually causes the disappearance of the graphite pattern. Measuring the reciprocal basis vector from the rod spacing in the indium diffraction pattern, $a^* = 2\pi W/\lambda L$, where W is the rod separation and L is the sample-to-screen distance, a^* is found to be 2.07 Å^{-1} in good agreement with the calculated $a^*_{001} = 2.12$ Å^{-1}.
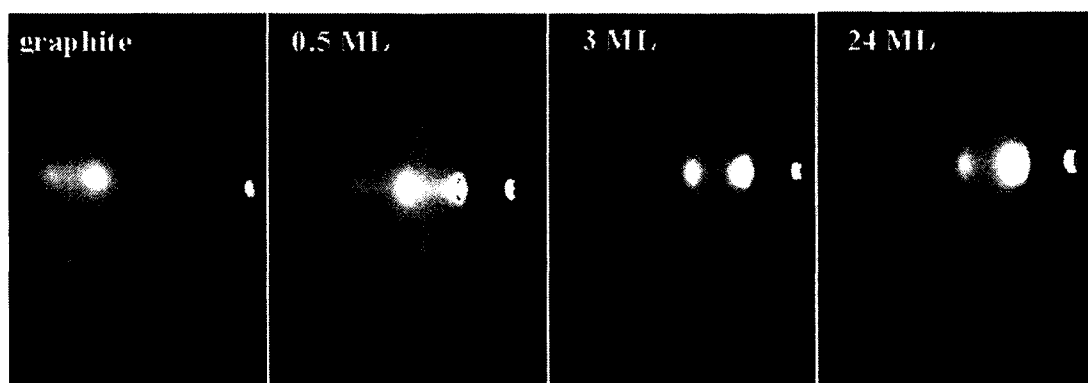
FIG. 4.2. Diffraction patterns of evaporated indium films with different thickness shown along with that for clean graphite (002) surface. The electron beam energy is 8.5 kV for both, while $\theta \approx 3.5°$ for graphite and 2.2° for indium. The $1.l$ and $\bar{1}.l$ graphite rods are visible (indicated by arrows) at low surface coverage and gradually disappear with increased indium thickness.

The morphology of indium films, performed at three different locations across the surface, was observed by SEM. Figure 4.3 shows SEM images of the 3-ML and 34-ML indium films at one location, on each film, at different magnification powers. Indium is found to grow from the melt as an ensemble of faceted nanocrystals. The nanocrystals has a cubo-octahedron shape with facets that are connected by curved surfaces with smooth edges similar to Pb, Sn, and In crystallites observed before [26,27,41,42]. The

equilibrium shape of indium crystallites on graphite has {111}, {001}, and {100} facets connected with smooth edges. The SEM images do not show any thin platelets similar to those observed when evaporating bismuth and lead without recrystallization from the melt [8,9,22]. The interaction between the deposited indium films and graphite substrate is known to be of the Van der Waals type with no chemical reaction or interdiffusion of indium in the graphite [39]. The crystallite size distribution was analyzed over an arbitrarily chosen 2.5 x 1.5 μm area. Figure 4.4 shows the crystallite size distribution for some indium films of different mean thickness at two different locations on each film. The size distribution, the number of counted particles, and the average crystalline size are found to depend on the location. Because terrace edges provide sites with lower adsorption energy and break the isotropy of surface diffusion, large numbers of indium nanocrystals with smaller sizes are found near the terrace edges. For the 3-ML and 6-ML films, Fig. 4.4(a) and Fig. 4.4(b), the morphology is strongly dependent on location. Near terrace edges, a significant increase in the density of nanocrystals and some decrease in the average crystalline size is observed. This strong morphology dependence on location is not observed for the thicker samples as show in Fig. 5(c) and Fig. 4.4(d). Although particle distribution analysis is sensitive to the chosen area in the SEM images, some general conclusion about their size distribution can be made. The slight decrease in the average crystallite size as the film mean thickness is increased from 3 ML to 6 ML is due to the increase in nucleation density as evident by the larger number of particles counted in the scanned area, particularly at locations with few terrace edges. As the average film thickness was increased from 6 ML to 43 ML, the average crystallite size grew and some coalesced resulting in a reduced total number of particles in the scanned area. The

average indium crystallite size and the graphite surface coverage increase with film mean thickness.
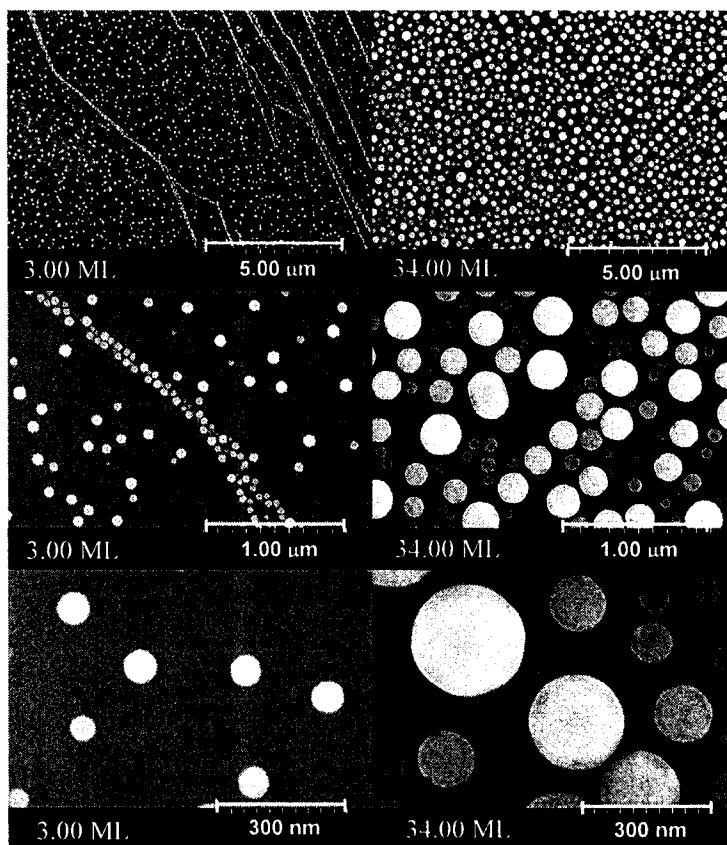
FIG. 4.3. SEM images of indium nanocrystals on graphite (002) of films with mean thickness 3 ML and 34 ML are shown with different magnification powers at one location on each film. Well-faceted indium nanocrystals are distributed over the graphite substrate surface. At terrace edges a large density of nanocrystals is observed. (a) 3 ML, (b) 34 ML.
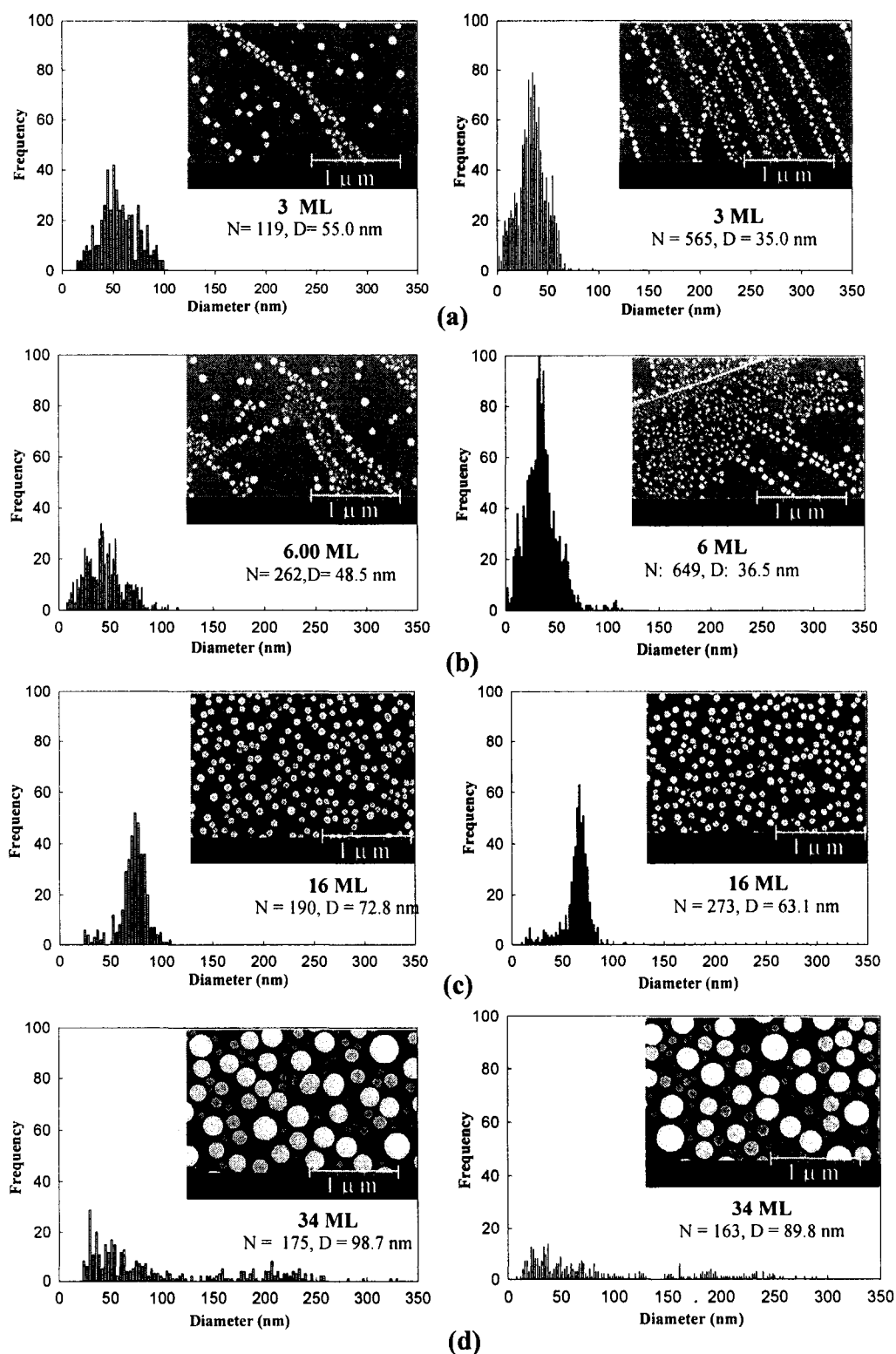
FIG. 4.4. The size distribution of indium nanocrystals calculated for films with different mean thickness, taken at two randomly selected locations on each film. The inset is the SEM image of a 2.5 x 1.5 μm area of the film for which the analysis is performed. (a) 3 ML, (b) 6 ML, (c) 16 ML, and (d) 34 ML. N is the total number of particles; D is the average particle size.

IV.3.2.2. As-deposited nanocrystals

Within the experimental uncertainty, no relative shift in position could be noticed in the RHEED spots between the as-deposited and recrystallized samples, indicating no change in the average unit cell. The pattern remains observable at all azimuth orientations, a feature that is characteristic of transmission patterns. As mentioned in the previous chapter, the transmission diffraction features observed in the RHEED pattern originate from a shell roughly the IMFP in thickness. Because of the penetration limit of the electron beam, the RHEED patterns show no dependence on shape and size of the nanocrystals for the studied films. The RHEED image results from all diffractions from crystallites forming the film within the probed area, and is affected by shadowing. This lead to poor shape and size sensitivity of RHEED for films with high coverage ratios and high height differences between its crystallites [43]. Fig. 4.5 shows the room temperature RHEED patterns of the as-deposited and recrystallized indium films with different mean thicknesses deposited at room temperature. Spots located on the circumference of Laue rings are observed for the as-deposited as well as recrystallized indium films. This observation is characteristic of a transmission-reflection pattern. However, for the as-deposited films, streak-like features are observed between the 00 and the 01 spots and through the $1n$ and $\overline{1}n$ spots, where n is the Laue ring order. The streak feature in the as-deposited films is due to a surface reflection component in the diffraction pattern, while the spot pattern is characteristic of transmission through clusters or surface roughness. The as-deposited 1.5-ML film does not show clear streaks; only diffraction spots indicating a dominant transmission feature through the 3D indium nanocrystals. As the film mean thickness increases, the surface diffraction component increases and reflection

streaks are clearly observed for the as-deposited 10-ML indium film. This indicates a nearly flat surface of the as-deposited nanocrystals, which is confirmed using *ex situ* AFM. Moreover, the RHEED streaks disappear and clear separate spots are observed when the films are recrystallized showing transmission-dominant diffraction patterns.
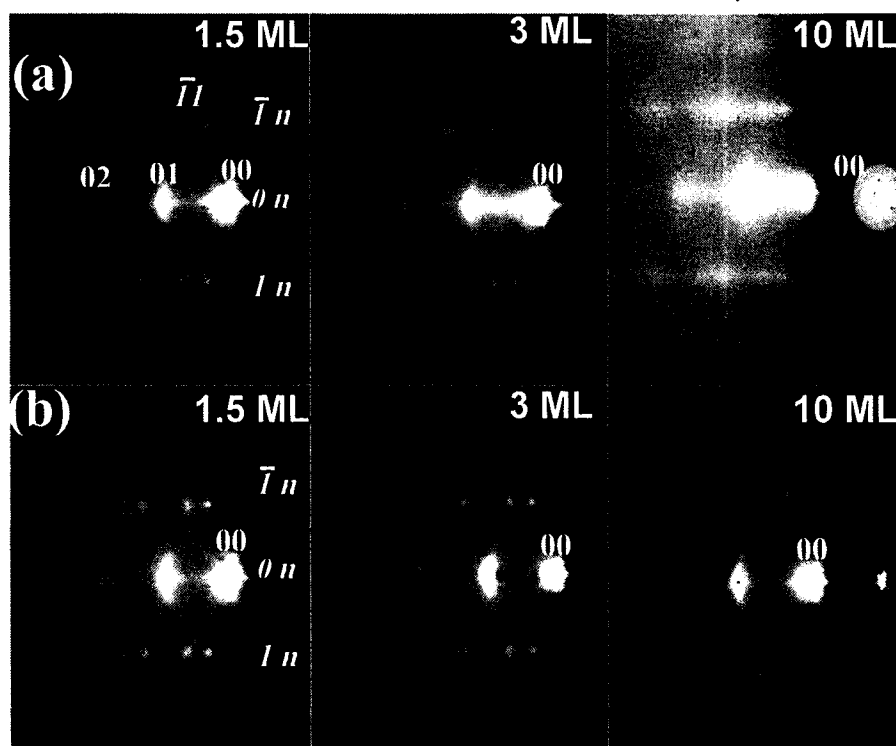
FIG. 4.5. RHEED patterns of (a) as-deposited, and (b) recrystallized indium films with different mean thicknesses deposited at room temperature.

The crystallographic shape and morphology of the as-deposited relative to those of recrystallized indium nanocrystals is studied using *ex situ* AFM. Images with different magnifications of an arbitrary selected area of the sample surfaces are obtained. Fig. 4.6 shows AFM images taken for as-deposited and recrystallized 1.5-ML and 10-ML indium films deposited at room temperature. Line profiles along the highest magnification

images are also presented. The nanocrystals are distributed uniformly throughout the substrate surface except at terrace edges where a higher density of nanocrystals is found. This is because, among all possible nucleation centers, terrace edges offer minimum energy barrier for nucleation. Shallow 3D nanocrystals with different shapes having a relatively flat top surface are found in the as-deposited films. However, the recrystallized nanocrystals are less faceted, with different sizes, and larger heights than the as-deposited ones. The as-deposited 1.5-ML showed nanocrystals of 10 - 20 nm height, while the recrystallized nanocrystals showed heights ~ 65 nm with nearly the same crystal width. This indicates an increase in the crystal size as the nanocrystals are recrystallized. A similar observation is found for the 10-ML film. Triangular shaped nanocrystals with sharp and curve edges, elongated platelet, and well-faceted polyhedral shape nanocrystals are clearly observed for as-deposited films. Less faceted nanocrystals forming polyhedron shapes with curved edges and curved top surfaces are observed in the recrystallized films. Rounded or curved surfaces indicate the presence of all surface orientations in the formed nanocrystals, however, sharp-edged shapes indicate missing orientations in the formed nanocrystals [44]. As reported previously in temperature dependent studies of equilibrium-shaped nanocrystals, the curved regions increase in size at the expense of the plain facets, due to the decrease in surface energy anisotropy with temperature, until a spherical shape is formed as the nanocrystal is completely melted [26,27,43]. Slow cooling or annealing conditions allow all possible surface orientations to appear in the final form of the nanocrystals; hence the curved surface areas in recrystallized nanocrystals are large.
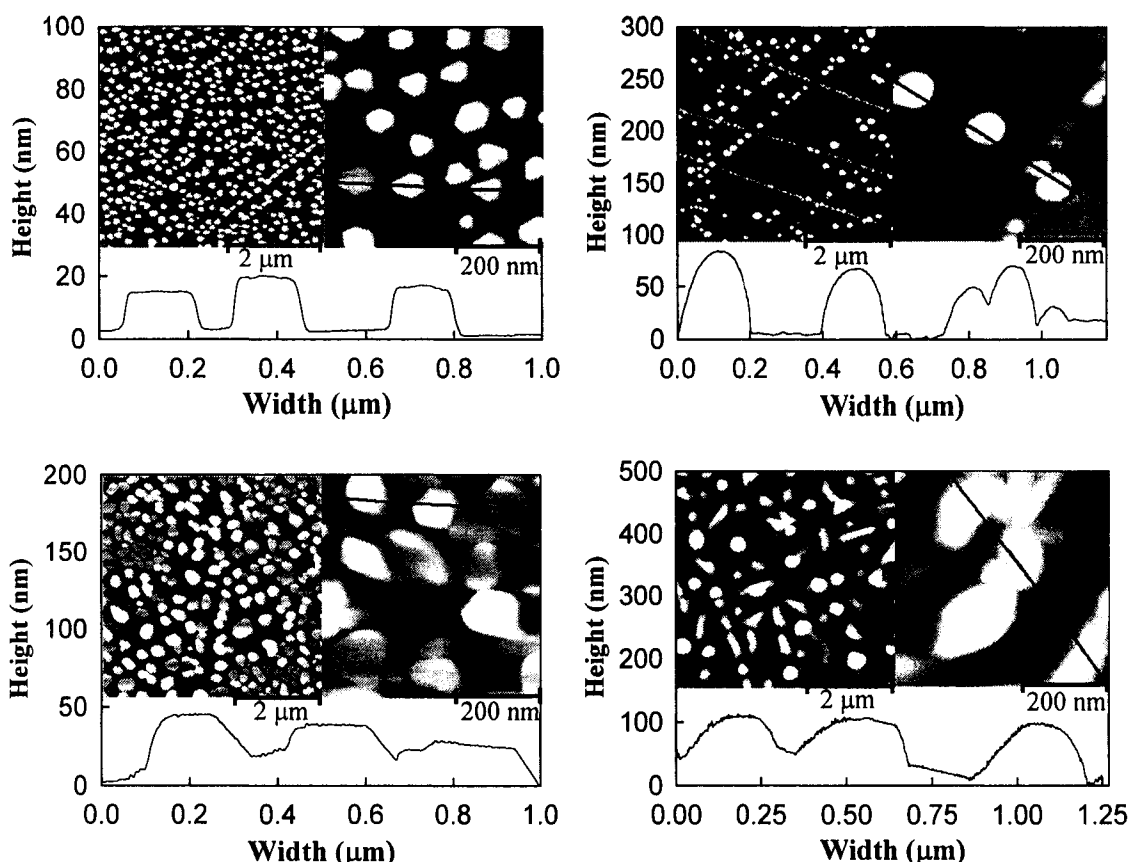
FIG. 4.6. AFM images of as-deposited and recrystallized 1.5-ML and 10 ML indium films deposited at room temperature along with line profiles. Shallow nanocrystals with relatively flat top surfaces are found in the as-deposited films, while the recrystallized nanocrystals form crystals with larger heights and curved surfaces.

The different non-equilibrium crystal shapes formed in the as-deposited films are determined by the size, the preparation condition, and the surface free energies involved in nanocrystal growth [44-46]. Small-size crystals form in the minimum total free energy-shapes, which are influenced by the preparation condition [44]. Moreover, the formation of crystal facets is due to the anisotropic surface energy and the surface free energy temperature and size dependence [45,46]. Because attaining an equilibrium shape is an energy-activated process, nanocrystals remain in the shape originally formed unless annealed at a higher temperature for a relatively long time or slowly recrystallized from

melt [46]. Fig. 4.7 gives the size distribution of as-deposited 3-ML and 10-ML films, deposited at room temperature for an arbitrary selected location on the surface of the films. Similar to nanocrystals recrystallized from melt, as-deposited indium nanocrystals showed a size distribution that is affected by the location selection for low thickness. The size distribution is shifted toward the larger values and spreads over a wider size range as the mean thickness increases. The average crystallite size also increases from 78 nm to 280 nm as the film mean thickness increases from 3 to 10 ML.
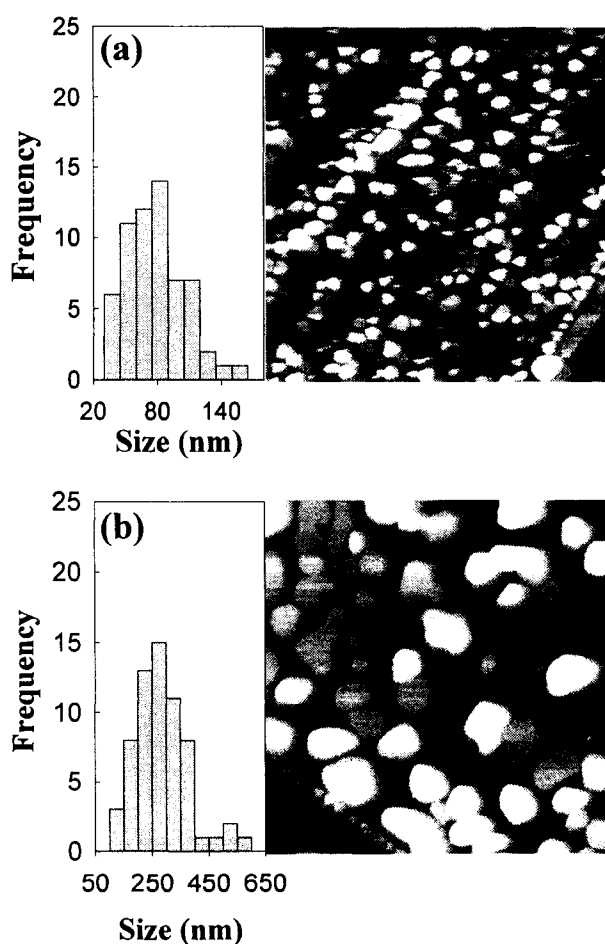
FIG. 4.7. AFM images and histograms of size distribution of as-deposited indium nanocrystals with different mean thicknesses (a) 3 ML and (b) 10 ML, deposited at room temperature. The distribution is shifted toward the higher value and spreads over a wider size range as the mean thickness is increased from 3 ML to 10 ML.

IV.3.3.   Melting and solidification of indium nanocrystals

IV.3.3.1.   Nanocrystal recrystallized from melt

Melting and solidification of the indium films were studied by measuring the intensity of the (00) and (01) spots with temperature. The heating and cooling rates during these measurements were maintained as described in the experimental section. No significant pressure changes in the vacuum chamber were observed during heating and cooling. Examples of these measurements are shown in Fig. 4.8. The diffraction intensity is normalized to its intensity at or near room temperature. The logarithm of the normalized (00) diffraction intensity is plotted as a function of temperature for heating and cooling. The deviation from the exponential Debye-Waller behavior with temperature indicates the initiation of film melting. This is followed by a sharper intensity decrease, corresponding to increased rate of nanocrystal melting. The end of this sharp intensity decrease indicates complete melting of the nanocrystal ensemble; only an inelastic diffraction background is present. In contrast to the abrupt nature of bulk melting, the melting of these indium films extends over a wide temperature range, which is attributed to the size distribution of the nanocrystals. The same observation was reported previously for melting of different nanocrystal thin films [5,15,18,19,47]. During cooling, the indium nanocrystals show supercooling relative to the onset of its melting. A film with 0.5 ML mean thickness shows 4 ± 2 K supercooling that increases to 8 ± 2 K and 12 ± 2 K as the mean thickness increases to 1.5 ML and 3.0 ML, respectively. Films with larger mean thickness show 16 ± 2 K supercooling, each relative to its own melting temperature. The observed supercooling is due to the presence of a nucleation barrier for solidification that
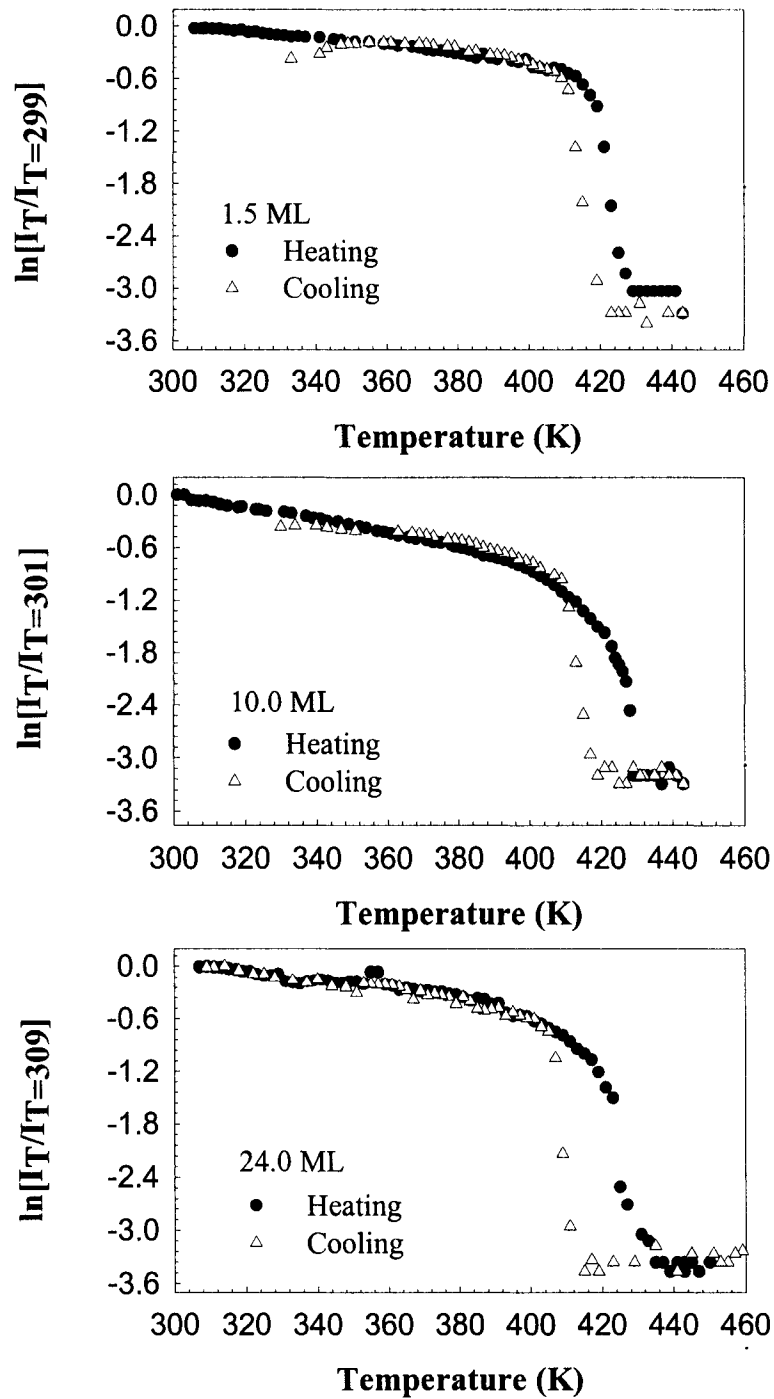
FIG. 4.8. Logarithm of normalized intensity of the RHEED (00) spot as a function of temperature during heating and cooling of indium films with different mean thickness. Smaller supercooling is observed for 1.5 ML than for 10 and 24 ML.

results from the competition between the decrease in the volume free energy upon solidification and the increase in the free energy associated with the existence of a solid-liquid interface. The size dependence of supercooling is attributed to the variation of the surface energy of the melt, and the liquid-substrate interfacial energy with the size of the droplet [39]. The smaller the droplet size, the smaller its melt surface energy and liquid-substrate interfacial energy. Thus, the energy barrier for solidification and the amount of supercooling are reduced as the droplet size is reduced [39].

The range of temperature over which the melting phase transition occurs is used to study the melting behavior of the ensemble of nanocrystals making up the indium thin film. If we assume that the intensity decrease of electron diffraction into the (00) and (01) orders is related to the fraction of the solid nanocrystals that are melted within the probed shell, we can use data as in Fig. 4.8 to estimate the melted ratio. For electron energy of 8.5 kV, the inelastic mean free path (IMFP) is 6 nm as calculated from the general equation of IMFP for indium [48]. Thus, the transmission diffraction features observed in the RHEED pattern originate from a shell roughly the IMFP in thickness. This thickness is larger than the critical liquid layer thickness of 2 nm for indium. The 2-nm critical liquid thickness of indium was estimated by Dippel *et al.* [16] based on the size dependent melting equation (Eq. (1) in Ref. [16]) using data for indium. After the liquid shell thickness reaches this critical thickness, the liquid diverges through the solid crystal [16]. Results of the estimated film-melted ratio as a function of temperature are shown in Fig.4.9. In calculating the melted ratio within the probed shell, the intensity decrease of the (00) order due to thermal vibration (Debye-Waller effect) is subtracted from the reduction in the diffraction intensity. This difference gives the diffraction intensity

reduction due to melting after taking the background into consideration. To account for the inelastic background that is superimposed on the (00) and (01) orders, we made a straight-line fit of the diffraction intensity at the high temperature tail of the melting curves, i.e. after complete melting, and subtracted that fit from the intensity of the (00) order.
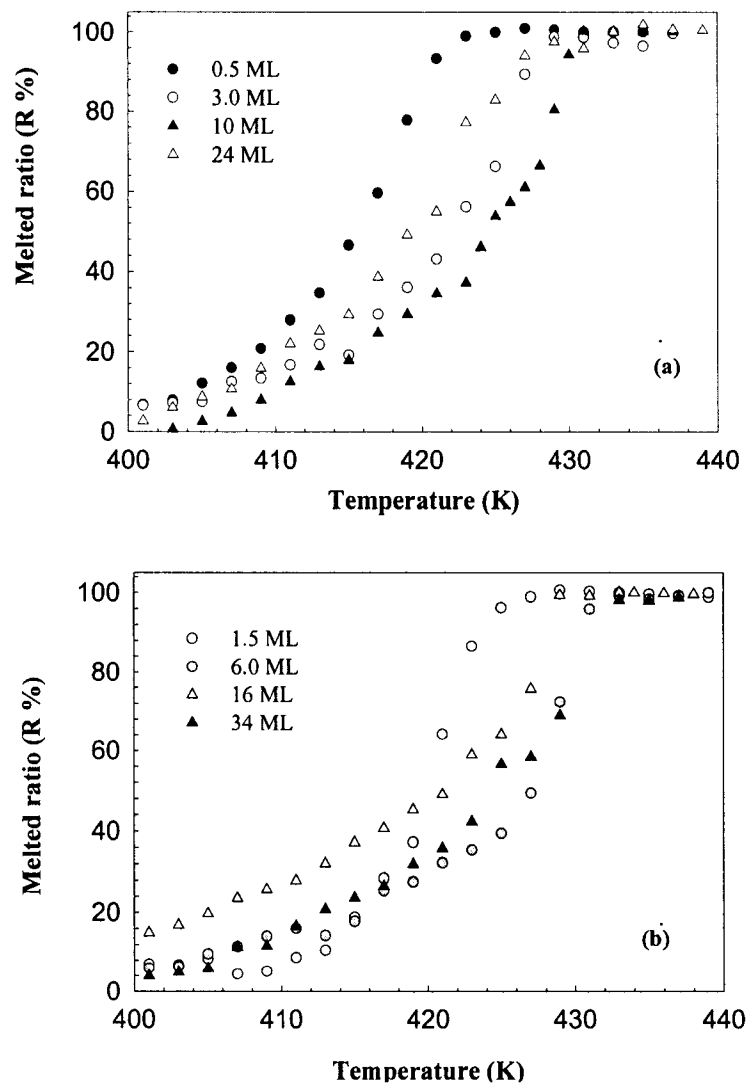
FIG. 4.9. Estimated film melted ratio as a function of temperature at the phase transition region for indium films with different mean thickness.

The diffuse inelastic background in RHEED arises due several effects that include phonon scattering (thermal diffuse scattering) and disorder in the probed region [49,50]. Theoretically, melting results in an increased diffuse background. The background intensity distribution in the RHEED pattern is complicated by dynamic (multiple scattering) effects. The background at a location between the (00) and (01) orders, in the studied temperature range, had a small value; typically ~10% or less of the peak intensity of the (00) order for temperatures up to the onset of melting. At this location, slight decrease in the background intensity with temperature was observed in our experiment. This observation cannot be explained by simple kinematic analysis and is, thus, assumed to be an effect of multiple scattering. Given that melting should increase the background intensity, we conclude that this expected increase is small compared to temperature dependent dynamic effects.

All films start melting at temperatures below the bulk melting temperature, *e.g.*, 25 K below bulk melting for the 0.5-ML film. The melted ratio for the 0.5-ML film changes rapidly with temperature and the film melts completely below the bulk melting temperature. For films with larger mean thickness, the melted ratio increases with temperature at slower rates. The size distribution and the shape of nanocrystals are expected to play a major role in this melting behavior [5,8,9,20]. Nanocrystals in the lower part of the size distribution are expected to melt at a lower temperature than those in the higher part, for crystallites with similar shape.

In general, the profile of the diffraction spots is related to the shape and size of the diffracting feature. Broadening of diffraction spots, after subtracting the instrumental response, is inversely proportional to the average crystalline size in the probed region.

The probed region in this case is the shell surrounding each probed nanocrystal with ~ 6 nm thickness. The instrumental response was obtained by deflecting the electron beam away from the sample so that it directly hits the phosphor screen. The shape of the electron beam, on the phosphor screen, was recorded by the CCD camera. The FWHM of this transmitted beam in Å^{-1}, was used as the instrumental response and was subtracting from the FWHM of the diffraction (00) spot, obtained at different mean film thickness. From the broadening of the (00) spot, diffraction feature size of ~ 4-7 nm is obtained, which is much less than the average nanocrystal size obtained by SEM. This is expected from a transmission RHEED pattern probing the outer shell of the nanocrystals. In Fig. 4.10, the full width at half maximum (FWHM) of the (00) spot parallel and normal to the sample surface is shown as a function of temperature. The FWHM remains constant over a wide temperature range and starts to increase only near the bulk melting temperature. The observed increase in FWHM of the (00) spot near the bulk melting temperature indicates that there is a reduction in the crystalline volume within the probed shell. The observed increase in the FWHM is consistent with the formation of a liquid skin covering the nanocrystals, thus, reducing the crystalline volume in the probed shell. The thickness of that liquid skin increases with temperature, and as it reaches a critical value of ~ 2 nm, the liquid diverges throughout the solid. Because the solid-liquid interfacial area is larger for larger crystals, small crystals melt first. Furthermore, the increase in the FWHM observed in Fig. 4.10 near T_m, is inconsistent with the view that the reduction in the diffraction pattern near T_m is due to homogeneous melting of the small crystallites that the electrons are probing without the formation of a liquid shell. Had this been the case,

the FWHM would have been reduced because of the increase in the average crystallite size as the smaller ones melt at lower temperatures.
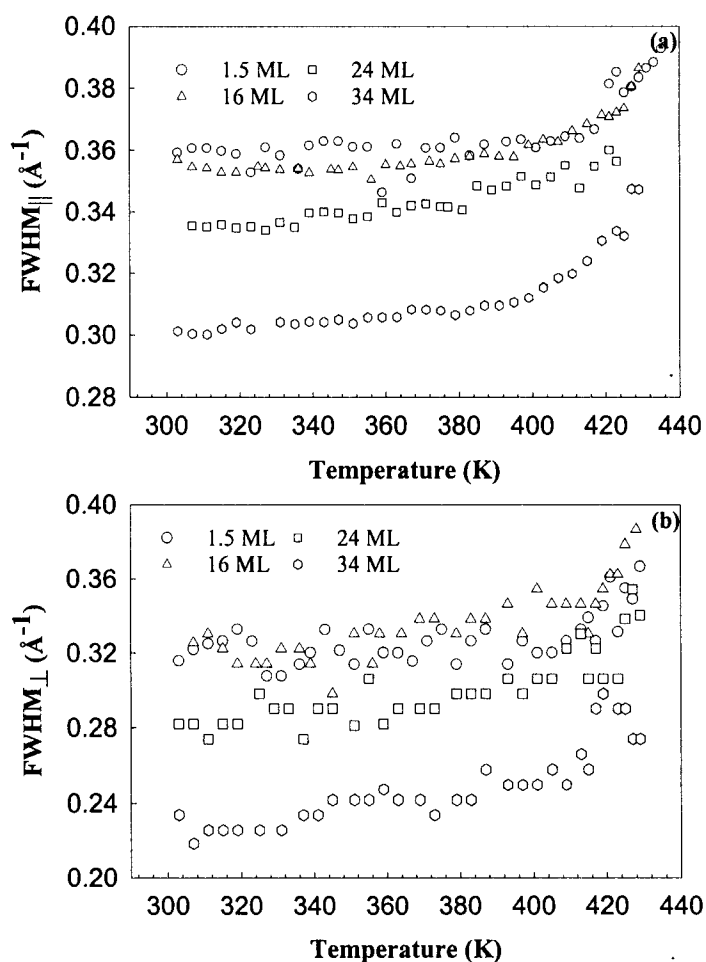
FIG. 4.10. The FWHM of the RHEED (00) spot from indium films with different mean thickness as a function of temperature in a direction (a) parallel and (b) perpendicular to the substrate surface. The plotted values include the instrumental response, which is the FWHM of the e-beam without scattering in the sample, and is measured to be ~ 0.19 Å⁻¹, for (a), and 0.15 Å⁻¹ for (b).

IV.3.3.2. Melting point-size dependent models

In order to obtain the rate of film melting with temperature, a curve-fit is made to the melted ratio data in Fig. 4.10 and the derivative of this curve-fit is plotted in Fig. 4.11.

The peak of this derivative gives the temperature at which the rate of film melting with temperature is the fastest, T_{fm}. We use T_{fm} to represent the characteristic film melting temperature, with a range that we define to correspond to 10% and 90% of the melted ratio in Fig. 4.10. Melting point depression that depends on the film mean thickness is clearly observed in Fig. 4.12.
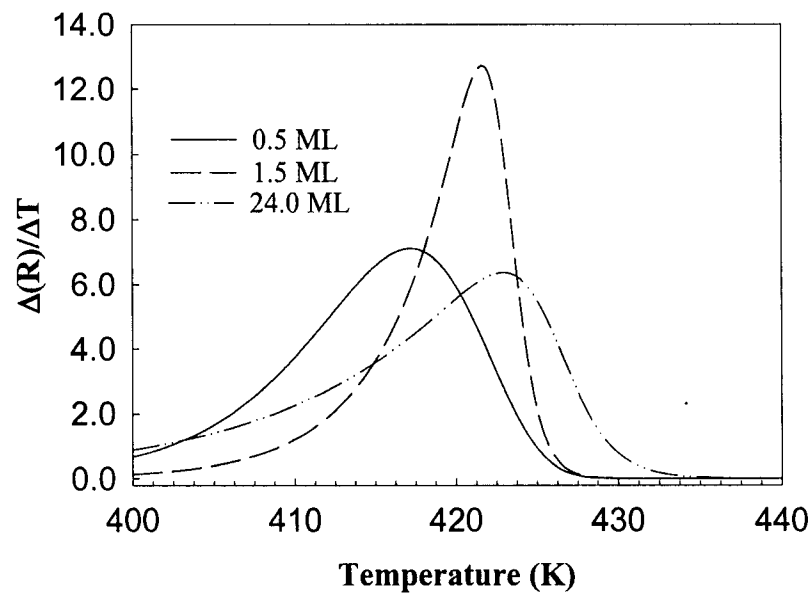
FIG. 4.11. Derivative of the curve-fit to the melted ratio curve in Fig. 4.9 obtained as a function of temperature for indium films with various mean thickness. The peak of this derivative gives the temperature at which the rate of film melting with temperature is the fastest, T_{fm}.

The characteristic film melting temperature is compared with the different melting point-size dependent models. The melting point of an indium nanocrystal as a function of its size is calculated based on melting models discussed in section 2.2.3. The known physical constants of indium ($T_0 = 430$ K, $\rho_s = 7.31$ g/cm^3, $\rho_l = 7.02$ g/cm^3, $L = 28.39$ J/g,
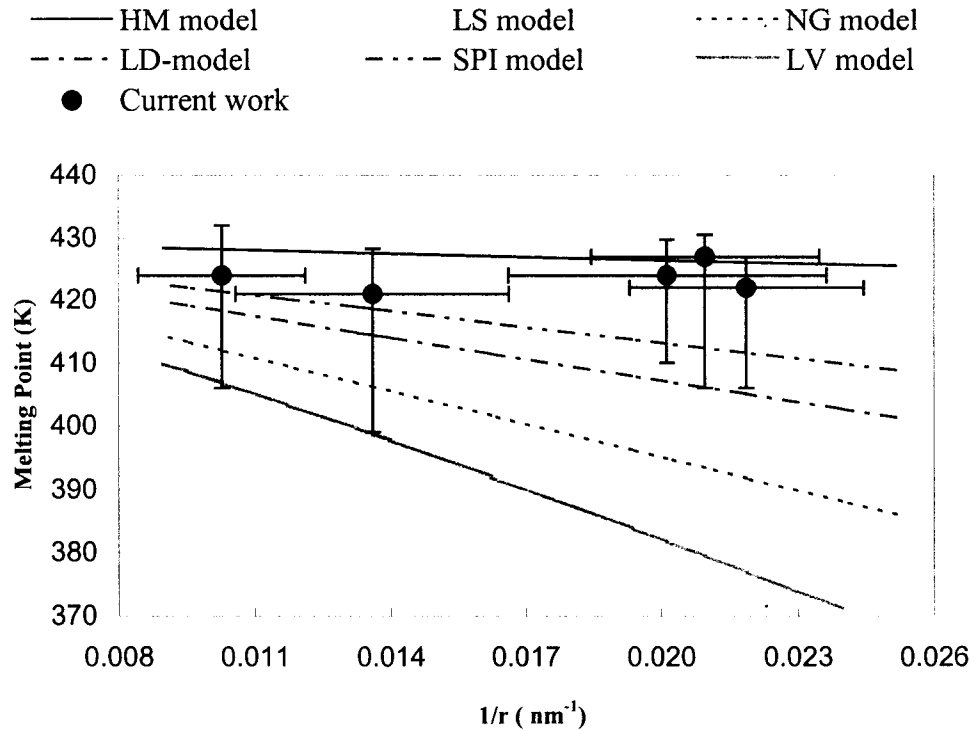
FIG. 4.12. The measured melting point as a function of the reciprocal of the average crystalline size compared to different thermodynamic models. The film melting point T_{fm} is obtained from Fig. 11. The horizontal bars represent the melting range as described in the text and the vertical bars represent the statistical error in the measured crystal size = ($\Delta r /r^2$). The liquid skin and homogenous models agree best with this experimental result.

γ_{sl} = 63 mJ/m^2, γ_{sv} = 618 ± 10 mJ/m^2, γ_{lv} = 560 mJ/m^2, h = 0.37 nm, $S(\infty)$ = 7.62 J/ mole

K, δ = 2 nm) are used in the calculations [5,16,34]. The melting point obtained from Eq.

(1) and Eq. (2) for indium particles of size larger than the skin thickness are nearly the

same. The nucleation and growth model, Eq. (4), is applicable only when surface effects

are eliminated, e.g., by confining the crystal with a higher melting point material forming

a coherent or semicoherent interface. In this case the crystal can be superheated. The

measured melting points as a function of the reciprocal of the average crystalline size

compared to the calculated values are shown in Fig. 4.12. The bars shown in Fig. 4.12

represent the range of temperature at which melting is observed in the ensemble of

nanocrystals because of their size distribution. The measured characteristic film melting temperature T_{fm} obtained from Fig. 4.11 shows agreement with the liquid skin model and the homogenous model. Because of the observed reduction in the crystalline volume in the probed shell observed in Fig. 4.10, our results favor the liquid skin model.

IV.3.3.3. Melting of as-deposited and recrystallized nanocrystals

Figure 4.13 shows the (00) spot intensity, normalized to its value at or near room temperature, measured as a function of temperature for as-deposited and recrystallized 3-ML indium film for a typical heating and cooling cycle. A decrease in the spot intensity with temperature is expected due to the enhanced atomic mean-vibrational amplitude as described by the Debye-Waller effect [21,28]. However, a sharp drop in the RHEED intensity occurs as the nanocrystals lose long-range order within the shell probed by the electron beam. Due to annealing of indium crystallites during heating, the normalized intensity of the (00) spot of the as-deposited film increases with temperature before its rapid decrease due to melting. A similar observation was reported during a melting and solidification study of Pb nanocrystals using X-ray diffraction where an increase in the integrated intensity of the (111) and (200) diffraction peaks were detected as the nanocrystals were heated toward melting [20]. Nanocrystals recrystallized from melt do not show any intensity increase before melting. Only the standard decrease due to increased lattice vibrations upon heating and crystal melting afterwards is observed. During cooling, both as-deposited and recrystallized nanocrystals showed a few degrees supercooling relative to their melting curves. While the normalized RHEED intensity of the recrystallized indium films recovers by solidification to its original value that of as-deposited nanocrystals exceeds its original value causing the saturation of the detector.
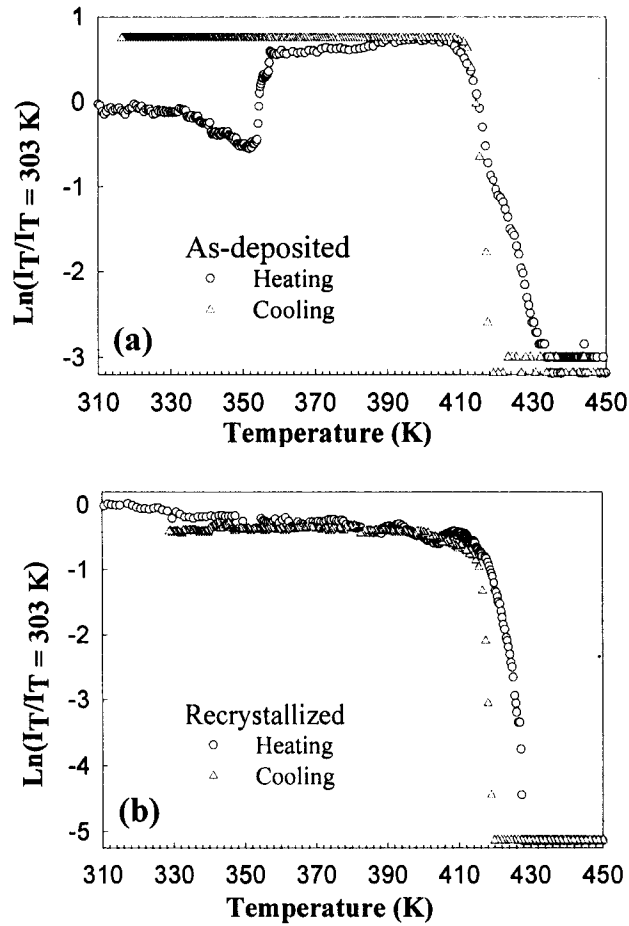
FIG. 4.13. Log of the normalized RHEED (00) spot intensity as a function of temperature during a heating and cooling cycle of (a) as-deposited and (b) recrystallized 3-ML indium film. The film was deposited at room temperature.

This behavior, observed in the as-deposited nanocrystals, is mainly due to the crystalline annealing and coalescence. Coalescence of metallic nanocrystals in the solid phase before melting is common, however, the coalescence mechanism depends on the annealing temperature [51]. Therefore, as the nanocrystals are heated up, the crystal shapes are changed to the more rounded polyhedral shape in addition to becoming larger due to coalescence. Thus, annealing enhances the measured RHEED intensity. On the other hand, recrystallized indium nanocrystals are already in their equilibrium shape and size;

hence no significant change in the normalized intensity is detected after solidification. Also, the amount of supercooling observed for as-deposited nanocrystals is found to be larger than that for recrystallized films, for films deposited at room temperature. This is attributed to the larger average crystal size for recrystallized films, which enhances the heterogeneous solidification and suppresses supercooling.

Figure 4.14 shows the normalized RHEED intensity of as-deposited and recrystallized indium films of different mean thicknesses as a function of temperature. An intensity increase due to annealing of as-deposited films is observed for the 1.5-ML film and is even stronger for the 3-ML film; however, is almost undetected for the 10-ML film. Because of the low coverage for the 1.5-ML film, we expect that the nanocrystals melt and solidify without significant coalescence, except in areas with higher coverage such as near terrace steps. Therefore, the observed intensity increase is mainly due to crystal shape modification with small contribution due to size increase by coalescence. As the mean thickness is increased, the coverage ratio increases and the crystallites become closer to each other causing their coalescence during heating. With further mean thickness increase, the crystal size increases by coalescence during growth, as observed from the AFM images of the as-deposited films. Although further coalescence and shape modification due to heating is possible, no increase in the RHEED intensity of the 10-ML film is detected. This could be due to the fact that RHEED detects only a shell determined by its IMFP within the nanocrystals. No intensity increase with heating before melting is detected for recrystallized films within the investigated thickness range.

The rapid decrease in the normalized (00) spot intensity with temperature indicates a decrease in the long-range order in the probed volume within the penetrated

shell of the nanocrystals [28,38]. As the film is completely melted, only the inelastic diffraction background is left. As-deposited and recrystallized nanocrystals showed melting behavior that extends over a temperature range. Based on different phenomenological models [6,7], small nanocrystals melt at a lower temperature. The temperature range over which as-deposited and recrystallized indium nanocrystals melt is due to the size distribution of these nanocrystals. A similar observation was previously reported for melting of different nanocrystal thin films [5-7,16,29,38].

We use RHEED to detect the diffraction pattern obtained from the ensemble of nanocrystals. We emphasize the measurement of the end melting point because it indicates the highest melting temperature of a subset of that ensemble. This is of interest because a fraction of the formed nanocrystals was previously shown to superheat above the equilibrium melting point [21]. As-deposited and recrystallized indium films melt completely before or at the bulk melting point, 430 K. Within the experimental error, as-deposited films, grown at room temperature, show an end melting point nearly equal to that of the recrystallized films except for the 1.5-ML film. The as-deposited 1.5-ML film shows an end melting point ~10 K lower than the recrystallized film. This could be due to average size increase resulting from coalescence as the film is recrystallized.

The dependence of the end melting point on the crystal size for as-deposited indium films, observed in Fig. 4.14, clearly suggests that not only the size but also the crystal shape determines the melting behavior of the nanocrystals. While the 3-ML film has an average crystallite size ~ 200 nm less than that of the 10-ML film, the end melting point of the 3-ML film is higher than that for the 10-ML film. This observation confirms
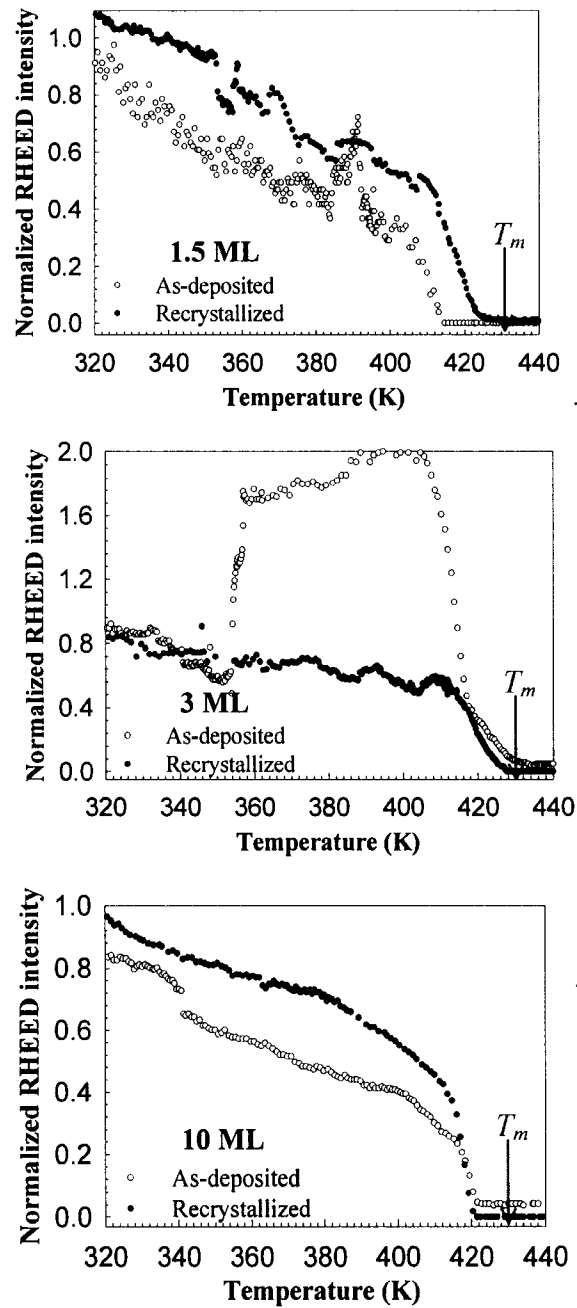
FIG. 4.14. Intensity of the RHEED (00) spot, normalized to that at 303 K, as a function of temperature during heating of as-deposited and recrystallized indium films of different thicknesses deposited at room temperature. The arrow indicates the bulk melting point of indium.

the effect of the external surface orientation on the melting of nanocrystals. Homogenous melting from within of these nanocrystals is energy costly; therefore the most plausible scenario is that melting must start at the surface [52,53]. Because the surface free energy depends on surface orientation, the melting behavior of same size nanocrystals is determined mainly by the external surface orientation and morphology. AFM images of as-deposited films, Fig. 4.7 and Fig. 4.8, show nanocrystals with different external facets and shapes including triangular shaped nanocrystals with sharp edges and elongated platelet. Lead and bismuth with similar crystal shapes were reported to show few degrees superheating above the bulk melting point [8,9,22]. Crystals with other shapes showed melting point depression. Indium has a non-isotropic surface energy with {111} surfaces having the lowest energy [27]. Therefore, one could subdivide the nanocrystals according to the external shape energy surfaces, and hence the melting behavior into those with low and high external energy facets. The low external energy faceted crystals show maximum stability and higher surface melting nucleation barrier as in case of the extensive {111} faceted platelet shaped crystals [9]. The high external energy shaped crystals favor surface melting formation, and hence show melting point depression. AFM images of the 3-ML film show the presence of low external energy faceted nanocrystals with a large number, and hence a high-end melting point is observed in spite of its low average size. On the other hand, coalescence during growth of the 10-ML film results in large crystallites with high external energy shaped, less faceted and more rounded nanocrystals, and hence a low-end melting point is observed.

IV.3.3.4. Deposition temperature effect on the melting behavior of indium nanocrystals

The effect of the substrate temperature during deposition on the melting behavior of as-deposited and recrystallized indium films is studied. Fig. 4.15 shows the variation of the normalized (00) RHEED intensity with temperature of indium films with different mean thicknesses deposited at different temperatures. The deposition temperature is found to affect the melting behavior and the end melting point of the as-deposited nanocrystals, as shown in Fig. 4.15(a-c). This effect depends on film mean thickness. For the 1.5-ML film, the end melting point increases as the deposition temperature increases, while films with a higher mean thickness show a decrease in the end melting point as the deposition temperature is increased. The end melting point of the 1.5-ML film increased by ~12 K as the deposition temperature increased from 348 K to 398 K. On the other hand, the 10-ML film deposited at 398 K shows an end melting point ~ 5 K lower than that deposited at either 348 K or at room temperature. High deposition temperature enhances the crystallinity of the grown film and hence increases the average crystal size. It also increases the kinetic energy, mobility, and self-diffusion of the deposited ad-atoms, which in turn enhances the formation of curved facets or more rounded nanocrystals. Therefore, the effect of the deposition temperature on the end melting point of as-deposited films results from the modification of nanocrystal shape and size during growth. While the size increase results in an increase in the end melting point, transformation of triangular and platelet shaped nanocrystals into a polyhedral shape decrease the melting point [8,9]. Therefore, the observed increase in the end melting point with the deposition temperature for the 1.5-ML film can be attributed to the

increase in the crystal size. Considering the limited penetration of the 8.5 kV RHEED electrons, the observed decrease in the end melting point with the deposition temperature for films with higher mean thickness could be attributed to nanocrystal shape changes. The deposition temperature shows almost no effect on the end melting point of the recrystallized indium nanocrystals. Fig. 15(d) shows the normalized RHEED intensity of recrystallized 3-ML indium film prepared at different deposition temperatures. This behavior is expected since once the nanocrystals are melted then recrystallized, their shape, size, and size distribution remains about the same after subsequent recrystallizations.
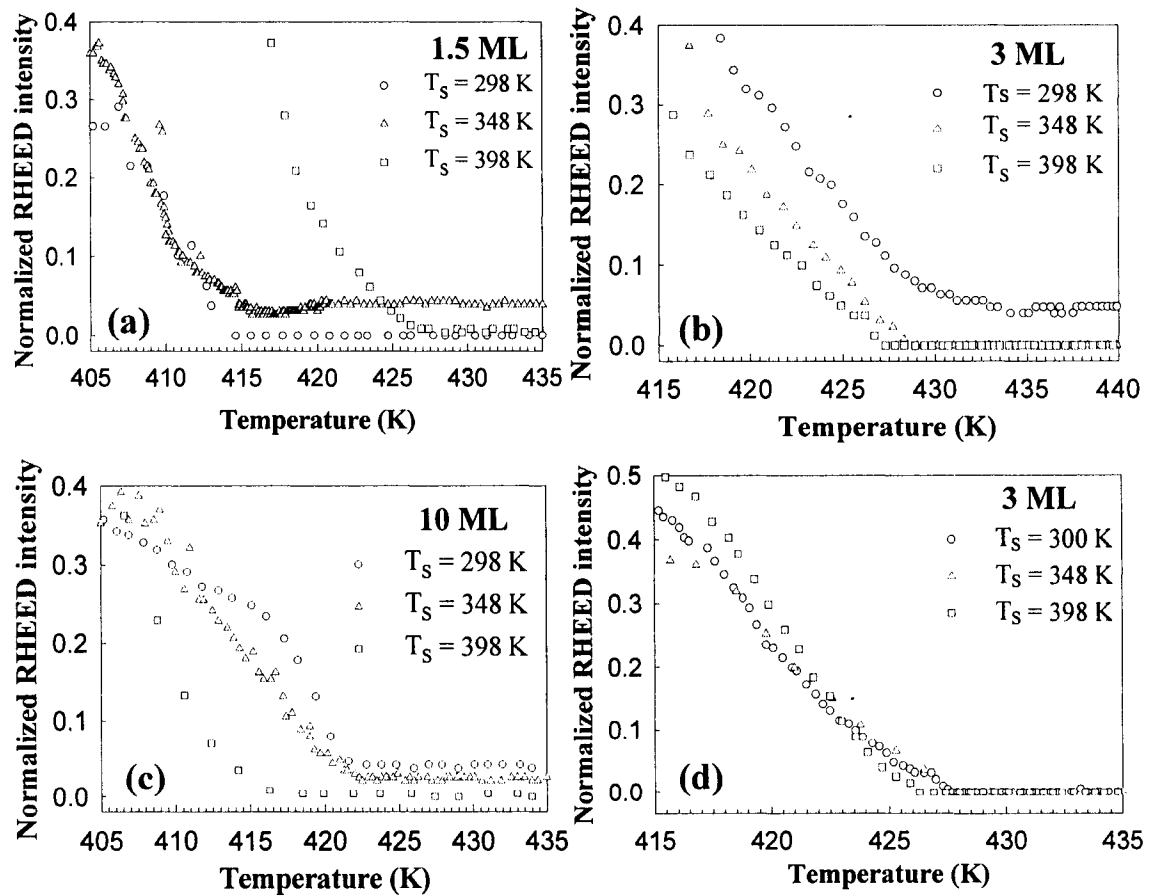
FIG. 4.15. The effect of the deposition temperature on the end melting point of indium films: (a-c) as-deposited films with different mean thicknesses; (d) recrystallized 3-ML film. The RHEED (00) intensity was normalized to that at 303 K.

IV.4. References of chapter IV

[1]   G. A. Breaux, R. C. Benirschke, T. Sugai, B. S. Kinnear, and M. F. Jarrold, "Hot and solid gallium clusters: too small to melt," Phys. Rev. Lett. **91**, 215508:1-4 (2003).

[2]   M. L. Lavčević and Z. Ogorelec, "Melting and solidification of Sn-clusters," Matter. Lett. **57**, 4134-3139 (2003).

[3]   S. Chacko, K. Joshi, D. G. Kanhere, and S. A. Blundell, "Why do gallium clusters have a higher melting point than the Bulk?," Phys Rev. Lett. **92**, 135506:1-4 (2004).

[4]   R. Kusche, T. Hippler, M. Schmidt, B. von Issendor, and H. Haberland, "Melting of free sodium clusters," Eur. Phys. J. D **9**, 1-4 (1999).

[5]   M. Zhang, M. Yu. Efremov, F. Schiettekatte, E. A. Olson, A. T. Kwan, S. L. Lai, T. Wisleder, J. E. Greene, and L. H. Allen, "Size-dependent melting point depression of nanostructures: nanocalorimetric measurements," Phys. Rev. B **62**, 10548-10557 (2000).

[6]   T. Castro, R. Reifenberger, E. Choi, and R. P. Andres, "Size-dependent melting temperature of individual nanometer-sized metallic clusters," Phys. Rev. B **42**, 8548-8556 (1990).

[7]   Ph. Buffat and J. Borel, "Size effect on the melting temperature of gold particles," Phys. Rev. A **13**, 2287-2298 (1976).

[8]   S. J. Peppiatt, "The melting of small particles. II. bismuth," Proc. R. Soc. Lond. A **345**, 401-412 (1975).

[9]   G. D. T. Spiller, "Time-dependent melting and superheating of lead crystallites," Phil. Mag. A **46**, 535-549 (1982).

[10]   H. W. Sheng, K. Lu, and E. Ma, "Melting and freezing behavior of embedded nanoparticles in ball-milled Al-10wt%M (M= In, Sn, Bi, Cd, Pb) mixitures," Acta Mater. **46**, 5195-5205 (1998).

[11]   B. Kusz, K. Trzebiatowski, M. Gazda, and L. Murawski, "Structural studies and melting of bismuth nanocrystals in reduced bismuth germanate and bismuth silicate glasses," J. Non-Cryst. Sol. **328**, 137-145 (2003).

[12]   H. W. Sheng, G. Ren, L. M. Peng, Z. Q. Hu, and K. Lu," Superheating and melting-point depression of Pb nanoparticles embedded in Al matrices," Phil. Mag. Lett. **73**, 179-186 (1996).

[13]   J. Zhong, L. H. Zhang, Z. H. Jin, M. L. Sui, and K. Lu, "Superheating of Ag nanoparticles embedded in Ni matrix," Acta Mater. **49**, 2897-2904 (2001).

[14]   J. Zhong, J. Xu, L. G. Yu, X. K. Sun, Z. Q. Hu, and K. Lu, "Melting process of nanometer-sized In particles embedded in an Al matrix synthesized by ball milling," J. Mater. Res. **11**, 28941-2851 (1996).

[15]   S. L. Lai, J. Y. Guo, V. Petrova, G. Ramanath, and L. H. Allen, "Size-dependent melting properties of small tin particles: nanocalorimetric measurements," Phys. Rev. Lett. **77**, 99-102 (1996).

[16]   M. Dippel, A. Maier, V. Gimple, H. Wider, W. E. Evenson, R. L. Rasera, and G. Schatz, "Size-dependent melting of self-assembled indium nanostructures," Phys. Rev. Lett. **87**, 095505:1-4 (2001).

[17] G. Krausch, T. Detzel, H. N. Bielefeled, R. Fink, B. Luckscheiter, R. Platzer, U. Wöhormann, and G. Schatz, "Growth and melting behavior of thin in films on Ge(100)," Appl. Phys. A **53**, 324 (1991).

[18] T. Tsuboi, Y. Seguchi, and T. Suzuki, "The melting temperature of thin lead films," J. Phys. Soc. Jpn. **59**, 1314-1321 (1990).

[19] J. F. Pócza, A. Barna, and P. B. Barna, "Formation processes of vacuum-deposited indium films and thermodynamical properties of submicroscopic particles observed by *in situ* electron microscopy," J. Vac. Sci. Technol. **6**, 472-475 (1969).

[20] K. F. Peters, J. B. Cohen, and Y. Chung, "Melting of Pb nanocrystals," Phys. Rev. B **57**, 13430-13438 (1998).

[21] Z. H. Zhang, P. Kulatunga, and H. E. Elsayed-Ali, "Reflection high-energy electron-diffraction study of melting and solidification of Pb on graphite," Phys. Rev. B **56**, 4141-4148 (1997).

[22] J. J. Mètois, and J.C. Heyraud, "The overheating of lead crystals," J. Phys. (France) **50**, 3175-3179 (1989).

[23] M. Blackman, S. J. Peppiatt, and J.R. Samples, " Superheating of bismuth," Nat. Phys. Sci. **239**, 61-62 (1972).

[24] B. Lin and H. Elsayed-Ali, "Temperature dependent reflection electron diffraction study of In(111) and observation of laser induced transient superheating," Surf. Sci. **498**, 275-284 (2002).

[25] J. W. Herman and H. Elsayed-Ali, "Superheating of Pb(111)," Phys. Rev. Lett. **69**, 1228-1231 (1992).

[26]   J. C. Heyraud and J. J. Mètois, "Growth shapes of metallic crystals and roughening transition," J. Cryst. Growth **82**, 269-273 (1987).

[27]   J. C. Heyraud and J. J. Mètois, "Surface free energy anisotropy measurement of indium," Surf. Sci. **177**, 213-220 (1986).

[28]   V. P. Skripov, V. P. Koverda, V. N. Skokov, "Size effect on melting of small particles," Phys. Stat. Soli. (a) **66**, 109-118 (1981).

[29]   H. H. Andersen, E. Johnson, "Structure, morphology, and melting hysterises of ion-implanted nanocrystals," Nucl. Instr. Meth. In phys. Res. B **106**, 480-491 (1995)

[30]   F. Ercolessi, W. Andreoni, and E. Tosatti, "Melting of small gold particles: mechanism and size effects," Phys. Rev. Lett. **66**, 911-914 (1991).

[31]   Z. Zhang, J. C. Li, and Q. Jiang, "Modeling for size-dependent and dimension-dependent melting of nanocrystals," J. Phys. D: Appl. Phys. **33**, 2653-2656 (2000).

[32]   Z. H. Jin and K. Lu, "To what extent a crystal can be superheated," NanoStruct. Mat. **12**, 369-372 (1999).

[33]   V. B. Storozhev, "The solid-liquid phase transition in nanoparticles contacting with a solid surface," Surf. Sci. **397**, 170-179 (1998).

[34]   Q. Jiang, H. Y. Tong, D. T. Hsu, K. Okuyama, and F. G. Shi, "Thermal stability of crystalline thin films," Thin Solid Film **312**, 357-361 (1998).

[35]   Q. Jiang, N. Aya, and F. G. Shi, " Nanotube size-dependent melting of single crystals in carbon nanotubes," App. Phys. A **64**, 627-629 (1997).

[36]   Q. Jiang and Z. Zhang, "Superheating of nanocrystals embedded in matrix," Chem. Phys. Lett. **322**, 549-552 (1998).

[37]   A. A. Schvartsburg and M. F. Jarrold, "Solid clusters above the bulk belting

point," Phys. Rev. Lett. **85**, 2530-2533 (2000).

[38]   M. K. Zayed, M. S. Hegazy, and H. E. Elsayed-Ali, "Melting and solidification

of indium nanocrystals on (002) graphite," Thin Solid Films **449**, 254-263

(2004).

[39]   S.V. Dukarov, "Size and temperature effects on wetting in supercooled

vacuum condensates," Thin Solid Films **323**, 136-140 (1998).

[40]   J. F. van der Veen, B. Pluis, A. W. D. van der Gon, in *Chemistry and Physics of*

Solid Surfaces VII, Springer-Veilag, 1988, pp. 455-490.

[41]   N. Georgiev, A. Pavlovska, and E. Bauer, "Surface disordering without surface

roughening," Phys. Rev. B **52**, 2878-2888 (1995).

[42]   A. Pavlovska, D. Dobrev, and E. Bauer, "Orientation dependence of the quasi-

liquid layer on tin and indium crystals," Surf. Sci. **314**, 341- 352 (1994).

[43]   K. Mae, V.V. Moshchalkov, and Y. Bruynseraede, "Intensity profiles along the

RHEED streaks for various thin film surface morphologies," Thin Solid Films

340, 145-155 (1999).

[44]   Z. Wang and P. Wynblatt, "The equilibrium form of pure gold crystals," Surf.

Sci. **398**, 259-266 (1998).

[45]   H. P. Bonzel, "Surface morphologies: transient and equilibrium shapes," Interf.

Sci. **9**, 21-34 (2001).

[46]   D. Chatain, V. Ghetta, and P. Wynblatt, "Equilibrium shape of copper crystals

grown on sapphire," Interf. Sci. **12**, 7-18 (2004).

[47]   N. X. Sun, H. Lu, and Y. C. Zhou, "Explanation of the melting behavior of embedded particles; equilibrium melting point elevation and superheating," Phil. Mag. Lett. **76**, 105-110 (1997).

[48]   W. S. M. Werner, C. Tomastik, T. Cabela, G. Richter, and H. Störi, "Elastic electron reflection for determination of the inelastic mean free path of medium energy electrons in 24 elemental solids for energies between 50 and 3400 eV," J. Electron Spectrosc. Relat. Phenom. **113**, 127-135 (2001).

[49]   Z. L. Wang, "Statistical multiple diffuse scattering from rough surfaces in RHEED-beyond the distorted-wave Born approximation" Surf. Sci. **366**, 377-393 (1996).

[50]   G. Meyer-Ehmsen, "Real-space dynamical calculation of diffuse RHEED intensities from disordered surfaces," Surf. Sci. **395**, L189-L195 (1998).

[51]   M. M.-Yoshida, S. Tehuacanero, and M. J.-Yacamán, "On the high temperature coalescence of metallic nanocrystals," Surf. Sci. Lett. **274**, L569-L576 (1992).

[52]   Z. H. Jin and K. Lu, "Melting of surface-free bulk single crystals," Phil. Mag. Lett. **78**, 29-35 (1998).

[53]   J. G. Dash, "History of the search for continuous melting," Rev. Mod. Phys. **71**, 1737-1743 (1999).

CHAPTER V

MELTING AND SOLIDIFICATION OF BISMUTH NANOCRYSTALS

V.1. Introduction and literature survey

The solid-liquid phase transition of nanoscale systems has been extensively studied for the purpose of gaining an atomistic understanding of the phase transition properties and how it is affected by the reduced size [1-6]. Nanocrystals have melting and solidification behaviors that are different from their own bulk materials. An abrupt change in the physical properties upon melting characteristic to first-order phase transition is observed for bulk crystals, whereas that of nanocrystals spreads over a temperature range and has strong size dependent [1-10]. Also, the role of surface and interfacial energies becomes crucial [2,11-15]. While the reduced size is known to cause melting point depression, the effect of the surface and interfacial energies can lead to either melting point depression or superheating for certain crystal morphologies [1-15]. Nanocrystals embedded in a host matrix have melting and solidification behaviors that are mainly controlled by the interfacial energy, nanocrystals grown on relatively inert substrates give information on the thermodynamic nature of the transition with minimal interface effects.

Bi has an anisotropic crystal structure, low bulk melting point, T_0, low partial vapor pressure near T_0, and undergoes negative volume change upon melting [7,16,17]. These properties have stimulated numerous experimental and theoretical studies to better understand its solid-liquid phase transition [18-21]. While a size-dependence melting point depression, consistent with theoretical models, is commonly observed [12,20,21], a

subset of the formed nanocrystals previously observed superheat above T_0 [7,18,19].

Furthermore, experimental and theoretical studies have shown that superheating of the

solid phase is observed for many materials that undergo positive volume change upon

melting [22-25]. Thus, it is believed that the solid-liquid interfacial energy and/or crystal

shape, rather than the volume change upon melting, is the reason for the observed

superheating [16,18].

Because of its structural and thermodynamical properties, Bi has a number of

phases at elevated pressures and temperatures and a wide solid-liquid hysteresis curve

[13,26,27]. Bi in reduced dimensions has also shown many interesting physical properties

that include lattice shrinking [28,29], the presence of a metallic-semiconductor transition

[30], amorphous and metastable phase formation [31], thermoelectricity [32],

superconductivity [33], quantum-size effects [34], and enhanced magneto-resistance [35].

Films deposited at liquid helium temperatures had an amorphous structure exhibiting

superconductive properties [30,33], while those deposited at 300 K up to T_0, showed a

typical rhombohedral Bi structure with morphologies that vary from single crystal films

to a dendrite structure [36-43].

In general, deposition at elevated substrate temperatures increases the surface

diffusion of Bi adatoms, thus producing an ordered crystalline surface; while low

temperature deposition results in microscopically rough surfaces [36-38]. Bi films

deposited on 111-BaF$_2$ substrate at 533 K using molecular beam epitaxy (MBE) showed

a featureless scanning electron microscope (SEM) image consistent with epitaxial film

formation [39]. On the other hand, films deposited at room temperature showed randomly

oriented ~1 μm crystallites [39]. Bi films prepared by pulsed laser deposition (PLD) also

showed a dramatic morphology dependence on the temperature of the substrate during deposition [40]. For epitaxial growth of thermally evaporated Bi on cleaved mica, preheating the substrate to 413 K and maintaining it at that temperature during deposition was found to be essential for epitaxy [41]. This temperature was found to optimize the nucleation rate and the lateral spreading rate of Bi adatoms. Also, it was found that the Bi film is hard to nucleate on a 111-BaF_2 substrate using MBE at temperatures higher than 423 K [42]. A two-step growth process with the film initially nucleated at 373 K followed by growth to a thicker film near T_0 was employed to obtain an epitaxial film with a low level of defects and high electron mobility.

Because of surface energy anisotropy of crystalline solids, crystals of different orientations melt differently. For nanocrystals, the anisotropy in surface energy affects their external shapes as well as their melting behaviors [44,45]. Recrystallized nanocrystals can have shapes and external surface morphologies that differ from as-deposited nanocrystals, and hence, the melting and solidification behaviors can differ between the two types. Dark field electron microscopy was used to investigate the melting of Bi crystallites in as-deposited and recrystallized Bi films on a carbon substrate [18]. As-deposited films were found to have crystallites that are different in shape and in melting behavior from those recrystallized after melting. While a subset of the as-deposited crystallites, with elongated platelet shape, superheated by 7 K above the equilibrium bulk melting point, the recrystallized polyhedral hexagonal shaped nanocrystals in the as-deposited film showed melting point depression [18]. Using the same technique to study the melting of lead nanocrystals, superheating by 2 K was found for extensively {111} faceted platelet-shaped nanocrystals formed in the as-deposited

films [23]. Lead nanocrystals with other shapes melted below the bulk melting point. By recrystallizing a 1000-Å average thickness lead film previously deposited on a graphite substrate at room temperature, Mètois and Heyraud were able to prepare some nanocrystals bounded by minimum energy facets with sharp edges that were able to superheat by ~3 K [22].

Reflection high-energy electron diffraction (RHEED) is a structurally sensitive probe used to obtain real-time information on the top monolayers of a surface, either during film growth or a surface phase transition [46,47]. In the present work, *in situ* RHEED is used to monitor the deposition of Bi on a highly oriented 002-graphite surface. *Ex situ* atomic force microscopy (AFM) is used to study the morphology of the deposited films. Two deposition regimes were observed; growth of solid crystallites below a substrate temperature of 413±5 K, and condensation of the liquid phase above that temperature. The melting point size dependence of the initially formed nuclei, combined with the thermal characteristics of Bi is used to explain liquid Bi formation below T_0 on the graphite surface. Elongated platelet Bi nanocrystals were found to form in the neighbor of the solid/liquid deposition boundary, 415 ± 5 K showed rounded polyhedral as well as elongated platelet Bi nanocrystals. Bi nanocrystals having similar shapes were previously reported to have a resistance against surface melting and showed ~7 K superheating. The change in the diffraction pattern with temperature was used to probe the melting and solidification of as-deposited and recrystallized Bi nanocrystals deposited at 415±5 K. The effect of the crystal shape and size on the melting behavior of the nanocrystals is discussed. The size-dependent supercooling of Bi nanocrystals was also studied.

V.2.   Experimental method

Bi films were prepared and *in situ* studied in ultrahigh vacuum (UHV) chamber $(5.0 \times 10^{-10}$ Torr base pressure) equipped with RHEED. The base pressure of the chamber remained almost constant during melting and solidification experiments, while a small increase was observed during deposition. Highly oriented pyrolytic 002-graphite (HOPG) was used as a substrate. HOPG is chemically inert. Accordingly, the deposited Bi interacts with the graphite substrate via the Van der Wall attraction force with no inter-diffusion or chemical compound formation. The graphite substrate is loaded in the UHV chamber immediately after cleaving it in air. The substrate is mounted on a resistively heated stage capable of reaching temperatures up to 1000 K. Before deposition, the graphite substrate is heated to ~ 770 K for 10 minutes in order to evaporate any adsorbed gases and obtain a clear graphite RHEED pattern. A K-type thermocouple was used to measure the surface temperature of the substrate and the deposited film. The thermocouple is calibrated in air to the bulk melting point of pure bismuth. This calibration is performed before and after the experiment in order to assure that the properties of the thermocouple were not altered during the heating and cooling cycles. A temperature measurement uncertainty of ±1 K was obtained.

Bi with 99.999% purity is evaporated from a resistively heated tungsten basket. The substrate temperature is kept at 423 K for ~10 min before deposition. RHEED is used to monitor the deposition and the growth of the deposited films. The film mean thickness is obtained using a calibrated quartz crystal thickness monitor. By controlling the current applied to the heater filament, the deposition rate is maintained between 0.4 - 0.7 Å s⁻¹. Bi has an average Bi-Bi bond length of 3.24 Å, which is used to express the

measured film thickness in ML. Films with different mean thickness, from 1.5 ML to 33 ML, were prepared. As-deposited samples are investigated immediately after cooling to room temperature, while recrystallized samples are heated a few degrees above the melting point of bulk Bi and maintained at that temperature for a few minutes, and then slowly cooled to room temperature. The reappearance of the Bi diffraction pattern during cooling indicates its recrystallization.

RHEED diffraction patterns are obtained using a 9.7-kV electron beam. A computer-controlled charged coupled device (CCD) camera was used to record the diffraction patterns that are displayed on a phosphorus screen. The heating and cooling rates were kept almost constant between 3 and 4 $Kmin^{-1}$, by controlling the current of the heating stage. These heating rates are in the range of previous melting and solidification experiments where subset Bi showed a time-dependent melting behavior and a subset was able to superheat by ~7 K [18]. Real time RHEED patterns are obtained during film deposition to study the structural evolution of Bi deposited at different temperatures. Each RHEED pattern is acquired in about 170 to 400 ms, depending on the image quality. A similar or shorter acquisition time is used in melting and solidification experiment, thus, temperature changes during the pattern acquisition are negligible. The low Bi vapor pressure near the bulk melting temperature, $< 2 \times 10^{-10}$ Torr [17], allows for conducting the melting experiment with negligible atom loss by evaporation. Bi has a relatively low bulk melting point (544.52 K), which facilitates the melting experiment. Bi films are easily re-evaporated off the substrate at the end of the investigation, by holding the substrate at 970 K for few minutes. A clear graphite pattern is observed, which

indicates complete evaporation of the deposited Bi off the graphite. Thus melting and solidification of different film thicknesses can be performed on the same substrate.

For the purpose of film morphology studies, films with different mean thicknesses were prepared in the UHV chamber. After completion of the film deposition and heat treatments, if any, the chamber is vented to the atmospheric pressure using argon gas and the films are taken out for *ex situ* AFM investigations. The lateral and height resolutions of the used AFM is 1 nm and < 0.1 nm, respectively, as specified by the manufacturer.

RHEED diffraction patterns are obtained using a 9.7-kV electron beam. A computer-controlled charged coupled device (CCD) camera is used to record the diffraction patterns that are displayed on a phosphorus screen. Real time RHEED patterns are obtained during film deposition to study the structural evolution of Bi deposited at different temperatures. Each RHEED pattern is acquired in about 170 to 400 ms, depending on the image quality. After film completion, the chamber is vented to atmospheric pressure using argon gas and the films are taken out for surface morphology studies. An *ex situ* AFM with lateral and height resolutions of 1 nm and < 0.1 nm, respectively, as specified by the manufacturer, is used. Films deposited at different deposition temperatures were studied.

V.3. Results and discussion

V.3.1. Film deposition and morphology

The growth dynamic of Bi nanocrystals was monitored using *in situ* RHEED while the *ex situ* AFM is used to study the film morphology after deposition. Two deposition regimes were observed: growth of solid crystallites below a substrate

temperature of 413±5 K, and condensation of the liquid phase above that temperature. The melting point size dependence of the initially formed nuclei, combined with the thermal characteristics of Bi was used to explain liquid Bi formation below T_0 on the graphite surface. The morphology of films crystallized from the condensed liquid Bi was found to be different from those directly crystallized from the vapor. The dependence of the formed morphology on the degree of liquid supercooling is also discussed.

V.3.1. Low temperature solid film deposition

After heating and then cooling the graphite substrate, the RHEED pattern, taken at room temperature, indicated a transmission-like diffraction pattern consisting of spots aligned along rods normal to the surface. The RHEED pattern of the graphite surface was indexed based on 3-dimentional (3D) reciprocal lattice spots seen in the $1\bar{1}0$ zone with the electron beam parallel to the zone axis. Detailed analysis of the graphite RHEED pattern can be found elsewhere [25]. The diffraction features observed were consistent with a clean graphite surface. Thermal deposition of Bi on graphite was studied by obtaining real time RHEED images during deposition. Fig. 5.1 shows RHEED patterns of the surface with different Bi coverage deposited at room temperature. The graphite spot intensity becomes dim at a Bi coverage of 0.5 ML and a diffuse background appears. As the deposited film thickness is increased to an average of 4-6 ML, the diffraction intensities of the Bi spots increase. Indexing of these spots show that they are characteristic of the rhombohedral structure of Bi. The RHEED intensity of the (002) graphite spot decayed continuously with Bi deposition and showed no intensity oscillation. This behavior is consistent with a 3D growth forming islands. The intensity of the 220-Bi spot increased with the deposited thickness. After deposition of ~8 ML, the

Bi diffraction spot intensity monotonically decreased. The increase of the Bi diffraction intensity and reduction of the graphite diffraction intensity is due to the increase in the surface coverage with Bi. However, as the Bi coverage was further increased, the density of misaligned crystallites increased, resulting in a decrease in the Bi RHEED spot intensity. After deposition of ~16 ML, the shape of the Bi spots changed from nearly rounded to elongated streaks, with the major axis normal to the substrate surface. Elongated RHEED spots indicate the formation of crystals with asymmetric shape, which was confirmed later using ex situ AFM. With further Bi deposition, the elongated RHEED spots remained almost the same with no shape change. Films deposited at a substrate temperature of 373 K showed RHEED patterns that were thickness dependent similar to that observed for those deposited at room temperature but with no noticeable elongation in the spots at higher thicknesses.
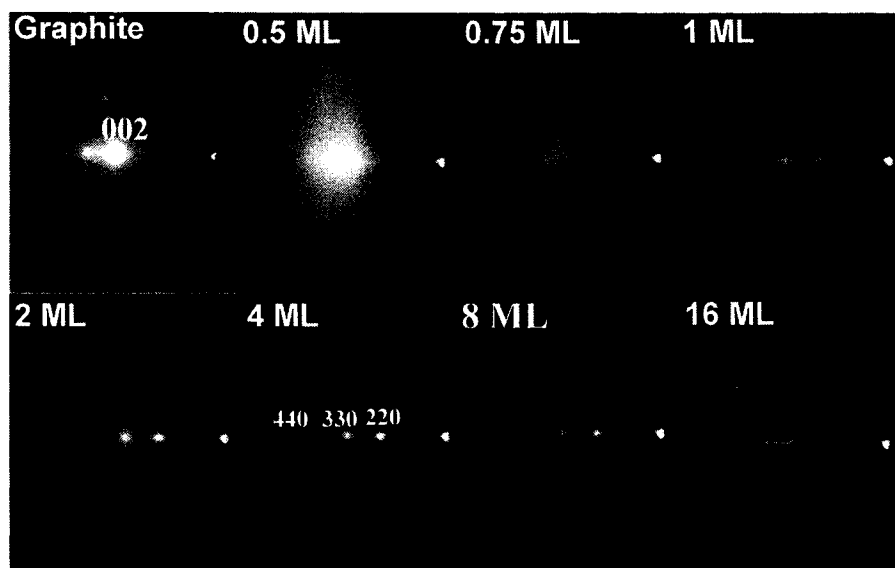
FIG. 5.1. Real time RHEED patterns taken during Bi deposition at room temperature. The graphite spot intensity decays and that of Bi start to appear after deposition of ~ 0.5 ML. The spot intensities of Bi increase with the deposited thickness up to ~ 8 ML. Elongated RHEED streaks at 16 ML indicate coalescence and formation of asymmetric shape crystallites.

For Bi films deposited on graphite with the substrate temperature between 300 K

and 373 K, no change in the relative spot positions was observed with the deposited

thickness. This remained the case from the initial formation of detectable transmission Bi

spots up to the maximum studied Bi thickness. Also, no change in the relative spot

position was observed as the deposition temperature was increased from 300 K to 373 K,

indicating no change in the film growth direction. Fig. 5.2 shows line profiles of Bi

RHEED patterns in a direction normal to the substrate surface for 8 ML films deposited

at 300 K and 373 K. Narrower peaks with higher intensities were observed for films

deposited at 373 K. This indicated that films deposited at 373 K have an enhanced

average crystallite size and/or a higher degree of orientation relative to those deposited at
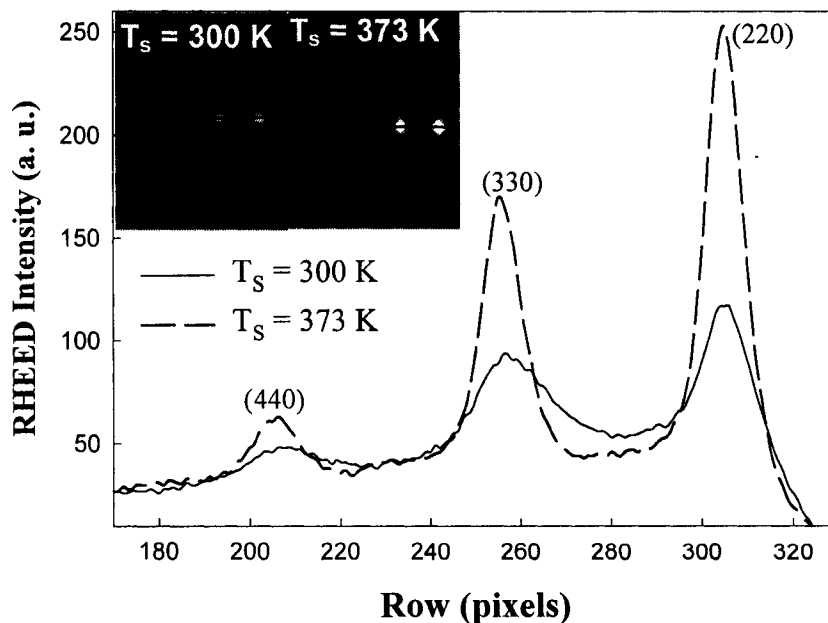
room temperature.

FIG. 5.2. Line profiles, normal to the substrate surface, of RHEED patterns taken after deposition of 8 ML Bi films deposited at two different substrate temperatures.

Ex situ AFM in air was used to study the structural morphology of the films after deposition. Figure 5.3 shows the obtained images for 25 ML Bi films deposited at 300 K and 373 K along with the corresponding RHEED patterns obtained in the deposition chamber, after terminating the deposition. The AFM images show highly ordered, 3D crystallites with layered triangular pyramid-like shapes. The edges of these crystallites become more defined and sharper as the deposition temperature is increased. The morphology of the formed crystallites indicates that nucleation on the top of a formed triangular Bi layer is likely. The growth of these nuclei occurs simultaneously with the lateral growth of the layer underneath in a 2D layer-by-layer-like growth mode. This crystal shape and growth mode results in elongated RHEED spots that continuously decay in intensity with deposition. This is because the average lateral crystalline size parallel and normal to the electron path are not equal due to the triangular pyramid surface morphology. RHEED intensity is sensitive to growth dynamics within the electron penetration depth over the probed area. Since the growth occurs concurrently in isolated crystallites with different heights, no RHEED intensity oscillation of the 002 Bi spot was observed, in spite of the layer-by-layer growth in each pyramid. Similar triangular-shaped crystallites formed by the same growth mode were previously reported for epitaxial Bi films deposited on a cleaved mica substrate [41,48]. This growth mode indicates solid film formation from the vapor phase.

As the substrate temperature was increased from 300 K to 373 K, the number of triangular crystallites found in the scanned area decreased. While this observation suggests a decrease in the nucleation density with temperature, other possible causes include repening, annealing due to deposition at a higher temperature, and coalescence
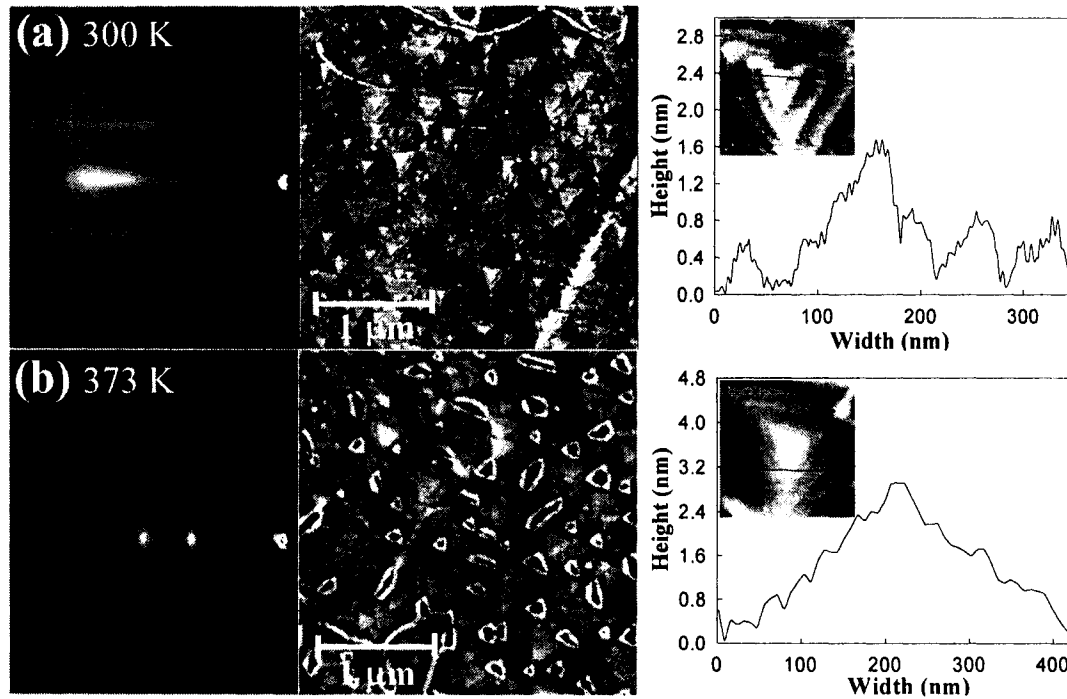
FIG. 5.3. RHEED pattern and *ex situ* AFM images along with line profiles of AFM through a smaller scanned area of 25 ML Bi films deposited at two different substrate temperatures: (a) T_s = 300 K, and (b) T_s = 373 K.

are also possible. From Fig. 5.3, an enhancement in the lateral growth of the deposited Bi and increased coalescence during growth is observed for films deposited at 373 K as compared to films deposited at 300 K. This enhancement in lateral size and the decrease in the nucleation density results in the transformation of wide elongated RHEED spots shown in Fig. 5.3(a) to the small circular spots shown in Fig. 5.3(b). The full width at half maximum of the RHEED spots is reduced with increased crystal size. Increased coalescence at 373 K leads to trench formation. The step heights forming the triangular pyramid structure in Fig. 5.3(a) and 5.3(b) were mostly found to be 0.4±0.1 nm, while a small number has heights of 0.8±0.1 nm. The Bi structure can be visualized as a layered hexagonal structure in the [111] direction with d_{111} = 11.862 Å, containing three

successive layers with a 3.9 Å separation distance. Thus, the measured step heights correspond to single and double heights of the Bi structure with its (111)-facet oriented parallel to the substrate surface in pseudocubic notation. Measurements of the terrace heights showed no variation with deposition temperatures within the studied range.

V.3.2. High temperature liquid phase condensation

RHEED observation of Bi deposition at different graphite substrate temperatures showed that solid crystalline films are directly formed on the surface for substrate temperatures up to ~410 K. The lowest substrate temperature considered was 300 K. As the graphite substrate temperature was increased higher than 373 K, the Bi diffraction pattern became weaker as compared with films of equal thickness deposited at different temperatures. Fig. 5.4(a) shows RHEED patterns taken during deposition of a 25 ML Bi film deposited at substrate temperatures from 403 K to 418 K. The reduction in the RHEED spot intensity with substrate temperature can be seen by comparing Fig. 5.4(a) with that of Fig. 5.3(b) taken at 373 K. The intensity of the 220 spot of the 25-ML film deposited at 410 K remained almost constant for a period of hours after deposition. However, a faint diffraction pattern that slowly increased in intensity after deposition of 25 ML was observed for films deposited and maintained at 413 K. Films deposited at temperatures higher than or equal to 418 K showed a diffuse pattern with a background intensity that decreased with increased film thickness. This diffuse pattern remained unaffected by the deposited Bi thickness up to 100 ML. Also, when a 25 ML film was left overnight at 418 K deposition temperature, no change in RHEED intensity was observed. However, when these films were cooled, a transmission RHEED pattern started to appear in the temperature range between 406 K and 392 K as shown in Fig. 5.4(b).

Strong RHEED patterns corresponding to twinned or multi-azimuth orientations were observed as the temperature was decreased to 300 K. A diffuse diffraction pattern is an indication of the lack of long-range order in the deposited film. The appearance of a Bi diffraction pattern after cooling below the supercooling limit indicates that these Bi films were initially formed in the liquid phase and precludes the possibility that a solid amorphous film was initially formed.
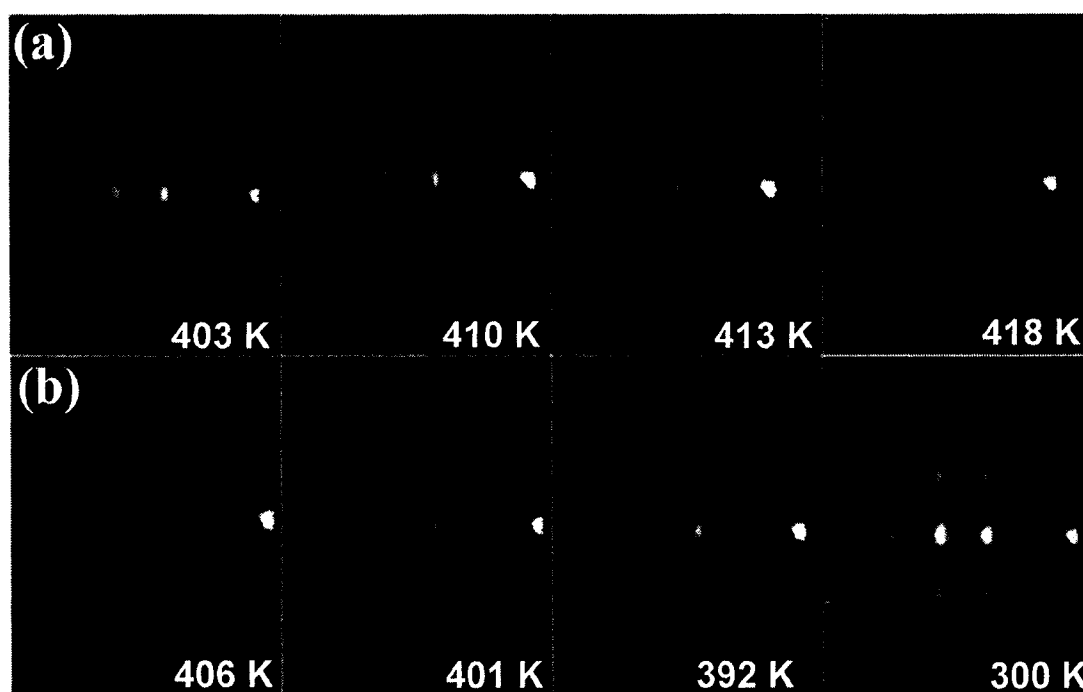
FIG. 5.4. (a) RHEED pattern taken after deposition of 25 ML Bi films at different substrate temperatures. The deposition temperature of ~ 415±5 K is the solid/liquid formation boundary. (b) RHEED pattern taking during cooling to room temperature of 25 ML Bi film initially deposited at 433 K.

Condensation of liquid films on different substrates at temperatures less than T_0, was previously reported. In a pulsed laser deposition experiment of Bi on a glass substrate, followed by the observation of film morphology using *ex situ* STM and AFM,

it was concluded that the film condensed in the liquid phase when deposition was performed with the substrate temperature at 458 K. The liquid droplets crystallized with cooling forming submicron spherical shaped isolated crystallites [40]. At lower deposition temperatures, Bi nucleated directly into the solid phase forming films with smooth surfaces [49]. Deposition of Bi on Si(100) did not show similar behavior. Thus, formation of the liquid phase in pulsed laser deposition was attributed to the high energy of the laser-ablated Bi and the absence of substrate influence. Scanning tunneling microscopey, Auger electron spectroscopy, and x-ray photoelectron spectroscopy revealed the formation of indium nano-drops in a 6 ML thermally deposited film on a Ge(001) substrate in UHV at room temperature [50]. The presence of indium in the liquid phase, even at room temperature, was attributed to the internal stress resulting from the lattice mismatch between the film and the substrate, and to the reduced dimensionality of the deposited film. Both factors are known to decrease the equilibrium melting point. Also, liquid Bi droplets with spherical shapes were previously detected using *in situ* electron microscopy for films deposited at temperatures above 423 K and having dimensions less than 150 Å [51]. Coalescence as well as transformation of these droplets into solid crystals during growth was observed.

RHEED probes a layer of an average thickness given by the inelastic mean free path which is ~ 9 nm for the 9.7-kV RHEED electron beam. Thus, diffuse RHEED patterns could be due to surface melting or due to liquid phase condensation. In order to differentiate between these two possibilities, the film was cooled to 300 K then the RHEED intensity of the (220) Bi spot was measured as a function of temperature. The intensity was normalized to that measured at 325 K. Fig. 5.5 shows the natural log of the

normalized RHEED intensity of the (220) spot for 45 ML and 90 ML Bi films deposited at 423 K. A decrease in spot intensity with temperature was expected due to the enhanced atomic mean-vibrational amplitude as described by the Debye-Waller effect. However, a sharp drop in the RHEED intensity occurred as the nanocrystals lose long-range order within the shell probed by the electron beam, which appeared only at ~ 10-15 K below the bulk melting point of bismuth, $T_0 = 544.52$ K. The normalized intensity vanished at ~ 4 K below T_0, indicating complete film melting. During cooling, the liquid Bi remained in the liquid phase down to 418 K, ~125 K below T_0. This behavior is repeatable with about 4-10 K shift toward higher values in the onset points of melting and freezing after the first heating-cooling cycle. Within the experimental error, no significant change is observed for further heating-cooling cycles. Films deposited at room temperature also showed reproducible heating-cooling hysteresis curves, however in this case, with a small shift towards lower temperatures for the onset of melting and freezing. These observed shifts are expected to be due to the dependence of the solid-liquid transition on the size distribution and/or shape of the crystallites, which changes with heating and melting after deposition. Surface melting is a reversible phase transition with a defined onset point for clean surfaces [24]. Since the decrease in the measured RHEED intensity due to surface melting occurred only within a few degrees from T_0, we conclude that Bi condensed as liquid droplets at temperatures as low as 125 K below T_0.

Condensation of liquid Bi at a substrate temperature as low as $T_0 - 125$ K cannot be simply explained based on substrate effect since graphite is an inert substrate with no known chemical reactivity with Bi and, therefore, should have only a weak influence on growth. The condensation of liquid Bi from the vapor is most likely related to the

tendency of Bi to show a large degree of supercooling and size dependent melting point depression. It is interesting that the $T_0 - 125$ maximum supercooling temperature that we observed for Bi in Fig. 5.5 was the same as the lowest temperature for which condensation of liquid Bi from vapor occurred. Melting point depression by few degrees was observed in Fig. 5.5, but is know to be strongly dependent on size for Bi as well as other nanocrystals [13,29].
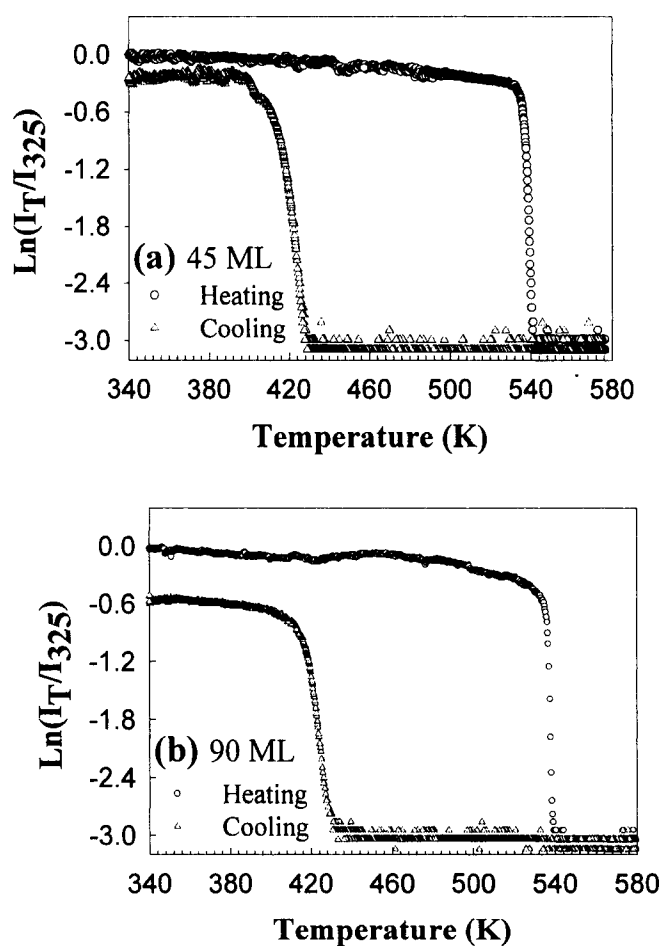
FIG. 5.5. Natural log of the normalized RHEED intensity of the (002) Bi spot as a function of temperature during heating and cooling of (a) 45 ML and (b) 90 ML Bi films initially deposited at 423 K.

The size effect on the melting point was described by different theoretical phenomenological models [7-10,29,53-55]. All of them predict a melting point depression proportional to the reciprocal of the particle radius as described in chapter 2. Examples of these models are the homogenous melting model [7,8,9], the liquid drop model [51], and the lattice vibration-based model [29]. The known physical constants of Bi (T_0 = 544.52 K, ρ_s = 9.8 g/cm^3, ρ_l = 10.07 g/cm^3, L = 5.19 × 10^{-8} erg/g, γ_{sl} = 61 erg/cm^2, γ_{sv} = 550 erg/cm^2, γ_{lv} = 375 erg/cm^2, h = 0.4074 nm, S_{vib} = 3.78 J mole^{-1} K^{-1}, R = 8.3142 J mole^{-1} K^{-1}) are used to calculate the melting point size dependence of Bi [7,29,51]. Figure 5.6 shows the size dependent behavior predicted by these models. Although these models show the same trend, there is some discrepancy at smaller sizes. Also, these models consider only spherical-shaped particles and do not include the crystallite shape effect. Therefore, the predicted melting point of the particle is only an estimate. From Fig. 5.6, particles with sizes between 5-20 nm can melt at room temperature. At 420 K, both the homogenous melting model and the lattice vibrational-based model predict that a particle of ~32 nm size would melt, while the liquid drop model requires that the particle size be less than ~8 nm to melt at 420 K. Considering the 0.203 nm atomic radius of the Bi atom, these sizes correspond to clusters containing roughly 4 × 10^6 atoms for the 32 nm cluster and 6 × 10^4 atoms for the 8 nm cluster, which are apparently very large compared to that necessary to form stable nuclei. Based on the above, one would suggest that the Bi nuclei are originally formed in the liquid phase because of the size-dependent melting point depression. However, as the nuclei grew, it solidified when the deposition temperature was below the freezing point. This freezing point is observed from Fig. 5.5 to be between 410 and 424 K based on a RHEED

measurement of films solidified from the melt. From the RHEED observation of Bi condensed on graphite, we observed a pattern for temperatures below 415±5 K (Fig. 5.4), which is in agreement within the expected experimental error with the maximum supercooling temperature obtained from Fig. 5.5. Thus, the liquid nuclei grew and remained in the liquid phase when the films were deposited at temperatures above the maximum possible supercooling temperature.
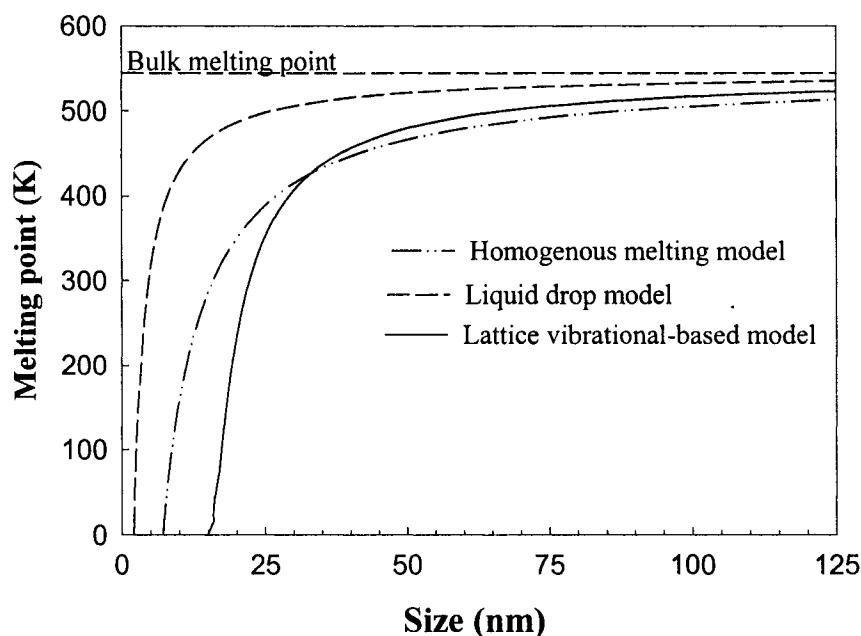
FIG. 5.6. Melting point-size dependence of Bi as calculated from different theoretical models.

For a deposition substrate temperature above the maximum supercooling point, the liquid Bi nuclei will be trapped in the supercooling state and grow forming larger size liquid droplets. The small size of the stable nucleus in the Bi/graphite system, relative to

crystallites obtained at growth termination, reduces the melting point of the stable nucleus and increases the amount of supercooling, as predicted by different size dependent melting models and observed experimentally [29,53,55-57]. The values of surface, interfacial, and bulk free energies involved in nanocrystal growth affect the size of the stable nucleus. In general, the amount of supercooling is affected by the size of the crystal as well as the melting and freezing kinetics [15,53,56]. For clusters of sizes larger than the stable nucleus, the amount of supercooling was reported to vary linearly with the reciprocal of the cluster size, assuming heterogeneous solidification due to its dominance and low activation energy. In Fig. 5, we observed an amount of supercooling for 45 ML that is ~ 4 K larger than that for 90 ML, which is attributed to the average size increase with the film coverage.

In ordered to study the effect of the freezing kinetics on the film supercooling, we obtained melting-freezing curves similar to those of Fig. 5, but with different cooling rates. The films were cooled from the same initial liquid overheating point, 10 K above T_0 of Bi. As the cooling rate was increased from 0.9 K/min to 9.5 K/min, ~ 6 K increase in the film maximum supercooling was observed. These cooling rates are the experimentally feasible rates using the current setup. The effect of the cooling rate on the amount of melt supercooling was reported to vary. For slow cooling rates, the amount of supercooling remains basically unchanged. For example, for PbTe no dependence on the cooling rate was observed for cooling rates between 0.5 and 3.0 K/min [58]. With the increase in the cooling rate the amount of supercooling could increase. For example, the amount of supercooling changed by ~ 46 K as the cooling rate was increased from 90 K/min to 456 K/min for $Bi_{95}Sb_5$ [59]. The ~ 6 K shift that we observed in the amount of

supercooling with cooling rate is about the same as the stated error in the RHEED observation of the solid/liquid formation boundary for Bi condensation on graphite, 415±5 K. In addition, to check on the stability of supercooled Bi droplets, melted Bi crystallites were left in the supercooled state overnight at 10-15 K above the freezing edge. No sign of solidification was observed indicating that Bi has a stable supercooled liquid. Thus, within the studied experimental conditions, the freezing rate has little effect on the kinetics of liquid condensation due to the relatively large and stable supercooling of Bi nano-droplets.

AFM analysis of films crystallized from the melt showed that these films have morphologies different from those grown from the vapor. While triangular layered shape crystallites were formed at a substrate temperature of 300-373 K, rounded or elongated platelet shaped crystallites were formed for films deposited at 413-598 K. Fig. 5.7 shows *ex situ* AFM images and line profiles of films deposited at substrate temperatures between 413 K and 532 K. Two different morphologies could be recognized based on the film deposition temperature. Those deposited in the neighborhood of the solid/liquid condensation temperature, which is the maximum supercooling point 415±5 K, form elongated platelet shaped crystals; while those deposited at higher temperatures form rounded polyhedral crystals. Films deposited at 413 K, a few degrees below the maximum supercooling point, showed relatively wide elongated crystallites with almost flat top surfaces. These films produced a faint RHEED pattern, as shown in Fig. 5.4(a). Films deposited at 423 K, several degrees above the maximum supercooling temperature, had crystallites of mixed shapes consisting of rod-like and rounded crystallites with curved top surfaces. These films produced diffuse RHEED pattern similar to those depos-
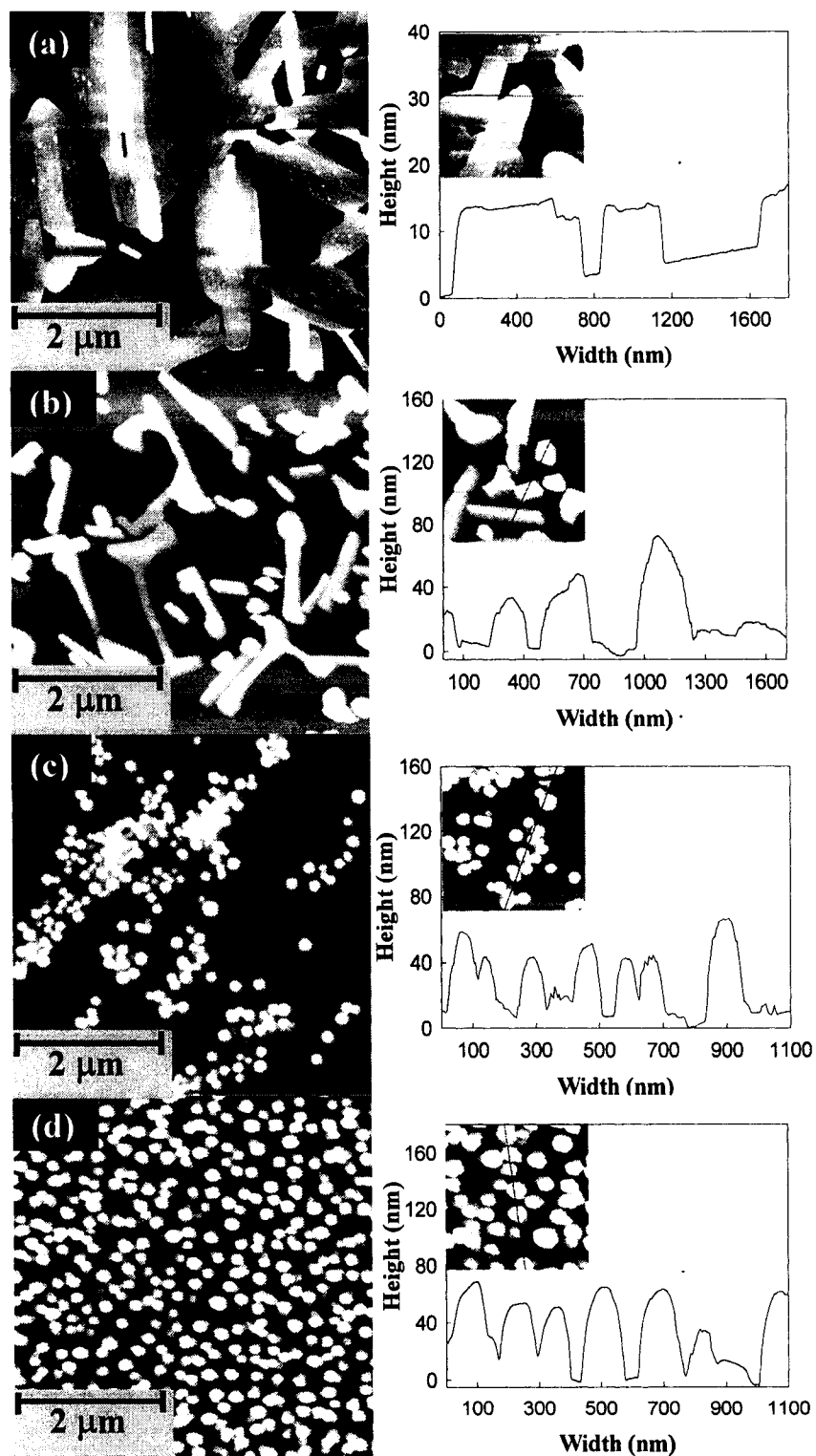
FIG. 5.7. AFM images, along with line profiles of Bi films deposited at different temperatures: (a) 25 ML deposited at 413 K, (b) 25 ML deposited at 423 K, (c) 25 ML deposited at 453 K, and (d) ~ 33 ML deposited at 498 K.

ited at 418 K, as shown in Fig. 5.4(a). Finally, films deposited at a substrate temperature of 453 K and 498 K showed almost identical rounded polyhedral crystallites with curved top surfaces. Because the RHEED image is due to diffraction from crystallites forming the film within the probed area, and is affected by shadowing, no significant change in the diffraction pattern after cooling to 300 K is observed for films crystallized from the liquid phase. Misalignment or randomness of the film crystallites in addition to height differences between the crystallites, shown in Fig 5.7, increase the shadowing effect and the shape and size insensitivity of RHEED [57].

The different crystallographic shapes of crystallites deposited at temperatures near 415 ± 5 K or higher then cooled to room temperature, indicate that the formed morphology is affected by the degree of liquid supercooling of the initially condensated liquid. Because of the presence of an energy barrier for solid nucleation, which is affected by the volume change upon solidification and the release of latent heat, the melt can be supercooled. The presence of short-range order is characteristic of a supercooled melt [58-61]. The melt stays in this metastable supercooled state until spontaneous homogenous or heterogeneous solidification occurs. Because the height of the energy barrier for solidification decreases as the amount of supercooling increases, different crystallographic structures may be formed depending on the initial supercooling point of the melt. Negative volume expansion upon melting is a shared property between Bi and water. For water, this expansion is due to the formation of a low-density cage structure created by hydrogen bonds, which link one water-molecule to the next [55,62]. For Bi, the negative volume change upon melting is thought to be due to liquid Bi having well-defined, long-lived, high-density clusters [62]. For $\sim$ 4.5-7.5 nm liquid Bi clusters,

supported on weakly interacting carbon substrates, interference enhanced Raman spectroscopy showed no change in the short-range order including bond distances, the number of nearest neighbors, and bond angle-distribution disorder [63]. A neutron diffraction study showed that there is some similarity between the structure of liquid and solid Bi [63]. We also note that water crystallized with different morphologies and structures based on the initial supercooling point from which the liquid was crystallized [55].

Thus, we conclude that the formation of different crystallographic shapes upon cooling of the deposited Bi is due to solidification from different supercooling regions. Rod-like Bi crystallites were formed for films deposited at substrate temperatures between 413 K and 423 K. At these temperatures, the condensed Bi nucleates in the form of a highly supercooled liquid that can be described as a quasi-liquid with short-range order [60]. Considering that solid Bi has a highly anisotropic structure and its highly supercooled melt has properties closer to that of the solid than to the liquid, the formation of these crystal shapes can be explained by the presence of order in the supercooled melt. Highly anisotropic crystal growth that induces anisotropic crystal shapes has been previously reported for Bi films grown by PLD [27]. Rounded or polyhedral crystal shapes were formed for Bi films solidified from less supercooled liquids where atoms have higher mobility and less anisotropic properties.

V.3.1.3. As-deposited and recrystallized nanocrystals deposited at 425 K

From Fig. 5.7, it is clear that films deposited around 415 ± 5 K formed rounded polyhedral as well as elongated platelet Bi nanocrystals. Bi nanocrystals having similar elongated platelet shape previously showed ~7 K superheating [18]. Thus, 125 K is

chosen as an optimum deposition temperature to prepare thin films with nanocrystals having a shape of potential superheating. After cooling to room temperature, as-deposited and recrystallized Bi films showed a transmission diffraction pattern consisting of spots aligned along rods normal to the surface. The patterns were indexed based on the 3-dimentional (3D) reciprocal lattice mesh of the rhombohedral structure of Bi. The RHEED pattern of as-deposited 1.5 ML Bi films and its corresponding indexing is shown in Fig. 5.8(a). As-deposited films with coverage of 1.5 ML – 10 ML showed similar patterns. The pattern is composed of superposition of two spot sets representing two different diffraction zones, $\langle 1\bar{1}\bar{1}\rangle$ and $\langle 0\,0\bar{1}\rangle$, with the [110] is a common direction. This indicates that Bi grows on the HOPG surface as ensembles of 3D nanocrystals have [110] perpendicular to the substrate surface. The presence of two diffraction zones indicates that the nanocrystals have different lateral orientations on the basal graphite plane, or have finite misalignment angels relative to each other, $\sim 40°$, which is the angel between the observed zone directions. Formation of nanocrystals with two or more lateral orientation, due to substrate effects, has been previously reported [65,66]. Using AFM, we observed elongated Bi nanocrystals that are influenced by the crystal symmetry of the substrate in spite of the weak chemical interaction. Also, some spots corresponding to the graphite surface (pointed at by arrows in Fig. 5.8) were still observable even at higher film coverage. This is indicative to the low surface coverage of the formed Bi crystallites. As the Bi coverage increased to 15 ML and up to the maximum thickness studied, Fig. 5.8(b), the misalignment and randomness of the grown crystallites in the as-deposited films increased. This results in diffraction patterns that are characteristic to textured films [67]. Regardless of the multi-zone diffraction feature and/or textured film growth, no cha-
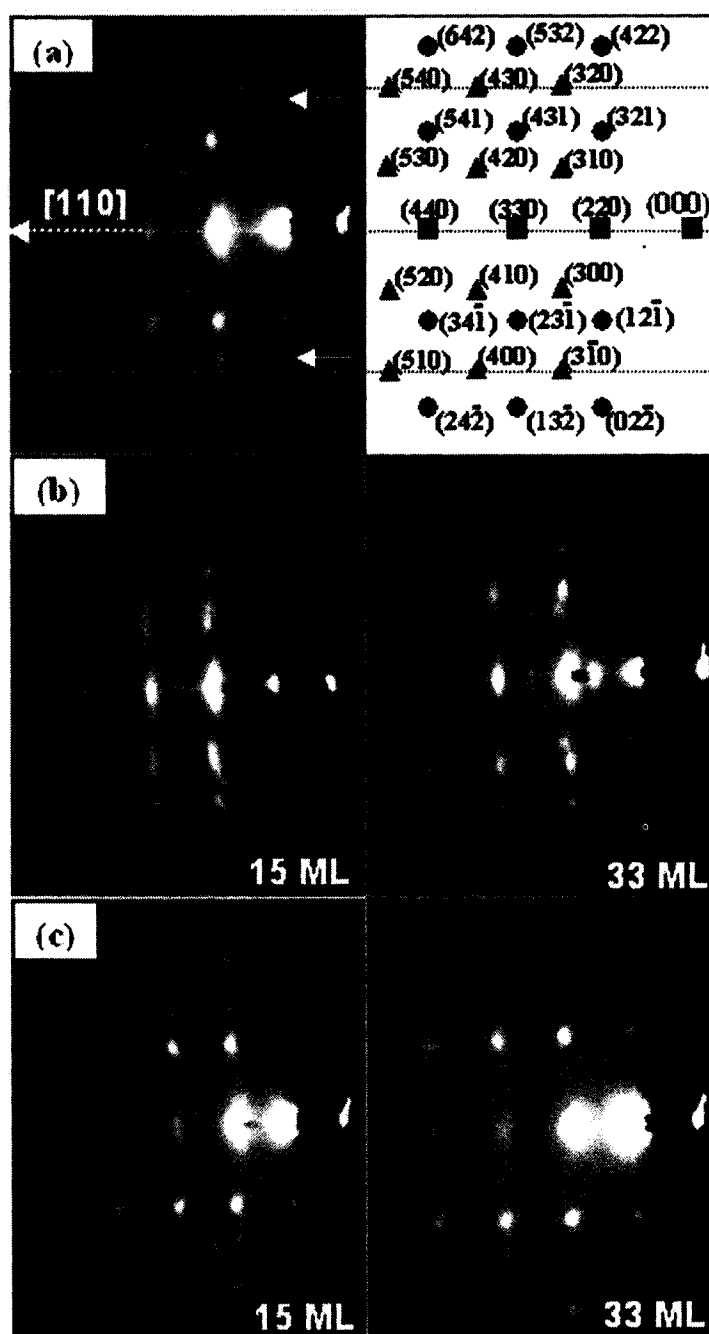
FIG.5.8. (a) RHEED pattern of as-deposited 1.5 ML Bi film and its corresponding 3D indexing ($\bullet$: spots of $\langle 1\bar{1}\bar{1}\rangle$ diffraction zone, $\blacktriangle$: spots of $\langle 00\bar{1}\rangle$ diffraction zone, and $\blacksquare$: spots of the common [110] direction). RHEED patterns of (b) as-deposited, and (c) recrystallized Bi films of 15 ML and 33 ML mean thickness. The films were deposited at 423 K and the patterns were taken after cooling to room temperature for both as-deposited and recrystallized films. The arrows pointing at graphite spots that are still observable even at large film thickness due to incomplete surface coverage.

ange in the relative spot positions, within the experimental error, was observed as the film thickness was increased. This indicates that no structural and or orientation change with the thickness occurred.

For 1.5 ML −10 ML films, no noticeable change in the RHEED pattern is observed between as-deposited and recrystallized films. However, the RHEED patterns of the 15- and 33-ML Bi films changed after recrystallization from that of textured films to patterns of films that have two orientation crystal sets. Moreover, the $\langle 1\bar{1}\bar{1}\rangle$-diffraction zone in the recrystallized films prevailed and the diffraction spots of the $\langle 00\bar{1}\rangle$-zone was bearly seen for 33-ML film. Such pattern suggests that the crystallites are preferably oriented along the $[1\bar{1}\bar{1}]$ than in $[00\bar{1}]$. Another consideration is that the RHEED penetration depth and shadowing effects could affect the diffraction pattern [57]. RHEED probes a shell given by the inelastic mean free path of the electron beam within the probed nanocrystals, which is ~ 9 nm for 9.7 kV electron beam into Bi as calculated from a general equation of IMFP [68]. Within this probed depth, the RHEED pattern is a result of diffractions from all crystallites forming the film in the few mm^2-probed area. The shadowing effect is expected to increase with increasing film thickness because of the anisotropic crystal growth that results in height differences between the crystallites forming the film. The effect of the shadowing is limited at the lower coverage ratios. Thus, the dominance of one diffraction zone over the other is mainly due to film orientation enhancement.

Post deposition AFM was used to study the morphology of as-deposited and recrystallized Bi films as shown in Fig. 5.9. As-deposited Bi films were found to form

3D nanocrystals with different shapes and sizes, while those recrystallized from melt were found to form nanocrystals with nearly shaped but different sizes. Nanocrystals with different shapes including rounded, polyhedral, elongated platelet, and triangular are observed in as-deposited films. For the recrystallized films, facetted polyhedral-shaped nanocrystals with curved edges and in some cases with sharp edges, were observed. Formation of crystal facets is due to the anisotropic surface energy and the surface free energy temperature and size dependence. Rounded or curved surfaces indicate the presence of all surface orientations in the formed nanocrystals, however, sharp-edged shapes indicate missing orientations in the formed nanocrystals [69]. As reported previously, the curved regions increase in size with temperature at the expense of the plain facets due to the decrease in surface energy anisotropy until a spherical shape is formed as the nanocrystal is completely melted [44,45]. Annealing near T_0 or cooling from the melt allows all possible surface orientations to appear in the final form of the nanocrystals.

The nanocrystals were uniformly distributed throughout the substrate surface except at terrace edges where a higher density of nanocrystals is found. This is because among all possible nucleation centers terrace edges offer minimum energy barrier for nucleation. The nanocrystals that nucleated at terrace edges grew outward as observed in Fig. 5.9. Thus, the distribution of the nanocrystals was influenced by the density of substrate terrace edges, which is random due to cleavage. The majority of these crystallites were found to be aligned either parallel to each other, with ~ 5° misalignment, or intercepts at angles of either 60° or 120°. For few crystallites intercept angles of 30° and 90° were found. This growth directionality suggests that the growth of Bi is influen-
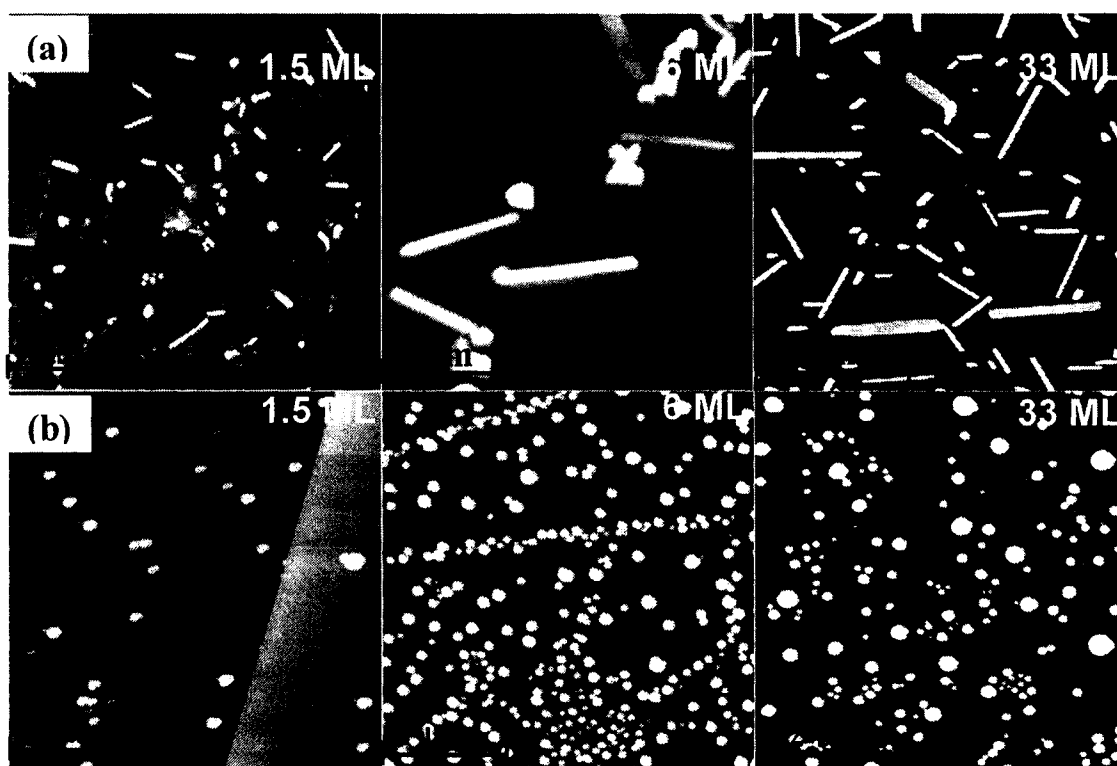
FIG.5.9. AFM images of (a) as-deposited and (b) recrystallized Bi films with different mean thicknesses. Elongated nanocrystal that align themselves in the direction of minimum lattice misfit and angular distortion are observed in the asdeposited films. Recrystallized films are formed in more rounded polyhedral similar shapes.

ced by the graphite structure in an epitaxial-like growth mode, in spit of the weak interaction with the substrate. In this case the overlayer has lattice spacing different from that of the substrate but grows with an orientation that is affected by the substrate. A similar observation was reported for the growth of Bi on III-V(110) substrates [70]. It is the weak interaction between these substrates and Bi and the use of very low deposition temperature, 30 K, that enabled such epitaxial directional growth in spite of the presence of a large lattice mismatch, ~ 20% [70]. For a graphite substrate, Bi adatoms were reported to be highly mobile on its basal plane and the growth was site limited rather than diffusion limited [43]. Because of the inertness and weak interaction of graphite with Bi,

in addition to unrestricted adatom diffusion, Bi favorably grows in directions of minimum mismatch with the graphite substrate. Based on the structure symmetry of Bi and 002-graphite plane, these epitaxial relations were found to be either with $[110]_{Bi} \| [120]_{Graphite}$ or $[010]_{Bi} \| [010]_{Graphite}$ where minimum lattice misfit and angular distortion exist [43].

In order to study the size distribution of Bi nanocrystals, the major and minor axes of the formed nanocrystals were measured from images similar to those of Fig. 5.9. Histograms representing the size distribution of as-deposited and recrystallized nanocrystals were generated. Two distributions accounting for the different crystal shapes were generated for as-deposited films; one for elongated and the other for rounded polyhedrons. For recrystallized films only one distribution is generated. Analysis of images taken at different locations on the surface showed that the size distribution is sensitive to the location selection for low thicknesses, 1.5 ML to 10 ML, while insignificant dependence on location was found for films with large thickness. The random nature of substrate terrace density upon cleavage contributes to this location dep endence of the nanocrystal size distribution. Similar observation was reported previously in the deposition of metallic nanocrystals on a cleaved graphite substrate [28]. Nanocrystals that are away from terrace edges are normally larger in size. Figure 5.10 shows AFM images and analysis of crystalline size distribution of as-deposited and recrystallized 1.5 ML and 33 ML films. A Gaussian function-fit of the distributions, rather than histograms, are plotted in Fig. 5.10(a) and (b) for 1.5 and 33 ML respectively. The distributions became wider and shifted toward higher values as the coverage increased from 1.5 ML to 33 ML. For recrystallized rounded crystals, the full width at
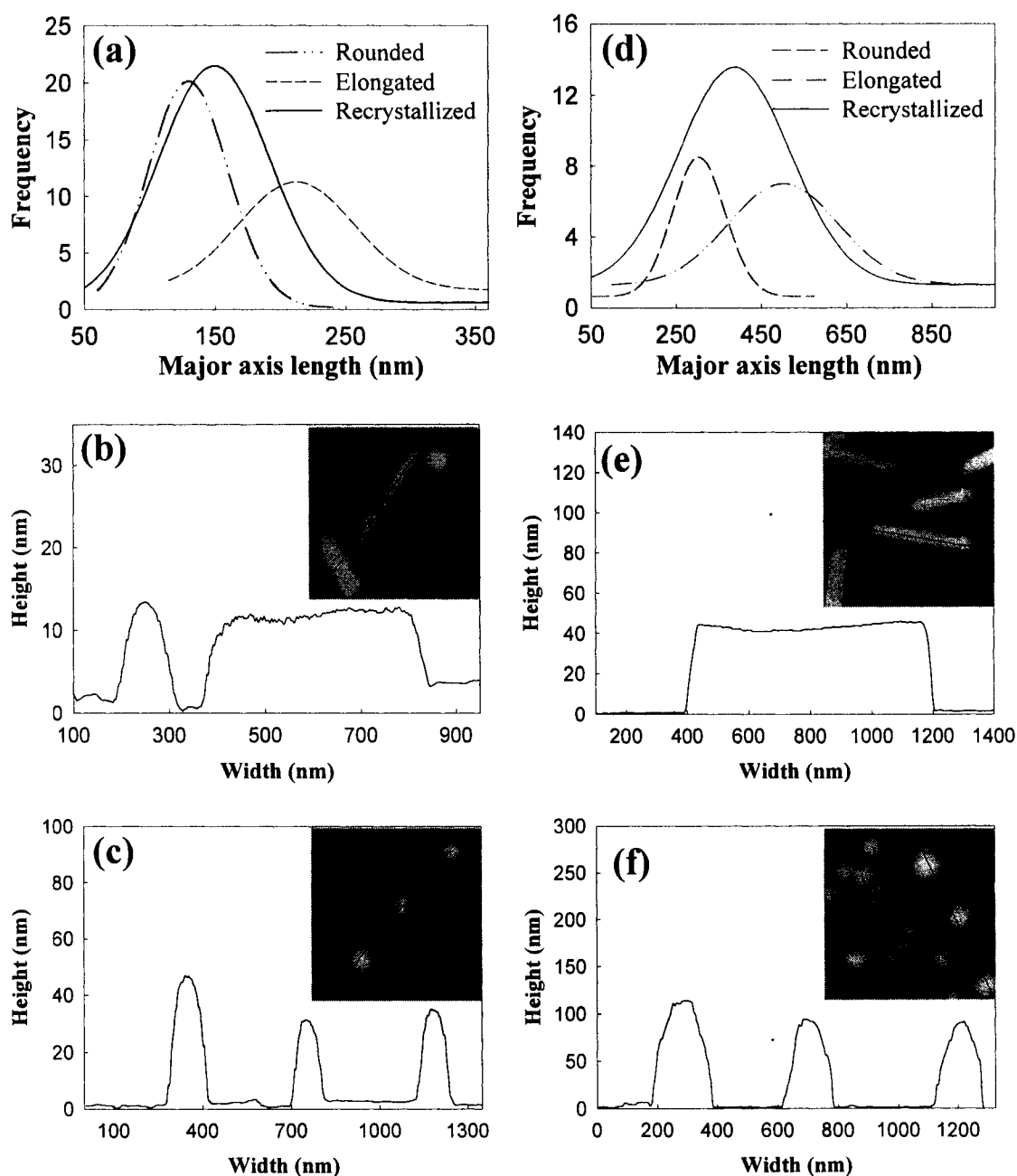
FIG.5.10. Some of the analysis performed on the obtained AFM images of as-deposited and recrystallized Bi films. Gaussian function fits of the size-distribution histograms of as-deposited and recrystallized Bi film of (a) 1.5 ML, and (b) 33 ML mean thickness. AFM line profile analysis along some nanocrystals of Bi films with different mean thickness; (c) as-deposited 1.5 ML, (d) as-deposited 33 ML, (e) recrystallized 1.5 ML, and (f) recrystallized 33 ML.

half maximum (FWHM) of the distributions increased from 102 nm to 333 nm, and the most probable value increased from 150 nm to 388 nm as the thickness increased from 1.5 ML to 33 ML. Similar behavior was observed for as-deposited films where both elongated and rounded distribution are widened and shifted to higher values. Due to shape deformation upon recrystallization, rounded nanocrystals were found to have larger average heights than as-deposited elongated. For 1.5 ML film, Fig. 5.10(c,e), the height increases from ~ 10 nm to ~20 nm, while for 33 ML it increased from ~ 40 nm to > 80 nm as the films recrystallized after melting.

V.3.2. Melting and solidification of Bi nanocrystals

V.3.2.1. Melting of Bi nanocrystals

Melting and solidification of as-deposited and recrystallized Bi films was studied by monitoring the intensity of the Bi (220) spot as a function of temperature. The intensity is normalized to its value at or near room temperature. Figure 15.11 shows the natural log of the normalized intensity as a function of temperature during heating and cooling of as-deposited films with different coverage. Similar curves were obtained for recrystallized films. With heating, the measured RHEED spot intensities decrease due to thermal effects according to the Debye-Waller factor. At some temperature, a sharper intensity decrease occurred due to decrease in the long-range order of the probed nanocrystals. The decrease in the RHEED intensity due to film partial melting is gradual and spans over a temperature range whose onset and end points increase with film thickness. As the film melted completely, the RHEED intensity decreased to its minimum value and only the inelastic scattering background remained. Recrystallized Bi films showed melting behaviors similar to that observed for as-deposited films but shifted

toward higher temperatures. This is due to the shift of the size distribution towards higher

sizes as the nanocrystals recrystallized after melting.
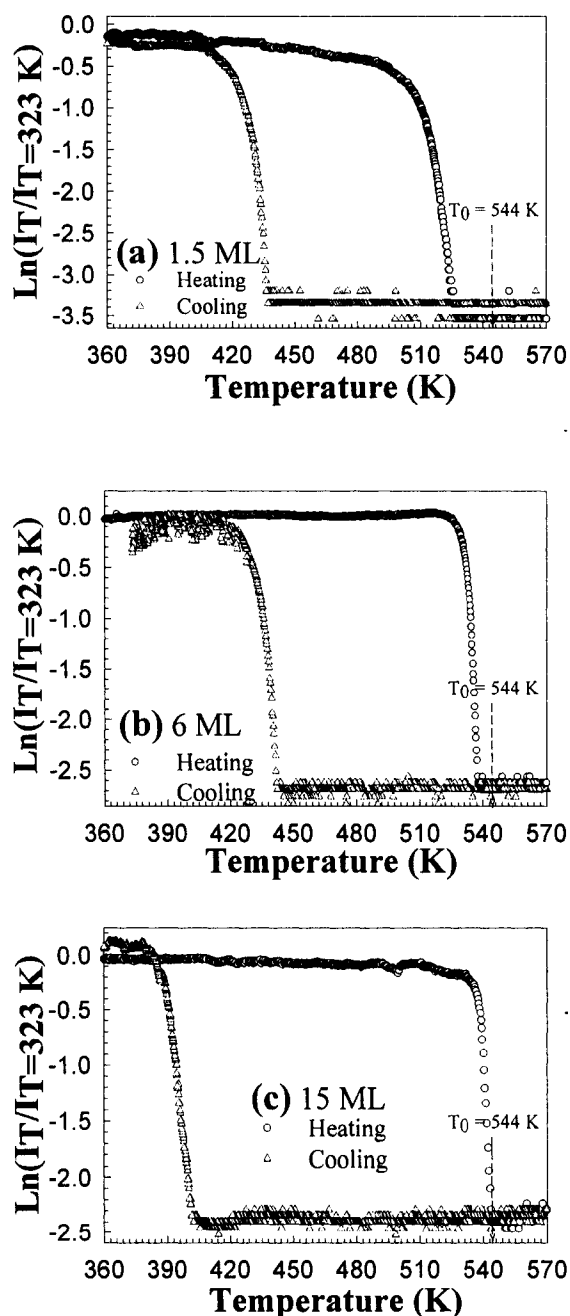
Fig. 5.11. Logarithm of normalized intensity of the RHEED (002) spot of Bi as a function of temperature during heating and cooling of as-deposited Bi films with different mean thickness. Melting point depression and amount of supercooling that varies with the film mean thickness is observed.

RHEED gives a statistical view of order over a large area within a penetration depth given by the IMFP of RHEED electrons in Bi. Thus, one would use the melting range over which the phase transition occurs to study the melting behavior of the nanocrystals making up the films. After taking into consideration the reduction in RHEED intensity due to Debye-Waller factor and inelastic scattering, the intensity decrease of electron diffraction into the (220) spot of Bi is related to the fraction of the solid nanocrystals that are melted within the penetrated depth of the probed area. Following a procedure used to calculate the melted ratio, R, for indium films, R is calculated for as-deposited and recrystallized Bi nanocrystals and plotted in Fig. 5.12 as a function of temperature for films with different thicknesses. Gradual changes in the melting ratio with temperature were observed. Melting of the nanocrystals making up the films occurred within a range of 10 - 20 K. All films started to melt at temperatures below T_0, e.g., T_0-50 K for as-deposited 1.5-ML film. A 5 - 15 K shift in the onset of the melting toward higher values was observed for recrystallized Bi films of same coverage. At the beginning of the melting range, the melting ratios of as-deposited Bi films, Fig 5.12(a), increased slowly with temperature. A much faster melting rate with temperature was observed as the temperature approaches the film maximum melting point. This melting behavior is similar to that reported for surface melting where the quasi-liquid layer thickness grows first as logarithmic function and then diverges as a power function of $(T - T_0)$ as T_0 is approached for bulk singe crystals [71]. For nanocrystals, formation of a surface liquid layer is accompanied by complete melting of smaller sized crystals [72]. The size distribution and the shape of nanocrystals are expected to play a major role in this melting behavior. For crystallites with similar shape, nanocrystals in the lower part

of the size distribution are expected to melt at a lower temperature than those in the higher part. The film melted ratio of recrystallized Bi films, Fig. 5.12(b), showed a similar behavior, but with the melting range shifted toward higher temperatures. Also, for higher thickness, *e.g.* 15 ML, the melting occurs at a narrower melting range. This is mainly due to the shift of the size distribution towards higher values as the nanocrystals recrystallized after melting.

The melting behavior of the nanocrystals making up the films is further investigated by performing profile analysis of the obtained diffraction patterns. In general, the profile of the diffraction spots is related to the shape and size of the diffracting feature. Broadening of diffraction spots, after subtracting the instrumental response, is inversely proportional to the average crystalline size in the probed region. The probed region in this case is the shell surrounding each probed nanocrystal with ~ 9 nm thickness. The instrumental response was obtained by deflecting the electron beam away from the sample so that it directly hits the phosphor screen. The shape of the electron beam, on the phosphor screen, was recorded by the CCD camera. The FWHM of this transmitted beam in Å^{-1}, was used as the instrumental response and was subtracting from the FWHM of the diffraction (220) spot, obtained at different mean film thickness. From the broadening of the (220) spot, diffraction feature size of ~ 4-7 nm is obtained, which is much less than the average nanocrystal size obtained by AFM. This is expected from a transmission RHEED pattern probing the outer shell of the nanocrystals.

Figure 5.13 shows the measured FWHM of the Bi (220) spot in direction parallel and normal to that of the beam for as-deposited and recrystallized Bi films with different mean thicknesses as a function of temperature. The FWHM remains almost constant over
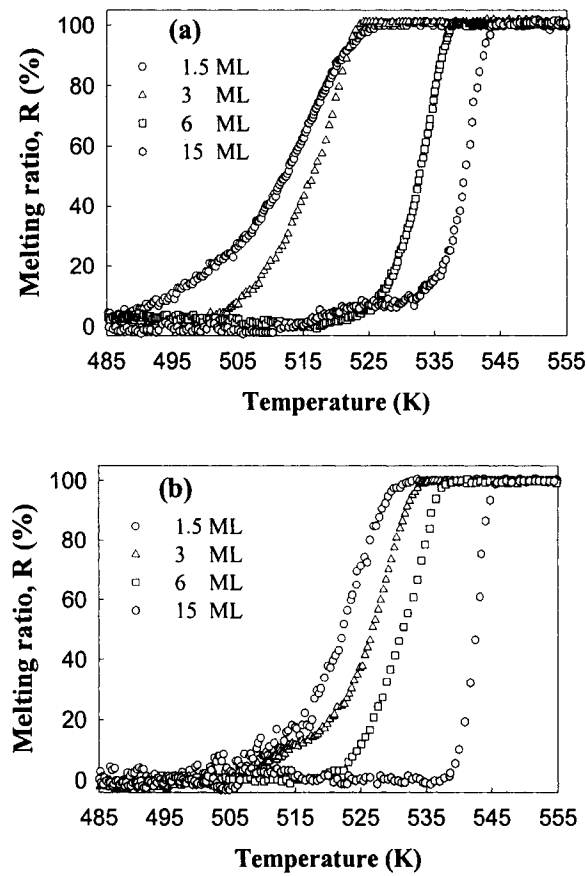
FIG. 5.12. Estimated film melted ratio as a function of temperature at the phase transition region for (a) as-deposited, and (b) recrystallized Bi films with different mean thickness.

a wide temperature range in both the normal and the parallel directions. However, in the film melting range, the FWHM in both directions decreases with temperature, and then starts to increase as the maximum melting point of the film is approached. This behavior is clearly observed for as-deposited and recrystallized 1.5 ML Bi films. The initial decrease in FWHM of the (220) spot in both directions indicates that there is an increase in the average crystalline size within the penetrated depth of the probed area. This average size increase might be due to coalescence of Bi nanocrystals near melting,

Ostwald ripening, and/or crystal shape modification as observed in the AFM of Figs 3. However, this does not explain the observed decrease in the FWHM of recrystallized films where no further significant shape and size changes is expected. Also, no increase in the normalized intensity is observed anywhere within the film melting range, which indicates that there is no significant crystalline enhancement during heating and the size increase occurs only by coalescence of liquid droplet after film melting. Thus, it appears that nanocrystals with small sizes are homogenously melted at lower temperatures resulting in an average sizes increase. The observed increase in the FWHM at the end of the melting range indicates a decrease in the detected average crystal size. This decrease is consistent with the formation of a liquid skin covering the larger nanocrystals, thus, reducing the detected average crystalline size of the probed area of the films.

All films with average thickness up to 15 ML showed FWHM trends similar to that observed for 1.5 ML. However, recrystallized films showed a decrease in the FWHM without significant increase till the end of the film melting range for both normal and parallel directions. AFM image of these films, 3 ML to 15 ML, showed nearly polyhedral shaped nanocrystals with a size distribution shifted toward higher values. While the average crystal size of recrystallized 1.5-ML film is found to be 40 nm that of 3-, 6- and 15 ML films were found to be 57, 83, and 100 nm, respectively. Also, as the coverage increased, the size distribution widened. The nanocrystal at the lower part of the distribution are expected to melt homogenously at a temperature in the lower part of the melting range. As the temperature is raised into the melting range, a subset of the larger nanocrystals becomes covered by a liquid skin layer. Because of the size-dependent liquid skin formation, the liquid layer is formed on the surfaces of larger nanocrystals at
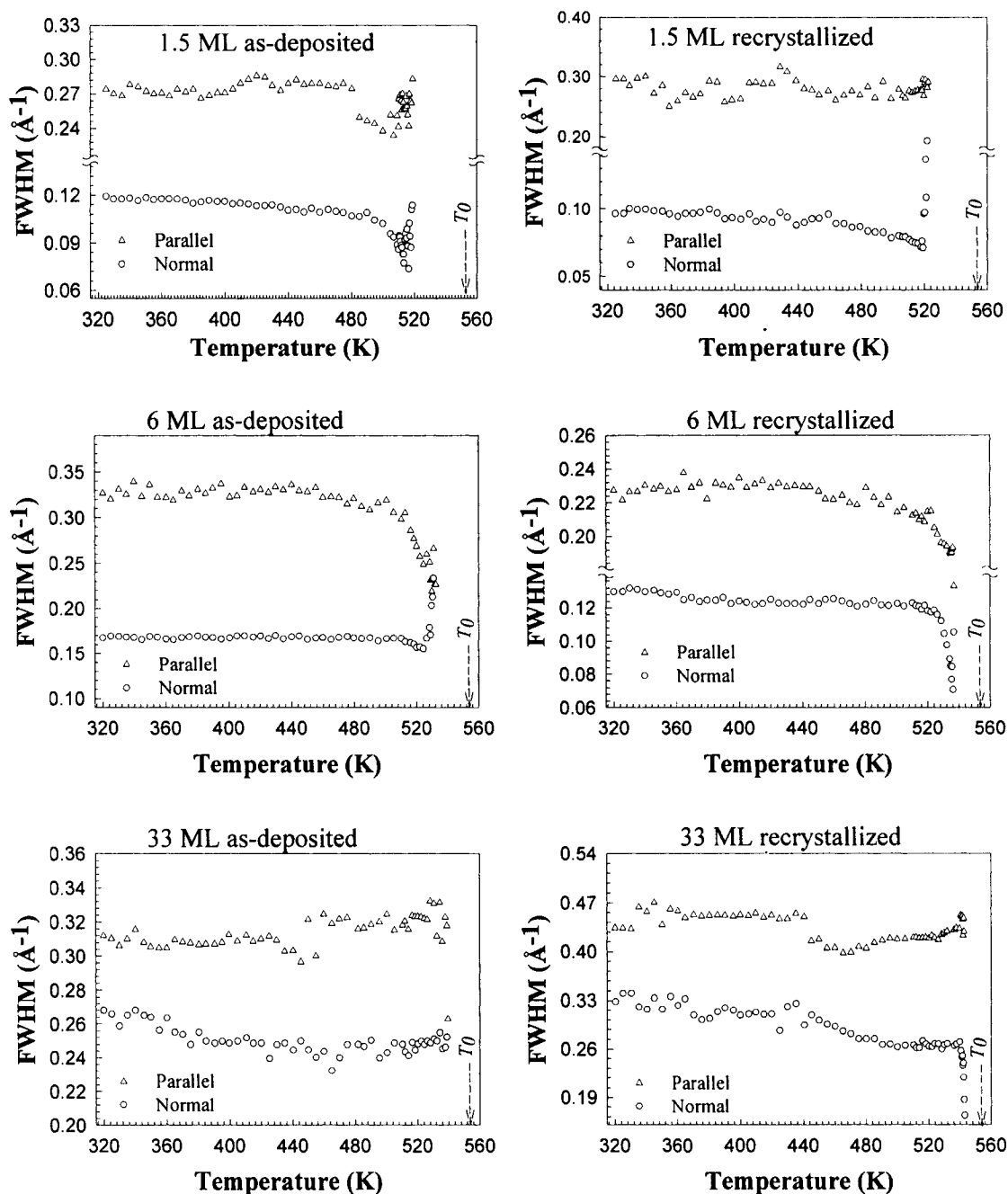
FIG. 5.13. The FWHM of the RHEED (002) spot for as-deposited and recrystallized Bi films with different mean thickness as a function of temperature in a direction parallel and normal to the beam direction. The instrumental response, which is measured to be ~ 0.12 Å^{-1} and 0.17 Å^{-1} for parallel and normal directions, respectively, is subtracted from the plotted values.

higher temperatures relative to those with smaller sizes. With the increase in temperature, more nanocrystals completely melt with the thickness of the liquid shell on the remaining crystals continue to grow with no detectable reduction in the average probed size. This could be due to the compensation of the average crystallite size increase due to melting of small crystals with the decrease due to liquid layer formation on larger ones. Another consideration is the inelastic and linear effects of RHEED electrons, which is expected to increase as a big portion of the nanocrystals of the film turned into liquid. The increase in the liquid formation not only increases such effects but also introduce an uncertainty in the measured FWHM.

The FWHM of as-deposited 33 ML remain constant up to the film complete melting in both parallel and normal directions, while it decreases without significant increase for recrystallized film. This observation shows the effect of crystal shape and size distribution on the melting behavior of the nanocrystals. While as-deposited film have nanocrystals with different shapes, recrystallized nanocrystals have rounded shapes but higher average sizes. Thus, melting of as-deposited either occurred abruptly, due to surface facets, or the melting proceeds via simultaneous melting of small crystals and formation of a liquid layer on the top of larger ones with no detectable change in the FWHM. On the other hand, rounded nanocrystals of recrystallized film melt gradually according to their sizes with a continuous decrease in the measured FWHM.

Within the investigated thickness range, all films melted completely below or at T_0 of Bi. AFM images showed that as-deposited films contain nanocrystals of round, triangular, and platelet shapes. No subset of the grown crystallites could be superheated. For rounded polyhedral Bi nanocrystals, the observed melting point depression was found

to be similar to that previously reported using dark field electron microscopy [18]. Elongated Bi crystallites in the as-deposited films melted at temperatures lower than that for the recrystallized round nanocrystals. In Ref. [18], however, polyhedral shaped nanocrystals faceted by {111} planes were observed to superheat up to $T_0 + 7$ K. These nanocrystals were formed during heating of Bi films initially deposited at room temperature on an amorphous carbon substrate. In the present study, polyhedral elongated nanocrystals were formed on a heated HOPG substrate. The shape of these nanocrystals was affected by the substrate and Bi grew along directions of minimum lattice mismatch and angle distortion on the HOPG basal plane. Thus, the elongated platelet nanocrystals on the HOPG are not of minimum energy shapes and formed in a more hexagonal elongated shape of ~120° side angels (~60° for the triangle shape). In other words, these crystals are not in the truncated pyramidal shape that completely covered by the {111} facets, however, they are most probable of 110 facets. The absence of long-range order in the amorphous carbon substrate appears to have allowed the formation of a subset of crystallites in an elongated shape with minimum energy facets that hinder surface melting and allow superheating. On the other hand, the long-range order of the HOPG substrate causes the formation of elongated crystallites that are bounded by some higher energy facets that permit surface melting. Even with the side surfaces to be the {111}, melt can nucleate from higher energy faces bounding the crystal such as the top surfaces, which could be either 110 or 010 surfaces based on RHEED, and curved edges. For Pb, only triangular shape nanocrystals with sharp edges were reported to show 2-4 K superheating using transmission electron microscopy [22]. In this work, we observed triangular nanocrystals with sharp and curved edges but with fewer umber. Because RHEED gives a

statistical view of nanocrystals over a large area and the sharp-edges triangular nanocrystals were formed with lower probability, at the current experimental conditions, superheating of these nanocrystals is hard to be detected.

V.3.2.2. Melting point-size dependence

To obtain the rate of film melting with temperature, a curve-fit is made to the melted ratio data in Fig. 5.12 and the derivative of this curve-fit is plotted in Fig. 5.14 for as-deposited and recrystallized films. The peak of this derivative gives the temperature at which the rate of film melting with temperature is the fastest, T_{fm}. We use T_{fm} to represent the characteristic film melting temperature, with a range that we define to correspond to 10% and 90% of the melted ratio in Fig. 5.12. Melting point depression that depends on the film mean thickness is clearly observed in Fig. 5.14. Also, recrystallized films showed higher T_{fm} than as-deposited for all films. This is mainly due to the average size increase. From the AFM images of as-deposited and recrystallized films, we calculated a shape-independent average crystal radius, $r_{av} = \left((3 \times Area \times height)/(4\pi) \right)^{1/3}$, by measuring the area and the height of the nanocrystals. The values obtained for as-deposited films were lower than that obtained for recrystallized films with equal thickness for all films. This indicates an average crystal size increase as the films recrystallized after melting, thus, recrystallized films melt at higher temperatures.

We used the obtained values of T_{fm} and r_{av} to study the melting point size dependence of Bi films in the light of different phenomenological models discussed previously in section II.2.3. In this context r_{av} is more convenient since all of these models considered a spherical shape particle. The known physical constants of Bi ($T_0 =$
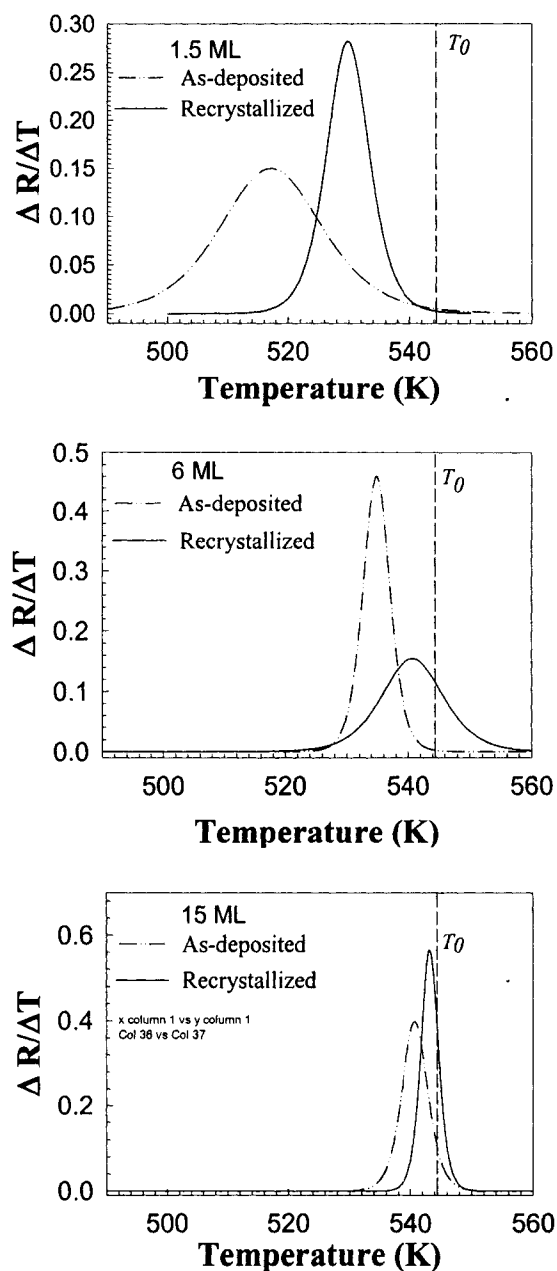
FIG. 5.14. Derivative of the curve-fit to the melted ratio curve in Fig. 5 obtained as a function of temperature for as-deposited and recrystallized Bi films with various mean thickness. The peak of this derivative gives the temperature at which the rate of film melting with temperature is the fastest, T_{fm}.

544.52 K, ρ_s = 9.8 g/cm^3, ρ_l = 10.07 g/cm^3, L = 5.19 × 10^{-8} erg/g, γ_{sl} = 61 erg/cm^2, γ_{sv} = 550 erg/cm^2, γ_{lv} = 375 erg/cm^2, h = 0.4074 nm, S_{vib} = 3.78 J mole^{-1} K^{-1}, R = 8.3142 J mole^{-1} K^{-1}) are used to calculate the melting point size dependence of Bi [7,17,40,41]. Fig. 5.15 shows the size dependent behavior predicted by these models compared to the results obtained from the present work. In calculating the melting point using the NG model, we used the average value of the parameter α_{NG}. Also, we used an arbitrary value of δ = 4 nm in the calculation using the LS model. However, varying this value between 2 nm and 10 nm does not affect the predicted values for particles of radius within the current experimental values, it only affects the melting point of particles with radius close to the value of δ.

The size-dependent phenomenological models have two characteristics in common; T_m converge to T_0 as the radius goes to infinity, and a linear or semi-linear relation exist between T_m and r^{-1} of the particle. Straight lines with different slops are obtained for Bi using these models with LV and HM models showing strong agreement with each other. The melting points calculated by these models converge to T_0 for the larger sizes. Considering the range of nanocrystal sizes we studied, the melting data shows best agreement with the SPI model. While the predicted trend of SPI model fits nicely the data of Bi, it showed a big deviation from that measured for In. A similar conclusion was obtained by the authors of the SPI model in comparing his model with other reported available experimental data for different materials.

——— HM model   – – – LS model   · · · · · NG model   – · – · LI

– · · – SPI model   LV model   ● Current work
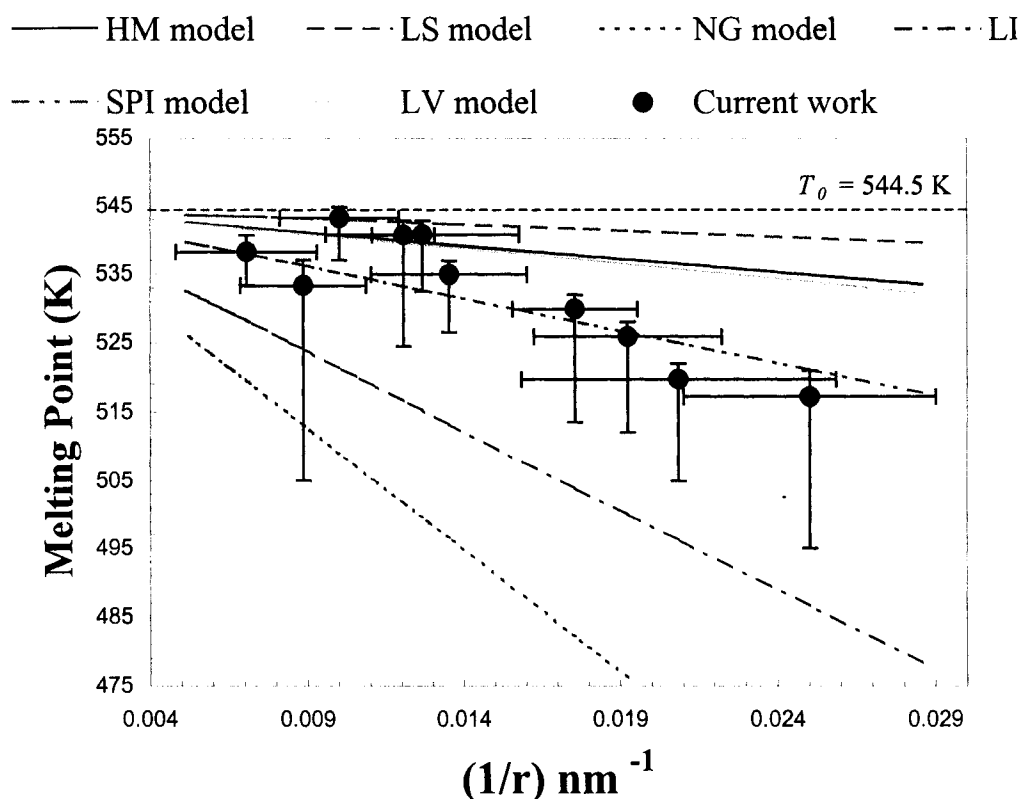
FIG. 5.15. The measured melting point as a function of the reciprocal of the average crystalline size compared to different thermodynamic models. The film melting point T_{fm} is obtained from Fig. 7. The bars represent the melting range as described in the text. The surface phonon instability model agrees best with this experimental result.

V.3.2.1. Solidification of Bi melt

During solidification, the Bi films showed high amount of supercooling relative to the onset of its melting. A wide melting- solidification hysteresis curves that varied with the film average thickness were observed for as-deposited Bi films as shown in Fig. 5.11. In general, supercooling is attributed to the presence of a nucleation barrier for solidification that results from the competition between the decrease in the volume free energy upon solidification and the increase in the free energy associated with the existence of a solid-liquid interface. Classical nucleation theory predicts that

solidification occurs with a lower energy barrier on heterogonous sites than homogenously from within the liquid. The energy barrier for solidification decreases as the liquid is supercooled below its bulk melting point. Furthermore, if the liquid is deeply supercooled, spontaneous solidification can occur with zero energy barriers. For a bulk liquid, this can take place after supercooling amount of ΔT_0. However, for a small droplet, spontaneous solidification starts at a different temperature given by [15],

$$\Delta T_m = \Delta T_0 + \frac{T_0}{\rho L} \cdot \frac{3\alpha \Delta\gamma}{r}, \text{ with } \Delta\gamma = \gamma_{solid / graphite} - \gamma_{liquid / graphite} \quad (5.1)$$

where ΔT_m is the amount of supercooling of a melted particle of radius r, α is the fraction of the liquid/substrate interface that is replaced by the solid/substrate interface after solid nucleation, and $\gamma_{solid / graphite}$ and $\gamma_{liquid / graphite}$ are the specific interfacial energies between the graphite substrate and the solid and liquid bismuth, respectively. The amount of supercooling obtained from as-deposited and recrystallized films is plotted as a function of the calculated shape-independent average crystal size, as shown in Fig 5.16. The obtained supercooling amount ΔT_m fits nicely a straight line with a small negative slop. This indicates a supercooling amount increase as the droplet size increase. From Eq. (5.1), the sign of the slope of the straight line is determined by the sign of $\Delta\gamma$, which means, in our case, that $\Delta\gamma$ is negative i.e. liquid Bi has a higher interfacial energy with graphite substrate than its solid phase. Accordingly, nanocrystals with larger sizes have a higher supercooling amount with maximum supercooling observed for the bulk material, which is found from the curve intercept to be 126 K.
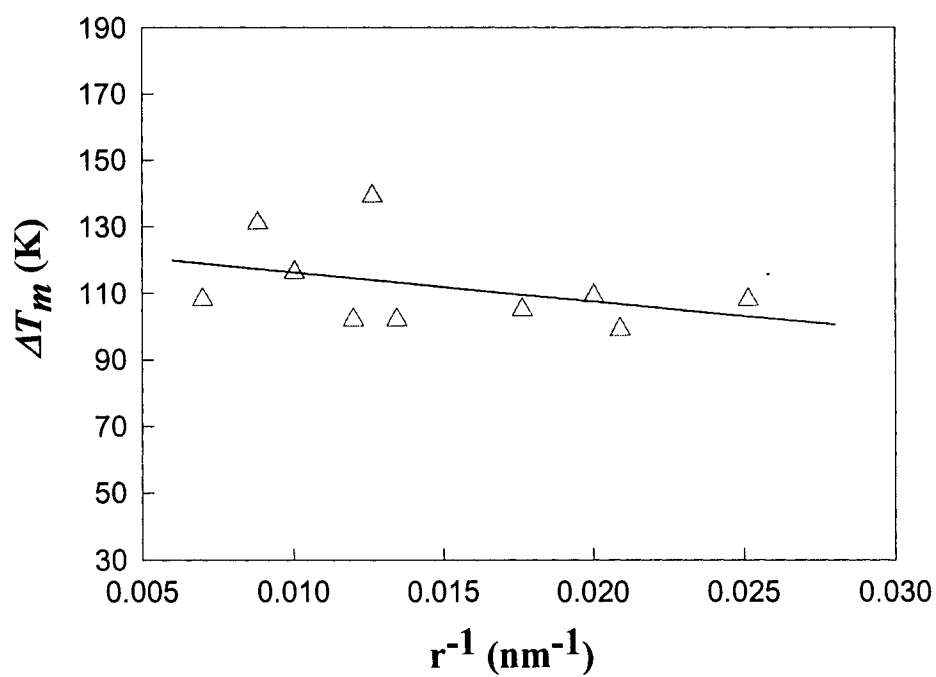
FIG. 5.16. The measured amount of supercooling as a function of the reciprocal of the average crystalline size. Straight line with negative slope indicating a liquid substrate interaction to be higher than that between the solid and the substrate, best fit the result.

V.4.   References for chapter V

[1]   R. S. Berry, "Melting and freezing phenomena", Microscale Thermophys. Eng. 1, 1-18 (1997).

[2]   K. Lu and Z. H. Jin, "Melting and superheating of low-dimensional materials," Curr. Opin. Solid State Mater. Sci. 5, 39-44 (2001).

[3]   Y. Qi, T. Cagin, W. L. Johnson, and W. A. Goddard III, "Melting and crystallization in Ni nanoclusters: The mesoscale regime," J. Chem. Phys. 115,385-394 (2001).

[4]   M. L. Lavčević and Z. Ogorelec, "Melting and solidification of Sn-clusters," Mater. Lett. 57, 4134-4139 (2003).

[5]   L. J. Lewis, P. Jensen, and J. Barrat, "Melting, freezing, and coalescence of gold nanoclusters," Phys. Rev. B 56, 2248-2257 (1997).

[6]   F. Ercolessi, W. Andreoni, and E. Tosatti, "Melting of small gold particles: Mechanisms and size effects," Phys. Rev. Lett. 66, 911-914 (1991).

[7]   G. L. Allen, R. A. Bayless, W. W. Gile, and W. A. Jesser, "Small particle melting of pure metals," Thin Solid Films 144, 297-308 (1986).

[8]   Ph. Buffat and J.-P. Borel, "Size effect on the melting temperature of gold particles," Phys. Rev. A 13, 2287-2298 (1976).

[9]   T. Castro, R. Reifenberger, E. Choi, and R. P. Andres, "Size-dependent melting temperature of individual nanometer sized clusters," Phys. Rev. B 42, 8548-8556 (1990).

[10]   M. Zhang, M. Yu. Efremov, F. Schiettekatte, E. A. Olson, A. T. Kwan, S. L. Li, T. Wisleder, J. E. Greene, and L. H. Allen, "Size-dependent melting point

depression of nanostructures: Nanocalorimetric measurements," Phys. Rev. B **62**, 10548-10557 (2000).

[11]   L. Zhang, Z. H. Jin, L. H. Zhang, M. L. Sui, and K. Lu, " Superheating of confined Pb thin films," Phys. Rev. Lett. **85**, 1484-1487 (2000).

[12]   N. T. Gladkikh, S. I. Bogatyrenko, A. P. Kryshtal, and R. Anton, "Melting point lowering of thin metal films (Me = In, Sn, Bi, Pb) in Al/Me/Al film system," Appl. Surf. Sci. **219**, 338–346 (2003).

[13]   N. B. Thoftt, J. Bohrf, B. Burast, E. Johnsons, A. Johansens, H. H. Andersens, and L. Sarholt-Kristensens, "Melting and solidification of Bi inclusions in aluminium," J. Phys. D: Appl. Phys. **28**, 539-548 (1995).

[14]   H. H. Andersen and E. Johnson, "Structure, morphology and melting hysteresis of ion implanted nanocrystals," Nucl. Instrum. Methods Phys. Res. Sect. B: Beam Interact. Mater **106**, 480-491 (1995).

[15]   H. W. Sheng, K. Lu, and E. Ma, "Melting and Freezing behavior of embedded nanoparticles in ball-milled Al ±10 wt % M (M = In, Sn, Bi, Cd, Pb) mixtures," Acta Mater. **46**, 5195-5205 (1998).

[16]   J. D. Mackenzie and R. L. Cormia, " Melting of gallium and Bi," J. Chem. Phys. 39, 250-250 (1963).

[17]   J. F. van der Veen, B. Pluis, and A. W. D. van der Gon, in *Chemistry and Physics of Solid Surfaces VII*, Springer-Veilag, pp. 455-490 (1988).

[18]   S. J. Peppiatt, "The melting of small particles. II. Bi," Proc. R. Soc. Lond. A **345**, 401-412 (1975).

[19] M. Blackman, S. J. Peppiatt, and J. R. Samples, "Superheating of Bi," Nat. Phys. Sci. **239**, 61-62 (1972).

[20] V. P. Skripov, V. P. Koverda, and V. N. Skokov, ' Size effect on melting of small particles," Phys. Stat. Sol. A **66**, 109-118 (1981).

[21] M. Takagi, "Electron diffraction study of liquid-solid transition of thin metal films," J. Phys. Soc. Japan **9**, 359-363 (1954).

[22] J. J. Mètois and J. C. Heyraud, "The overheating of lead crystal," J. Phys. (France) **50**, 3175-3179 (1989).

[23] G. D. T. Spiller, "Time-dependent melting and superheating of lead crystallites," Phil. Mag. A **46**, 535-549 (1982).

[24] A. A. Shvartsburg and M. F. Jerrold, "Solid cluster above the bulk melting point," Phys. Rev. Lett. **85**, 2530-2532 (2000).

[25] Z. H. Zhang, P. Kulatunga, and H. E. Elsayed-Ali, "Reflection high-energy electron-diffraction study of melting and solidification of Pb on graphite," Phys. Rev. B **56**, 4141-4148 (1997).

[26] H. Lwasaki, J. H. Chen, and T. Kikegawa, "Structural study of the high-pressure synchrotron radiation phases of bismuth using high-energy," Rev. Sci. Instrum. **66**, 1388 (1995).

[27] E. Haro-Poniatowski, R. Serna, C. N. Afonso, M. Jouanne, J. F. Morhange, P. Bosch, and V. H. Lara, "Hysteresis in the melting kinetics of Bi nanoparticles" Thin Solid films 453-454, 467 (2004).

[28]   X. F. Yu, X. Liu, K. Zhang, and Z. Q. Hu, "The lattice contraction of nanometre-sized Sn and Bi particles produced by an electrohydrodynamic technique," J. Phys.: Condens. Matter. **11**, 937 (1999).

[29]   L. H. Liang, J. C. Li, and Q. Jiang, "Size-dependent melting depression and lattice contraction of Bi nanocrystals," Physica B **334**, 49-53 (2003).

[30]   M. M. Rosario and Y. Liu, "Electrical transport studies of quench condensed Bi films at the initial stage of film growth: A structural transition and the possible formation of electron droplets," Phys. Rev. B **65**, 094506 (2002).

[31]   M. G. Mitch, S. J. Chase, J. Fortner, R. Q. Yu, and J. S. Lannin, "Phase transition in ultrathin Bi films," Phys. Rev. Lett. **67**, 875 (1991).

[32]   J. P. Heremans, C. M. Thrush, D. T. Morelli, and M.-C. Wu, "Thermoelectric power of bismuth nanocomposites," Phys. Rev. Lett. **88**, 216801 (2002).

[33]   T. Hamadat, K. Yamakawa, and F. E. Fujita, "Superconductivity of vacuum-deposited bismuth films," J. Phys. F: Metal. Phys. **11**, 657 (1981).

[34]   K. Liu, C. L. Chien, and P. C. Searson, "Finite-size effects in bismuth nanowires," Phys. Rev. B **58**, R14681 (1998).

[35]   F. Y. Yang, K. Liu, K. Hong, D. H. Reich, P. C. Searson, and C. L. Chien, "Large magnetoresistance of electrodeposited single-crystal bismuth thin films," Science **421**, 1335 (1999).

[36]   A. Martinez, R. Collazo, A. R. Berrios, and G. O. Ducoudray, "Growth and characterization of bismuth and antimony thin films," J. Crys. Growth **174**, 845 (1997).

[37]   S. Jiang, Y.-H. Huang, F. Luo, N. Du, and C.-H. Yan, "Synthesis of bismuth with various morphologies by electrodeposition," Inorganic Chem. Comm. **6**, 781 (2003).

[38]   Y. Namba and T. Mori, "Cross-sectional structure of Bi films and its phenomenological analysis," J. Appl. Phys. **46**, 1159 (1974).

[39]   D. L. Partin, J. Heremans, D. T. Morelli, C. M. Thruch, C. H. Olk, and T. A. Perry, "Growth and characterization of epitaxial bismuth films," Phys. Rev. B. **38**, 3818 (1988).

[40]   A. Dauscher, A. Jacquot, and B. Lenior, "Temperature dependent growth of pulsed laser deposited Bi films on BaF2(111)," Appl. Surf. Sci. **186**, 513 (2002).

[41]   J. Jing, P. N. Henriksen, H. T. Chu, and H. Wang, "Epitaxial growth of ultrathin films of bismuth: An atomic force microscope study," Appl. Surf. Sci. **62**, 105 (1992).

[42]   D. L. Partin, C. M. Thruch, J. Heremans, D. T. Morelli, and C. H. Olk, "Growth and characterization of epitaxial bismuth films" J. Vac. Sci. Technol. B **7**, 348 (1989).

[43]   H. Wang, J. Jing, and P. N. Henriksen, "Onset of crystal growth of bismuth on graphite: An atomic force microscopy study," J. Vac. Sci. Technol. A **11**, 1987 (1993).

[44]   J. C. Heyraud and J. J. Mètois, "Equilibrium shape and temperature: Lead on graphite," Surf. Sci. **128**, 334-342 (1983).

[45]   J. C. Heyraud and J. J. Mètois, "Surface free energy anisotropy measurement of indium," Surf. Sci. **177**, 213-220 (1986).

[46]   Y. Shigeta and Y. Fukaya, "Structural phase transition and thermal vibration of surface atoms studied by reflection high-energy electron diffraction," Appl. Surf. Sci. **237**, 21 (2004).

[47]   K. Theis-Bröhl, I. Zoller, P. Bödeker, T. Schmitte, H. Zabel, L. Brendel, M. Belzer, and D. E. Wolf, "Temperature and rate-dependent RHEED oscillation studies of epitaxial Fe(001)on Cr (001)," Phys. Rev. B **57**, 4747 (1998).

[48]   H. Wang, J. Jing, R. R. Mallik, H. T. Chu, and P. N. Henriksen, "Crystallographic structure and defects in epitaxial bismuth films grown on mica," J. Cryst. Growth **130**, 571 (1993).

[49]   A. Dauscher, M.O. Boffouè, B. Lenoir, R. Martin-Lopez, and H. Scherrer, "Unusual growth of pulsed laser deposited bismuth films on Si(100)," Appl. Surf. Sci. **138-139**, 188 (1999).

[50]   D. J. Bottomley, M. Iwami, Y. Uehara, and S. Ushioda, "Evidence for liquid indium nanoparticles on Ge(001) at room temperature," J. Vac. Sci. Technol. B **17**, 12 (1999).

[51]   T. Inuzuka and R. Ueda, "Continuous observation of initial growth and coalescence of bismuth deposits by in situ electron microscopy," J. Vac. Sci. Technol. **6**, 379 (1968).

[52]   K. K. Nanda, S. N. Sahu, and S. N. Behera, "Liquid-drop model for size dependent melting of low dimensional systems," Phys. Rev. A **66**, 013208 (2002).

[53]   H. Reiss, P. Mirable, and R. L. Whetten, "Capillarity theory for the coexistence of liquid and solid clusters," J. Phys. Chem. **92**, 7241-7246 (1998).

[54]   M. Wautelet, "Estimation of the variation of the melting temperature with the size of small particles on the bases of a surface-phonon instability model," J. Phys. D: Appl. Phys. **24**, 343-346 (1991).

[55]   M. Akyurt, G. Zaki, and B. Habeebullah, "Freezing phenomena in ice-water systems," Energy Conversion and Management **43**, 1773 (2002).

[56]   S. V. Dukarov, "Size and temperature effects on wetting in supercooled vacuum condensates," Thin Solid Films **323**, 136 (1998).

[57]   K. Mae, V. V. Moshchalkov, and Y. Bruynseraede, " Intensity profiles along the RHEED streaks for various thin film surface morphologies," Thin Solid Films **340**, 145-152 (1999).

[58]   H. J. Koh, P. Rudolph, N. Schäfer, K. Umetsu, and T. Fukada, "The effect of various thermal treatment on supercooling of PbTe melts," Mat. Sci. Eng. B 34, 199 (1995).

[59]   Z. Zhou, W. Wang, and L. Sun, "Undercooling and metastable phase formation in a $Bi_{95}Sb_5$ melt," Appl. Phys. A **71**, 261 (2000).

[60]   V. D. Aleksandrov and S. A. Frolova, "Supercooling of In_2Bi and InBi melts," Inorganic Mat. **40**, 227 (2004).

[61]   T. Schenk, D. Holland-Moritz, V. V. Simonet, R. Bellissent, and D. M. Herlach, "Icosahedral short-range order in deeply undercooled metallic melts," Phys Rev. Lett. **89**, 075507(2002).

[62]   J. Kritzer, A. Deaconescu, J. de la Parra, Jr., D. F. Coluccio, S. Mikhail, K. Demuren and R.Q. Topper, "Benchmarking potential energy models against bulk properties for simulations of bismuth clusters," Internet J. Chem. **3**, 12 (2000).

[63]   V. I. Merkulov and J. S. Lannin, "Variations in atomic structure of liquid bismuth clusters," Phys. Rev. B **58**, 7373 (1998).

[64]   O. Chamberlian, "Neutron diffraction in liquid sulfur, lead, and bismuth," Phys. Rev. **77**, 305 (1950).

[65]   J. C. Patrin, Y. Z. Li, M. Chander, and J. H. Weaver, "Bi thin film growth structures prepared at 30 K on GaAs(110) and InP(110)," J. Vac. Sci. Technol. A **11**, 2078-2083 (1993).

[66]   M. Mašek, V. Matolín, "RHEED study of Nb thin film growth on Cu(111) and (100) single crystals," Vacuum 61, 217-221 (2001).

[67]   S. Andrieu and P. Frechard, "What information can be obtained by RHEED applied on polycrystalline films?" Surf. Sci. **360**, 289-296 (1996).

[68]   C. J. Powell, A. Jablonski, I. S. Tilinin, S. Tanuma, and D. R. Penn, "Surface sensitivity of Auger-electron spectroscopy and X-ray photoelectron spectroscopy," J. Electron Spectrosc. Relat. Phenom. **98–99**, 1–15 (1999).

[69]   Z. Wang and P. Wynblatt, "The equilibrium form of pure gold crystals," Surf. Sci. **398** 259-266 (1998).

[70]   J. C. Patrin, Y. Z. Li, M. Chander, and J. H. Weaver, "Bi thin film growth structures prepared at 30 K on GaAs(110) and InP(110)," J. Vac. Sci. Technol. A **11**, 2078-2083 (1993).

[71]   B. Pluis, T. N. Taylor, D. Frenkel,and J. F. Van der Veen, "Role of the long-range order in the melting of metallic surfaces," Phys. Rev. B **40**, 1353-1356 (1998).

[72]   K. F. Peters, Y.-W. Chung, and J. B. Cohen, "Surface melting on small particles," Appl. Phys. Lett. 71, 2391-2393 (1997).

CHAPTER VI

SUMMARY

Melting and solidification of as-deposited and recrystallized indium and bismuth nanocrystals were studied using RHEED. The nanocrystals were thermally deposited on highly oriented 002-graphite substrate at different deposition temperatures. The growth dynamics of the nanocrystals was studied using *in situ* RHEED, while the morphology and size distributions were studied using *ex situ* real image technique (AFM or SEM). The intensity change of RHEED diffraction pattern with temperature was used to probe the melting and solidification of the nanocrystals. Some of the main results obtained in this work are summarized below.

For indium, RHEED observation during deposition showed that 3D nanocrystals are directly formed from the vapor phase at all the studied deposition temperatures, 300 K up to 25 K below the bulk melting point of indium. Post deposition AFM showed that as-deposited films were composed of shallow 3D nanocrystals with different shapes having top flat surfaces, while the recrystallized nanocrystals form well faceted relatively high 3D crystals, polyhedral shaped, with curved edges, and curved top surfaces. As-deposited nanocrystals showed an increase in the (00) RHEED intensity due to annealing as they were heating before melting. No intensity increase before melting was detected for the recrystallized films; only the expected intensity decrease due to the increased lattice vibration and melting was observed. Both as-deposited and recrystallized indium nanocrystals showed melting point depression that extends over a temperature range due to their size distribution. Nanocrystal size and shape determine its melting behavior. Because of the formation of low external energy faceted nanocrystals, the as-deposited 3-

ML film show higher-end melting point than the 10-ML film in spite of the lower average crystal size for the 3-ML film. For recrystallized nanocrystals, the absence of any abnormal crystal morphology, with the nanocrystals formed in their equilibrium shape, explains the observed melting point depression. The deposition temperature is found to have a significant effect on the end melting point of the as-deposited nanocrystals, while it has a negligible effect on the end melting point of the recrystallized films. Within the experimental error, as-deposited films, grown at room temperature, show an end melting point nearly equal to that of the recrystallized films except for the 1.5-ML film where the as-deposited film shows an end melting point ~10 K lower than the recrystallized film. The measured melting point of indium nanocrystals is found to depend linearly on the reciprocal of its average crystal size, in agreement with different thermodynamic models. The diffraction intensity and line shape analysis favor the liquid skin model of nanocrystal melting. Upon cooling below the bulk melting temperature, films with mean thickness $\geq$ 6 ML show about constant amount of supercooling, while films with lower mean thickness show an amount of supercooling that decreases with mean thickness.

For bismuth, RHEED observation during deposition showed two deposition regimes; low temperature solid film deposition and high temperature liquid phase condensation. A substrate temperature of 415±5 K was found to be the boundary between these two regimes. Films deposited at temperatures below 415±5 K showed transmission RHEED patterns corresponding to the Bi structure at an average thickness as low as ~ 0.5 ML, indicating direct solid film formation. The continuous decay of the graphite (00) spot intensity indicated 3D Bi island formation. AFM analysis showed that these films were composed of 3D multilayer triangular step-pyramid shaped crystallites. This

crystallite shape supports the conclusion of direct solid Bi crystallites growth from the vapor phase in a 2D layer-by-layer-like growth mode. Bi deposited at temperatures higher than 415±5 K condensed into liquid droplets. This result is supported by the observation of diffuse RHEED patterns that are thickness independent. When these films were cooled, clear transmission RHEED patterns appeared in the temperature range between 408 K and 392 K. Moreover, when these films were subsequently heated, the diffuse RHEED patterns appeared only at ~10-15 K below T_0 of Bi, due to surface melting forming a liquid shell surrounding the crystallite. Upon cooling, these Bi crystallites supercooled by ~125 K. Our observations indicate that not only the surface but also the bulk of the deposited Bi films were condensed in a long-lived, relatively stable, supercooled liquid phase. Different size-dependence melting point models support the conclusion that Bi is condensed in a liquid phase for substrate temperatures higher than 415±5 K. As the Bi nuclei grew in size, it solidified when it reached a certain critical size that is dependent on temperature. However, the liquid nuclei would remain in the liquid phase if the films were deposited on substrates with temperatures above the maximum supercooling point. AFM observation of Bi crystallized from a liquid showed that two different crystal shapes are formed based on the deposition temperature. Films deposited in the neighborhood of the solid/liquid condensation temperature boundary, 415±5 K, form crystallites with nonisotropic shapes, while those deposited at higher temperatures form rounded polyhedral crystallites. The different crystallographic shapes observed for these films result from the dependence of crystal morphology on the degree of liquid supercooling. AFM image of films deposited at 425 K showed that both as-deposited and recrystallized films were composed of separate 3D crystallites with

different sizes. Nanocrystals with different shapes including rounded, polyhedral, elongated platelet, and triangular were observed in as-deposited films. Recrystallized nanocrystals were formed in facetted and/or rounded polyhedral similar shapes. The elongated nanocrystals were found to align themselves in the directions of minimum lattice misfit and angular distortion on the 002-graphite plane. The nanocrystals were uniformly distributed throughout the substrate surface except at terrace edges where a higher density of nanocrystals was found. The distributions became wider and shifted toward higher values as the thickness was increased. With heating, the Bi films showed a gradual solid-liquid phase transition. Melting of the nanocrystals making up the films occurred at temperatures lower than T_0 and spanned over a temperature range whose onset and end points increased with the film coverage. Due to size increase after melting, the recrystallized nanocrystals showed a melting range at temperatures higher than that of the as-deposited. Within the investigated thickness range, all the nanocrystal shapes showed size-dependent melting point depression, and the films were melted completely below or at T_0 of Bi. Formation of the elongated platelet crystals due to an epitaxial-like growth mode, rather than minimum energy shape, explains its observed meting point depression. RHEED profile analyses showed that small nanocrystals melt first, while liquid skin formation on the curved surfaces of larger nanocrystals continue to grow in thickness causing a size-dependent melting. The characteristic film melting point of Bi showed a linear dependence on the reciprocal of the average crystal radius, in agreement with different phenomenological theoretical models. However, the surface phonon instability model best fits our data. During solidification, as-deposited and recrystallized Bi nanocrystals showed large supercooling relative to T_0. The amount of liquid

supercooling was found to decrease linearly with the reciprocal of the average crystal size.

Indium has a positive volume change upon melting while bismuth has a negative volume change upon melting. Both nanocrystals showed melting point depression with end melting point below or at the bulk melting point. This nullifies the property change upon melting as an effect on the nanocrystals melting behavior, however, it might explain the large amount of supercooling, 125 K, observed for bismuth and the lower amount, 16 K, observed for indium. The melting point depression observed for indium is consistent with all previous results reported for indium using slow heating. However, bismuth nanocrystals of elongated platelet shapes was reported to show ~7 K superheating above the bulk melting point, which seems contradicting the melting point depression observed in this experiment. Formation of the elongated platelet crystals due to an epitaxial-like growth, rather than minimum energy shape, explains the observed melting point depression in the current work.

APPENDIX A

Interpretation of pure reflection RHEED patterns

For pure reflection RHEED patterns and for a given surface of known orientation, 2D indexing is used. Recalling that RHEED is an image of the surface lattice in the reciprocal space, a pre-calculation of the reciprocal lattice mesh of that surface is needed. These calculations are necessary to determine the direction of the incident electron beam relative to the surface structure. In the case of an unknown crystal surface, calculations are performed for different crystal surfaces until a good match between the experimental and the calculated structure is found. Below is a given example of particular graphite, indium and bismuth surfaces.

A.1. Graphite structure and (0002) surface calculations

Graphite is characterized by its layered structure due to the in-plane strong bonding and weak van der Waals bonding between planes. This mechanism is partially what allows graphitic planes to be easily cleavage. The in-plane structure of graphite consists of long-range order arrangement of fused hexagons of 1.415 Å effective bond length and 120-degree bond angle [1-3]. These homogenous layers of fused hexagons remain almost free from each other with a c-axis average interlayer distance of 3.35 Å and an upper limit distance of around 3.5 Å [1]. Figure A.1(a) shows the graphite structure along the 001 plane. The unit mesh in this plane can be constructed from the basic vectors $\underline{a} = 2.46$ [100], and $\underline{b} = 2.46$ [010] with the [001] vector normal to the page. Taking into consideration that the basic vectors $\underline{a}$ and $\underline{b}$ are not orthogonal (have a 60°), one can resolve $\underline{a}$ into its components in the orthogonal system to be,

$\underline{a} = 2.46$ [cosϕ $\underline{x}$ +sinϕ $\underline{y}$], with $\phi = 30$, while $\underline{b}$ is parallel to the y axis. Therefore, $\underline{a}$ and

$\underline{b}$ can be written as,

$$\underline{a} = 2.13 \, \underline{x} + 1.23 \, \underline{y}$$

$$\underline{b} = 2.46 \, \underline{y}$$

The basic vectors in the reciprocal space can be obtained from those of real space using the following formula,
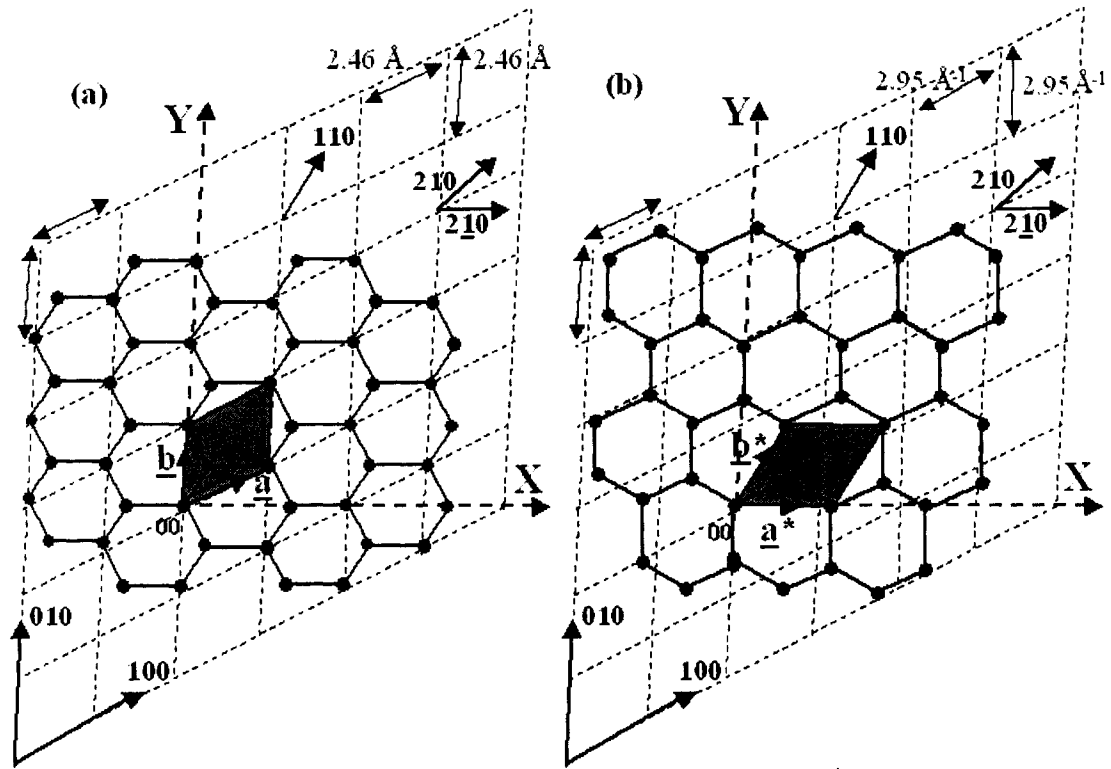
FIG. A.1. The long-range order arrangement of fused hexagons in the in-plane structure of graphite layer with a 2D diamond unit mish in real space (a), and in reciprocal space (b). The vector normal to the page is [0001].

$$\underline{a}^* = 2\pi(\underline{b} \times \underline{n}) \, / \, A,$$
$$\underline{b}^* = 2\pi(\underline{n} \times \underline{a}) \, / \, A,$$
$$(A.1)$$

where, $A = \underline{a} \cdot (\underline{b} \times \underline{n})$ is the area of the unit mesh, which can be calculated as,

$$A = \underline{a} \cdot (\underline{b} \times \underline{n}) = [(2.13 \, \underline{x} + 1.23 \, \underline{y})] \cdot [(2.46 \, \underline{y}) \times (\underline{z})]$$

$$= 5.2398 \text{ Å}^2 \cong 5.24 \text{ Å}^2$$

The primitive reciprocal vectors can then be obtained as,

$$\underline{a}^* = (2\pi/5.24)[(2.46 \, \underline{y}) \times (\underline{z})] = 2.95 \, \underline{x},$$

$$\underline{b}^* = (2\pi/5.24) [(\underline{z}) \times (2.13 \, \underline{x} + 1.23 \, \underline{y})]$$

$$= 1.198 [-1.23 \, \underline{x} - 2.13 \, \underline{y})] = -1.474 \, \underline{x} - 2.551 \, \underline{y}$$

The magnitude is given simply by the square root of the sum of the squares of their components, which gives an equal value of 2.95 A^{-1}. The new direction in the reciprocal space can be inferred from a calculation of the angle that the vectors make with the positive x-axis. In the reciprocal space, $\underline{a}^*$ is in the x-direction indicating a clockwise rotation by 30 degrees angle, while $\underline{b}^*$ makes a 60 degree angle with the positive x-axis indicating a 30-degree angle rotation too. This means that the vectors $\underline{a}^*$ and $\underline{b}^*$ are not parallel to the real space primitive vectors, however, the unit cell mesh is rotated by a 30 degree. Figure A.1(b) shows the 2D unit-mesh in the reciprocal space relative to the real lattice directions.

A.2. Indium (111) surface structure calculations

Indium has face centered tetragonal (FCT) structure with unit cell dimensions a = b = 4.591 Å and c = 4.935 Å at room temperature and atmospheric pressure [4-6]. This structure represents a small distortion of the face centered cubic (FCC) structure with an axial ratio $c/a = 1.0758$. In some cases, the FCT structure of indium is looked at as a body centered tetragonal (BCT). The BCT–FCT relations are: $a_{fct} = a_{bct}\sqrt{2}$ and $c_{fct} = c_{bct}$ [4]. The lattice constants a and c of tetragonal bulk indium showed

temperature and pressure dependence, with the ratio c/a increasing as the pressure

increases. The thermal expansion in the a-axis is found to be larger than that of the c-axis,

resulting in a continuous decrease in the ratio c/a with temperature [5]. Before the

melting point of indium, the ratio c/a was found to be larger than unity i.e. still in the

tetragonal phase. Figure A.2 shows the 111-plane in the FCT tetragonal unit cell of

indium and its extended lattice mesh in real and in reciprocal space.
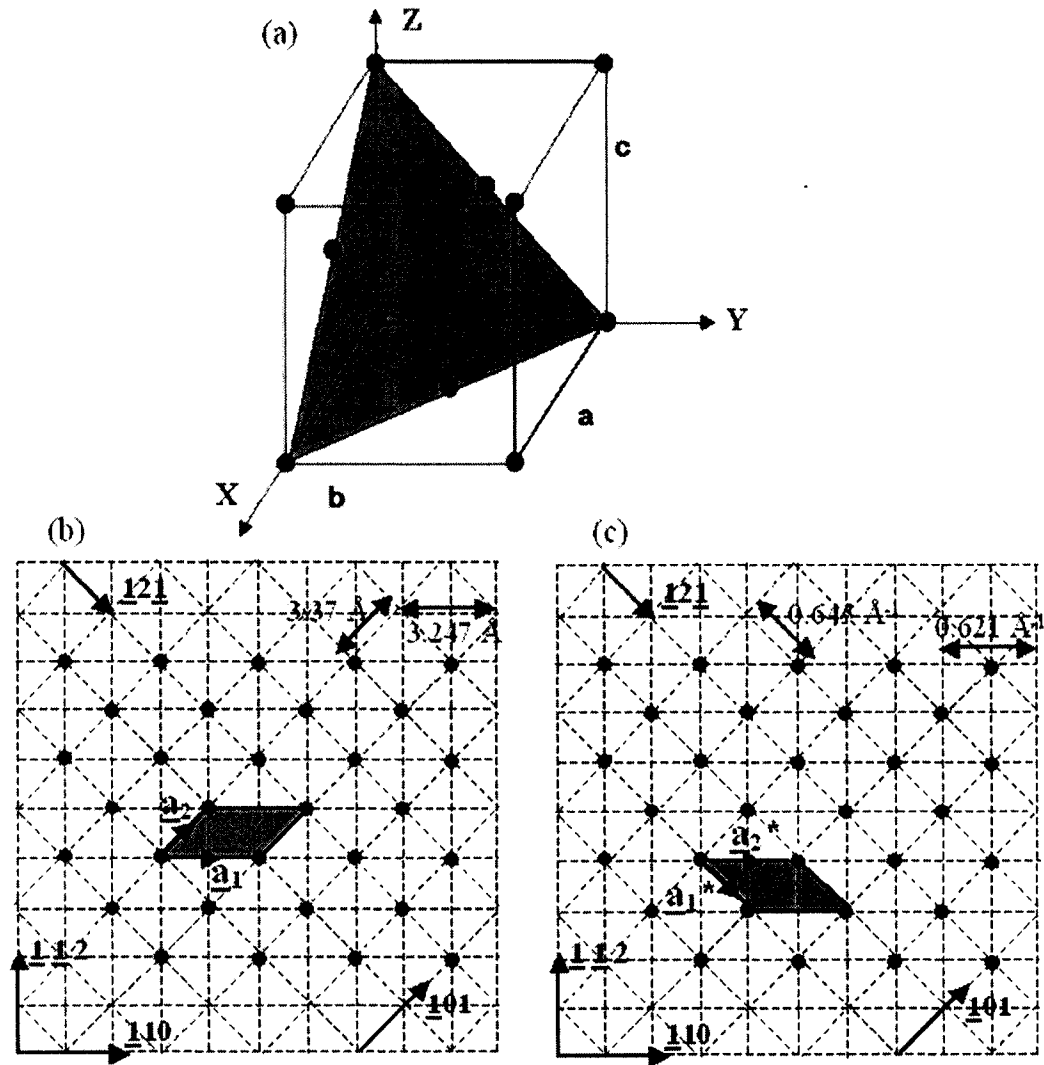
Fig. A.2. (a) The 111 plane in the face centered tetragonal cell of indium [a = b = 4.5912 Å, c = 4.9355 Å and $\alpha = \beta = \gamma = 90$ °]. The extended lattice mesh in the 111-plane and the 2D unit cell in real space (b), and in the reciprocal space (c). Different crystallographic directions are also indicated. The 2D unite cell in the reciprocal space is rotated by a 45° relative to that in the real space.

The unit cell in real space of (111) plane can be constructed using the basic primitive vectors, $\underline{a_1}$ and $\underline{a_2}$, and the unite vector normal to that plane n. These primitive vectors can be found to be,

$$\underline{a_1} = \frac{\sqrt{a^2 + b^2}}{2}[\underline{1}10] = 3.247\,[\underline{1}10],$$

$$\underline{a_2} = \frac{\sqrt{a^2 + c^2}}{2}[\underline{1}01] = 3.370\,[\underline{1}01],\ \text{and}$$

$$\underline{n} = \sqrt{\frac{1}{(a^2 + b^2 + c^2)}}[111] = 0.1226\,[111].$$

The area of the 2D unit mesh can be calculated as,

$$A = \underline{a_1} \bullet (\underline{a_2} \times \underline{n}) = 3.247\,[\underline{1}10] \bullet [3.370\,[\underline{1}01] \times 0.1226\,[111]]$$

$$= [3.247\,[\underline{1}10]] \bullet 0.4132\,[\underline{1}2\underline{1}]$$

$$= 1.3413 + 2.6833 + 0 = 4.0246\ \text{Å}^2$$

$$= 4.0246\ \text{Å}^2$$

The reciprocal vectors $\underline{a_1}^*$ and $\underline{a_2}^*$ can be calculated using the same set of equations used for graphite calculations,

$$\underline{a_1}^* = (2\pi/4.0246)[3.370\,[\underline{1}01] \times 0.1226\,[111]]$$

$$= 0.6447\,[\underline{1}2\underline{1}],\ \text{and}$$

$$\underline{a_2}^* = (2\pi/4.0246)[\,0.1226\,[111] \times 3.247\,[\underline{1}10]]$$

$$= 0.6212\,[\underline{1}\underline{1}0].$$

By calculating the angle between $\underline{a_1}$ and $\underline{a_1}^*$ or between $\underline{a_2}$ and $\underline{a_2}^*$, one can find the direction of the reciprocal lattice vectors relative to those in real space. These calculations indicated that, besides the reduction in the magnitude of the vectors constructing the 2D unite cell in the reciprocal space, the unit cell is also rotated by a 45° relative to that in the real space as shown in Fig. A.2(c).

A.3. Bismuth structure and 002 surface

Bismuth has a non-cubic slightly complicated α-arsenic or *A7* structure similar to group-V semimetal elements such as As and Sb [7,8]. The unit cell is rhombohedral ($a = b = c = 4.75$ Å and $\alpha = \beta = \gamma = 57°$ 14') with two atoms per unit cell, one at the corners (000) and the second located along the body diagonal at (u,u,u) with u = 0.474 Å. This structure can be constructed from the simple cubic lattices by proper distortions [9,10]. Strain the cell along the [111] direction simultaneously with displacement of the basis atoms toward each other in pairs along the same direction until the correct value of the rhombohedral angle α_{rh} is obtained, then inter-displacing or adding another atom along the body diagonal at the correct body location. In fact, the first distortion transforms the simple cube lattices into rhombohedral with one atom per unit cell while the second distortion generates the pseudo-cubic or *A7* structure.

Bismuth structure could be visualized as layered structure in the [111] direction such that each atom has three pyramidal covalent bonds with its three nearest neighbors in one layer and a Van der Waal type force with other three next nearest neighbors in the adjacent layer. Because of this graphite-like layer structural, bismuth symmetry is sometimes described in the hexagonal indices where the [111] is equivalent to [0001] hexagonal direction. In this sense, the hexagonal cell parameters are a = 4.746 Å and c = 11.862 Å with c equal to the 111 diagonal of the rhombohedral unit cell.

The 2D lattice structure of the 100 surface of bismuth in the real and reciprocal space with different crystallographic directions in pseudo cubic notation is shown in Fig A.3. The appropriate 2D unit mish is a diamond cell of 4.75 Å edge length and 57.24°

angle constructed from the unit basic vectors $\underline{a}_1$ = 4.75 [100], and $\underline{a}_2$ = 4.75 [010].

Resolving $\underline{a}_1$, and $\underline{a}_2$ into their components in the orthogonal coordinates gives,

$$\underline{a}_1 = 4.75 \ \underline{x} \text{, and}$$

$$\underline{a}_2 = 4.75 \ [\cos \alpha \ \underline{x} + \sin \alpha \ \underline{y}], \text{ with } \alpha = 57.24°$$

$$\underline{a}_2 = 2.57 \ \underline{x} + 3.994 \ \underline{y}$$

The area of this basic unit mesh can be calculated as,

$$A = \underline{a}_1 . \ (\underline{a}_2 \times \underline{n}) = [(4.75 \ \underline{x})] \cdot [(2.57 \ \underline{x} + 3.994 \ \underline{y}) \times (\underline{z})] = \mathbf{18.9715} \ \text{Å}^2 \cong 18.97 \ \text{Å}^2$$
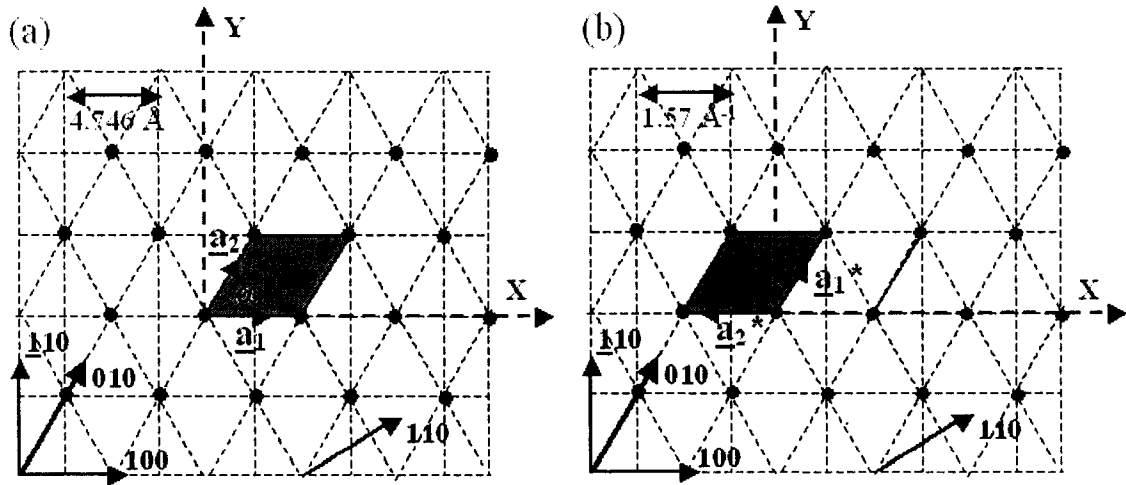
FIG. A.3. Real space structure of the 100- bismuth plane and the different crystallographic direction in a pseudo cubic notation, $\underline{a}_1$ = 4.75 [100] Å, $\underline{a}_2$ = 4.75 [010] Å, α = 57° 14'. The 2D primitive unit cell is counterclockwise rotated by an angle of 57.28° in the reciprocal space relative to that in the real space.

It is easy now to obtain the corresponding basic vectors in the reciprocal space. These

vectors can be obtained as,

$$\underline{a}_1{}^* = (2\pi / 18.97) [(2.57 \ \underline{x} + 3.994 \ \underline{y}) \times (\underline{z})]$$

$$= 1.323 \ \underline{x} - 0.85 \ \underline{y} \text{, and}$$

$$\underline{a}_2{}^* = (2\pi / 18.97) [(\underline{z}) \times (4.75 \ \underline{x})]$$

$$= - 1.57 \ \underline{y},$$

It is clearly notable that $\left|\underline{a}_1^*\right| = \left|\underline{a}_2^*\right| = 1.57$ Å^{-1}, which is inversely related to the magnitude of the basic vectors in the real space. In addition to the magnitude relation of the 2D primitive unite cell in the reciprocal space relative to that of the real space, the unit cell is counterclockwise rotated by an angle of 57.28°, which is clearly notable from $\underline{a}_2^*$ and $\underline{a}_2^*$ directions.

A.4. References

[1]   J.-C. Charlier, J.-P. Michenaud, and X. Gonze "First-principle study of the electronic properties of simple hexagonal graphite," Phys. Rev. B **46**, 4531-4539 (1992).

[2]   F. Atamny, O. Spillecke, and R. Schlögl , "On the STM imaging contrast of graphite: towards a "true" atomic resolution," Phys. Chem. Chem. Phys. **1**, 1, 4113-4118 (1999).

[3]   J.-C. Charlier, J.-P. Michenaud, X. Gonze, and J.-P. Vigneron, "Tight-binding model for electronic properties of simple hexagonal graphite," Phys. Rev. B **44**, 13237-13244 (1991).

[4]   K. Takemura, "Effect of the pressure on the lattice distortion of indium to 56 GPa," Phys. Rev. B **44**, 545-549 (1991).

[5]   V. F. Degtyareva, I. K. Bdikin, F. Porsch, and N. I. Novokhatskaya, "Phase transition in tetragonal In90Pb10 alloy under high pressure: A switch from c/a >1 to c/a<1," J. Phys.: Condens. Matter **15**, 1635-1641 (2003).

[6]   K. Takemura and H. Fujihisa, "High-pressure structural phase transition in indium," Phys. Rev. B **47**, 8456-8470 (1993).

[7]   F. Jona, "Low-energy electron diffraction study of surfaces of antimony and bismuth," Surf. Sci. **8**, 57-76 (1967).

[8]   R. J. Needs, R. M. Martin, and O. H. Nielsen, "Total-energy calculation of the structural properties of the group-V element arsenic," Phys. Rev. B **33**, 3778-3784 (1986).

[9]   X. Gonze, J.-P. Michenaud, and J.-P. Vigneron, " First principle study of As, Sb, and Bi electronic properties," Phys. Rev. B **41**, 11827-11836 (1990).

[10]   G. Jezequel, J. Thomas, and I. Pollini," Experimental band structure of semimetal bismuth," Phys. Rev. B **56**, 6620–6626 (1997).

APPENDIX B

Indexing of transmission RHEED patterns

As mentioned in section III.2.3, transmission RHEED patterns are indexed based on three indices similar to bulk diffraction and selected area electron diffraction (SAED). The following procedure can be used to index transmission patterns of known crystal structure.

- At a certain sample azimuth, taken as a reference point, obtain a diffraction pattern.

- Take the origin-transmitted spot to be the (000) point.

- Measure the distance to the origin, (000) point, in mm for three spots closest to the origin.

- Graphically, measure the angles between the selected three spots.

- Convert the measured distances into d-values using the calculated electron wavelength and the value of L, the sample to screen distance, in Eq. 3.13.

- Assign Miller indices to each spot by comparing the measured value to those of the single crystal. There might be more than one set of hkl assigned for a single spot.

- Based on the uncertainty in the measurement and the camera constant calibration, assign an error range in measuring d, Δd, and take all theoretical values situated between d $_{measured} \pm \Delta d$.

- From the assigned hkl indices of the spots, calculate the angle between these spots, α_{ij}, using the dot product rule, $\alpha_{ij} = cos^{-1} \dfrac{\overline{a}_i \bullet \overline{a}_j}{|a_i| \cdot |a_j|}$.

- Compare the measured and calculated angles, and assign the correct *hkl* indices.

- Determine the zone axis [*uvw*] from any two knowing [*hkl*] vectors within the diffracted zone such that $u = k_1l_2 - k_2l_1$, $v = l_1h_2 - l_2h_1$, and $w = h_1k_2 - h_2k_1$.

- Continue indexing the other spots within the diffraction pattern taking advantage of the crystal symmetry and making sure that the indices must satisfy the zone equation, Eq. (3.16).

- The same procedure can be followed for any other diffraction zone or azimuth orientation.

In the following sections, the diffraction pattern obtained for graphite and indium will be indexing according to the abovementioned procedure.

B.1. Graphite

Figure B.1 shows the obtained RHEED pattern, in its transmission mode, of a cleaned graphite surface. The spot in the diffraction pattern are labeled to allow us to refer to. The first step in pattern indexing is to measure the distances to the origin, in cm, for several spots closest to the origin. In case of digital images a conversion factor from cm-to-pixel is needed. This can be done by obtaining an image for two-marked points, with known separation distance, placed at the screen. The cm-to-pixel conversion is then the ratio of the distance between the two marks in the real and that in the image. Using an image of a graph paper is normally the best way to do this conversion. This calibration resulted in a calibration factor of 66.917 pixels/cm and 83.885 pixels/cm for the horizontal and the vertical directions respectively. This calibration factor might vary depend on the camera-to-screen distance and the camera zoom adjustments. Because of

the non-uniform pixel-to-cm ratio, the vector distances can't be transferred from pixels to mm directly. However, the vertical and horizontal components are first obtained then independently factored to cm units, and finally the distance in cm can be found. The measured d-values of the vectors are then compared to that generated for a single crystal graphite. A web-based software, "emaps" is used to generate a detailed list of *hkl* versus standard d-values of graphite [1]. It is found to be more convenient to consider positive indexing, since the negative sign will not affect the d-value as it is clearly observed from the detailed calculated d-list. A full version of "CaRIne" software can be used to generate the same list using $a_0 = 2.44$ and $c_0 = 6.71$ Å as cell parameters [2].
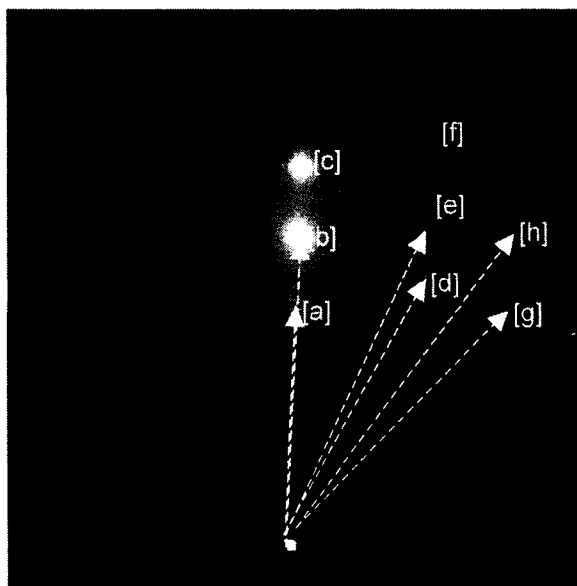
FIG. B.1. Transmission RHEED pattern of clean graphite surface, an accelerating voltage of 9.7 keV and filament current of 2.65 A were used to obtain this pattern. The spot are labeled alphabetically to make it easy to refer to. The first step in indexing this pattern is to measure the distances from the origin to some spots and the angles between them.

The measured d-values and the assigned *hkl* sets are listed in Table B.1. Since Bragg's low contains *n*, the interference order or integer, the calculated d-values is considered as (d/n) i.e. the n-multiple of the measured values are taken into

considerations. In order to eliminate the wrong indexing and nominate only the correct *hkl* set, the angles between the predicted *hkl* sets for [a] and [b] is calculated and compared to the measured angles. It is clear that the spots, [a] and [b] are on the same straight line i.e. making a zero angle. Therefore, the first step to correctly index them is to look carefully in the predicted *hkl* sets and figure out which of these sets making zero angle with each other. This means finding two *hkl* sets whose planes are parallel and can be written as $(hkl)_1 = \beta (hkl)_2$ where β is an integer. From the table, the only sets that satisfy this criteria are 007 and 005 where both sets can be written in terms of 001 with β equal to 7 and 5 respectively. It might not be obvious to recognize the angles between the planes from their *hkl* values, hence, one might generate a table of the angles between the different *hkl* sets of [a] and those of [b] then do the eliminations and correct indexing. Note that 006 is among the predicted indices of the [c] spot and also it belongs to the same family. Since all *00l* are parallel planes, then the correct indexing might be 002, 004, and 006. This is more convenient for systematic indexing because of the spot arrangements and the pattern symmetry.

Based on the final indexing of the spots [a], [b] and [c], it is clearly that the direction normal to the substrate surface represents the z-direction. Therefore each spot on the side rods should have *l* value based on its horizontal distance from the 000-horizontal line. This implies that the [d]- and [e]-spots must have indexing of *l* equal to 3 and 4 respectively. One might starts to calculate the zone axis using the 002 and any *hkl* predicted set of the [d] spot and check which of the [e] predicted sets that satisfy the zone equation. Keep forming combinations of 002 and all the other predicted *hkl* sets [d] and test it with those predicted for [e]. Performing these steps left us with two zone axis

possibilities <$\underline{1}$10> and <$\underline{1}$00> with possible spot indexing for [d] to be either 103 or 104

and for [e] to be either 113 or 114. Using these two zone axis with the predicted *hkl* sets

of [g] spot reveals that <100> is not a valid zone axis and so as the 103 and 104 indexing.

On the other hand, the zone equation is verified when using 113 and 114 indexing and,

hence the possible indexing of [g] spot either 220, 110, or 221. It is also clear that 226 is

a valid indexing of the [h] spot among all possibilities.

Table B.1. Comparison between the measured and the calculated d-values of graphite and its possible *hkl* sets. The stander d-values list is generated using a web based software [1]. The sample-to-screen distance is 17.3 cm and the electron wavelength is 0.1237 Å.

#	Experimental		Calculated	*h k l*
	(d)	**(2d)**		
[a]	0.955	1.910	0.963, 0.959 2.033	2 0 3, 2 2 3, 0 2 3, **0 0 7**, 1 0 1, 1 1 1, 0 1 1, 1 0 2, 1 1 2, 0 1 2
[b]	0.709	1.418	0.713, 0.711 0.707, 0.704 0.696, 1.342 1.318	2 0 7, 2 2 7, 0 2 7, 3 0 0, 3 3 0, 0 3 0, 3 0 1, 3 3 1, 0 3 1, 1 0 9, 1 1 9, 0 1 9, 3 3 2, 2 1 8, 1 1 8, 1 2 8, **0 0 5**, 1 0 4, 0 1 4, 1 1 4, 3 1 3, 2 2 4, 1 2 8, 2 1 8, 3 0 2
[c]	0.578	1.155	0.581, 0.578 1.157, 1.136 1.119	3 1 8, 3 2 8, 2 1 8, 2 3 8, 1 2 8, 1 3 8, 4 2 4, 2 2 4, 2 4 4, 4 1 3, 4 3 3, 3 1 3, 1 3 3, 3 4 3, 3 0 7, 3 3 7, 0 3 7, 2 1 2, 1 1 2, 1 2 2, 1 0 5, 1 1 5, 0 1 5, **0 0 6**,
[d]	0.765	1.532	0.756, 0.758 0.772, 1.544	2 1 7, 1 1 7, 1 2 7, 3 1 3, 3 2 3, 2 1 3, 2 3 3, 1 2 3, 1 3 3, 2 0 6, 2 2 6, 0 2 6, **1 0 3**, **1 1 3**, **0 1 3**,
[e]	0.673	1.345	0.691, 0.677 0.671, 0.659 1.342, 1.318	3 1 5, 3 2 5, 2 1 5, 2 3 5, 1 2 5, 3 0 3, 3 3 3, 0 3 3, 0 0 10, 2 0 8, 2 2 8, 0 2 8, **0 0 5**, **1 0 4**, **1 1 4**, 0 1 4
[g]	0.757	1.510	0.772, 0.758 0.756, 1.544	2 0 6, **2 2 6**, 0 2 6, 3 1 3, 3 2 3, 2 1 3, 2 3 3, 1 2 3, 1 3 3, 2 1 7, 1 1 7, 1 2 7, **1 0 3**, **1 1 3**, **0 1 3**, 1 0 5
[h]	0.620	1.239	0.6280, 0.6178 1.318, 1.232 1.211	3 0 5, **3 3 5**, 0 3 5, 3 1 7, 3 2 7, 2 1 7, 2 3 7, 1 3 7, 1 2 7, 1 0 4, 0 1 4, **1 1 4**, 2 1 0, **1 1 0**, 1 2 0, 2 1 1, 1 1 1, 1 2 1,

Based on the pattern symmetry, the correct and consistence indexing of the obtained graphite pattern is shown in Fig. B.2. The pattern is a cut through the 3D reciprocal lattice of graphite as the electron beam passes through direction parallel to the axis of the 110-zone. The pattern can be seen as a line of spots arranged in the n.l order with $h = k = n$. Figure B.3 gives a selected area diffraction pattern (SADP) simulation of graphite. The simulation was designed such that the electron beam is parallel to 110-direction, x-axis is parallel to 110-direction, 300 kV electron potential, and zero tilt angle in both x-and y-directions. Apparently, the obtained RHEED pattern is similar to the upper half of the SADP simulation pattern with h replaced by $-h$.
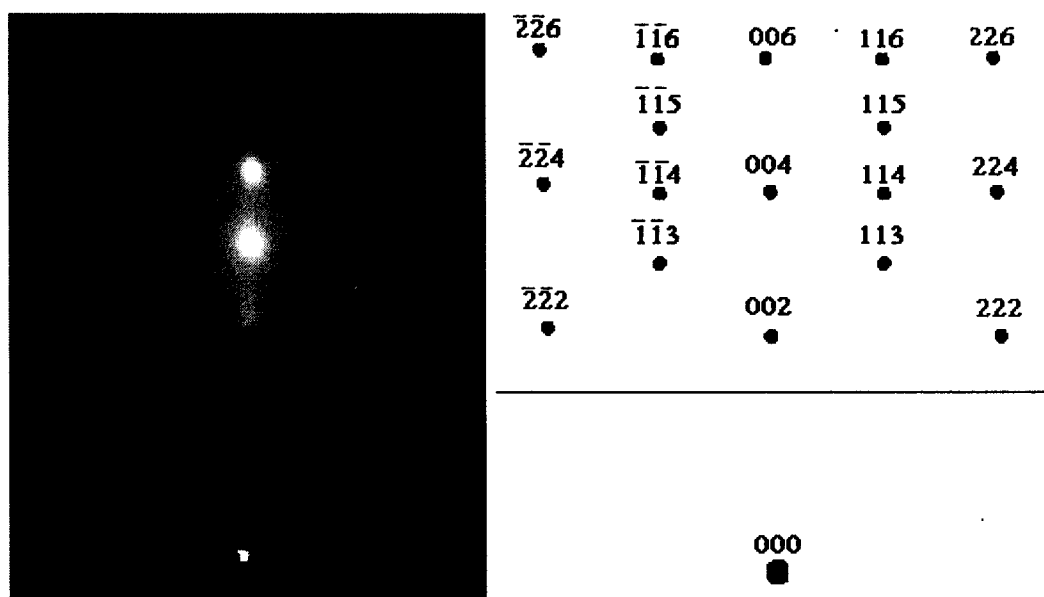
FIG. B.2. Transmission RHEED pattern of clean graphite surface and its interpretation, the pattern represent a cut through the 3D reciprocal lattice of graphite as the electron beam passes through direction parallel to the axis of the 110-zone. It is clearly that the vector [002] is normal to the substrate surface. The pattern can be seen as a line of spots arranged in the n.l order with $h=k=n$. The 1.l rods seem to have spots with lower intensity than 2.l rod.

0,0,8

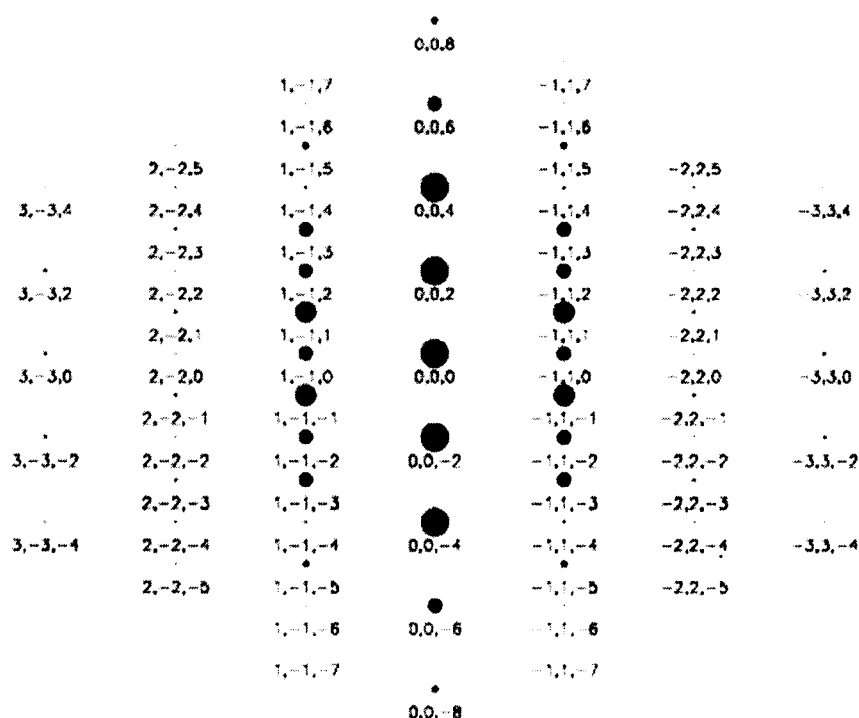| | | 1,-',7 | | -1,',7 | |
		1,-',6	0,0,6	-1,',6	
2,-2,5	1,-',5		-1,',5	-2,2,5
3,-3,4	2,-2,4	1,-',4	0,0,4	-1,',4	-2,2,4	-3,3,4
	2,-2,3	1,-',3		-1,',3	-2,2,3	
3,-3,2	2,-2,2	1,-',2	0,0,2	-1,',2	-2,2,2	-3,3,2
	2,-2,1	1,-',1		-1,',1	-2,2,1	
3,-3,0	2,-2,0	1,-',0	0,0,0	-1,',0	-2,2,0	-3,3,0
	2,-2,-1	1,-1,-1		-1,1,-1	-2,2,-1	
3,-3,-2	2,-2,-2	1,-1,-2	0,0,-2	-1,1,-2	-2,2,-2	-3,3,-2
	2,-2,-3	1,-1,-3		-1,1,-3	-2,2,-3	
3,-3,-4	2,-2,-4	1,-1,-4	0,0,-4	-1,1,-4	-2,2,-4	-3,3,-4
	2,-2,-5	1,-1,-5		-1,1,-5	-2,2,-5	
		1,-1,-6	0,0,-6	-1,1,-6	
		1,-1,-7		-1,1,-7	

0,0,-8

FIG. B.3. Selected area diffraction pattern (SADP) simulation of graphite. The in put simulation parameters are: 110 is the zone axis, x-axis is taken to be parallel to 1$\bar{1}$0-direction. The spot diameter is related to its simulated and expected intensity.

B.2. Indium

Indium showed diffraction RHEED patterns that are combination of reflection and transmission. Figure B.4. shows RHEED pattern of 16 ML indium film deposited at room temperature. The pattern can be seen as transmission spots arranged in rods normal to the surface with spots as if they are located on a circumference of Laue rings. However, the indexing can be made in a transmission manner similar to that of graphite in the above section. The only difference is the presence of double spots in the rods next to the 00 rod. Double spot diffractions normally results from overlapping of two crystals or grains whose lattice parameters are slightly different such as a precipitate embedded in a matrix, thin film on a substrate, lamellar twin, or thin foil that heavily bent and curved onto itself.
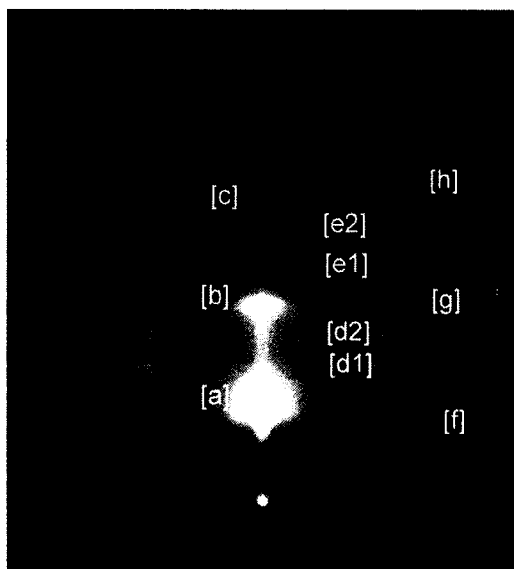
FIG. B.4. Transmission RHEED pattern of 16 ML indium film deposited at room temperature. The pattern can be seen as transmission spots arranged in rods normal to the surface with spots as if they are located on a circumference of Laue rings. The spot are labeled to be easy to refer to.

The distances to the origin, in cm, for several spots closest to the origin are measured and compared to that calculated using the standard cell parameters of indium. The calculated d-values and its *hkl* indices of the tetragonal indium are given in appendix B as calculated using "emaps" software [52]. The measured d-values and the possible *hkl* sets as compared to the calculated values are listed in Table B.2. The comparison gives rise to only one possible indexing of the spot [a], which is 002. This makes the indexing of the other spots on the same rod, [b] and [c], easy. Remembering that the angle between the vectors from the origin to the spots [a], [b], and [c] are zeros, this contains the possible indexing sets in the {00*l*} sets. Therefore, the elected indexing of the spots [a], [b], and [c] is 002, 004, and 006, respectively.

Table B.2. Comparison between the measured and the calculated d-values of indium and its possible *hkl* sets. The stander d-values list is generated using a web based software [52]. The sample-to-screen distance is 17.3 cm and the electron wavelength is 0.13232 Å.

#	Experimental		Calculated	*h k l*
	d	2d		
[a]	2.482	4.965	2.46	**0 0 2**
[b]	1.215	2.430	1.23, 1.19, 2.46	**0 0 4**, 1 3 2, 0 0 2
[c]	0.804	1.608	0.82, 0.811, 0.801, 0.790, 0.784, 1.62	**0 0 6, 3 0 5, 0 4 4,**1 5 2, 1 1 6, 2 5 1, 3 3 4, 0 2 2
[d1]	1.496	2.993	1.533, 1.527,1.382, 1.366, 3.05	1 0 3, **2 2 0,**0 3 1, 1 3 0,**1 1 0**
[d2]	1.241	2.482	1.25, 1.23, 2.46	1 2 3, 0 0 4, 0 0 2
[e1]	0.949	1.900	0.965, 0.959, 0.957, 0.940, 0.914,1.91	2 4 0, 1 0 5, **2 2 4,** 3 3 2, 1 3 4,**1 1 2**
[e2]	0.843	1.686	0.85, 0.84, 0.82, 1.798, 1.623	3 4 1, 0 5 1, 1 5 0, 0 0 6, 1 2 1, 0 2 2
[f]	1.257	2.514	1.29, 1.25, 1.23, 2.46	**2 2 2, 1 2 3,** 0 0 4,0 0 2
[g]	0.890	1.781	0.940, 0.914, 0.899, 0.876, 0.850,1.915 1.798,1.62	**3 3 2,** 1 3 4, 2 4 2, 1 4 3, 3 4 1, 0 5 1 **112,** 1 2 1, 0 2 2
[h]	0.699	1.399	0.722, 0.720,0.717, 0.709, 0.697, 0.693, 0.691,0.683, 1.382, 1.366	**2 2 6,** 2 5 3, 0 6 0, 1 4 5,3 5 2,3 1 6, 1 6 1,1 5 4, 1 0 7, 0 6 2, 2 6 0,0 3 1, 1 3 0

Because of the expected shrinking/expansion in the d-value of plains causing the double spot, it is better to start indexing the spots [f], [g], and [h]. Either 002 or 004 is a valid indexing of the spot [f]. This leave us with only two other possibilities; 222 and 123 and hence two zone axis<110> and <210>. Using the zone equation to test the predicted sets for [g] gives 332 and 112 when <110> is used and 242 and 121 when <210> is used. Going further by testing these zones matches with the predicted sets of [h] eliminates the <210> since none of the sets satisfy its equation. On the other hand, using the <110> axis show that 226 is a valid indexing of [h]. In other words, the correct indexing of the spots

[f], [g], and [h] is 222, 224 and 226 respectively. Using a systematic indexing, the twin

spots [d], and [e] can be indexed as 11*l* where *l* is the horizontal distance from the 000.

The transmission-RHEED pattern of indium and its corresponding 3D indexing is

shown in Fig. B.5. Also, an SADP simulation pattern of the tetragonal indium with the

electron beam parallel to 110-direction, x-axis is parallel to 110-direction, 300 kV

electron potential, and no tilting in the x-and y-directions is presented in Fig. B.6. The

lower half of the SADP simulation pattern looks similar to the obtained RHEED pattern

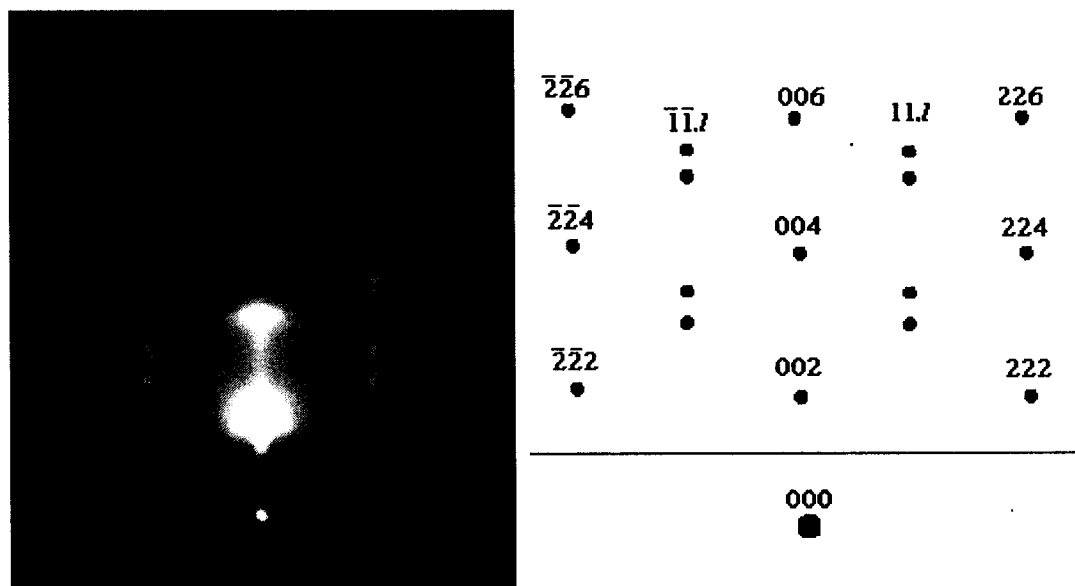of indium except at the 11*l*, twinning direction.

FIG. B.5. Transmission RHEED pattern of indium and its corresponding indexing. The indexing indicates that the electron beam is passing parallel to the 110 direction and the pattern is a 3D cut of the indium reciprocal lattice taken in the 110-zone. The indexing also shows that the nanocrystals have twinning in the 11*l* direction.
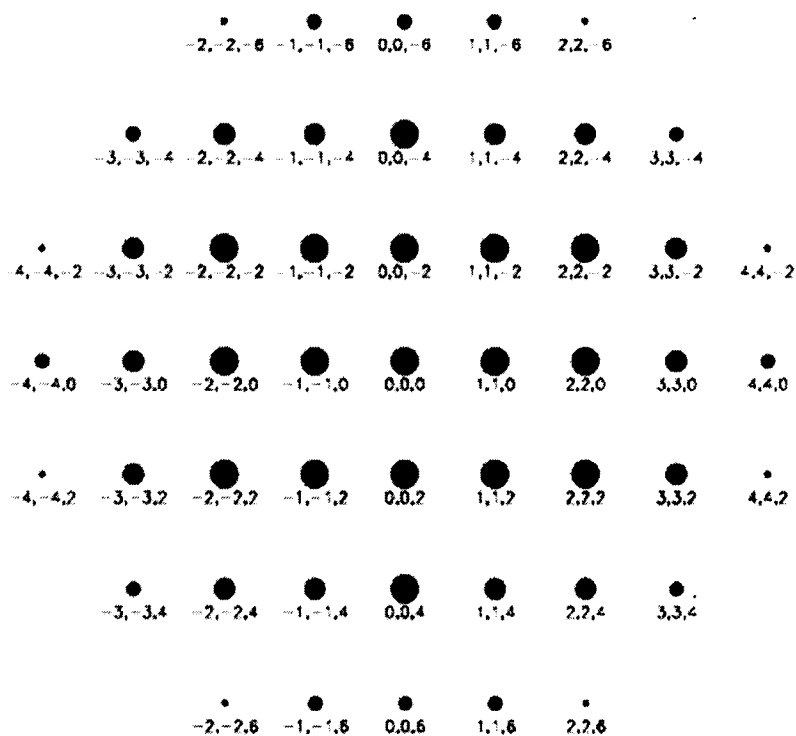
FIG. B.6. Selected area diffraction pattern (SADP) simulation of Indium. The spot diameter is related to its simulated and expected intensity.

References

1.   J.M. Zuo, J.C. Mabon, WebEMAPS software, University of Illinois at Urbana - Champaign; URL: http://emaps.mrl.uiuc.edu/

2.   CaRIne Crystallography software, C. Boudias and D. Monceau 1989-1998, Centre de Transfert, F-60200 Compiegne, France.

APPENDIX C

The ultrahigh vacuum system

The ultrahigh vacuum (UHV) chamber used in this work is a six-way 8-inch stainless steal chamber. RHEED gun, RHEED screen, homemade evaporator, and XYZ-manipulator are assembled to four ports of it, while the other two ports are used to connect the vacuum pumps and other accessories. Fig. C.1 shows a schematic illustration of the main components of the used system. Nanocrystals preparations and RHEED studies were performed after reaching a UHV of base pressure better than mid $\times 10^{-9}$ Torr.
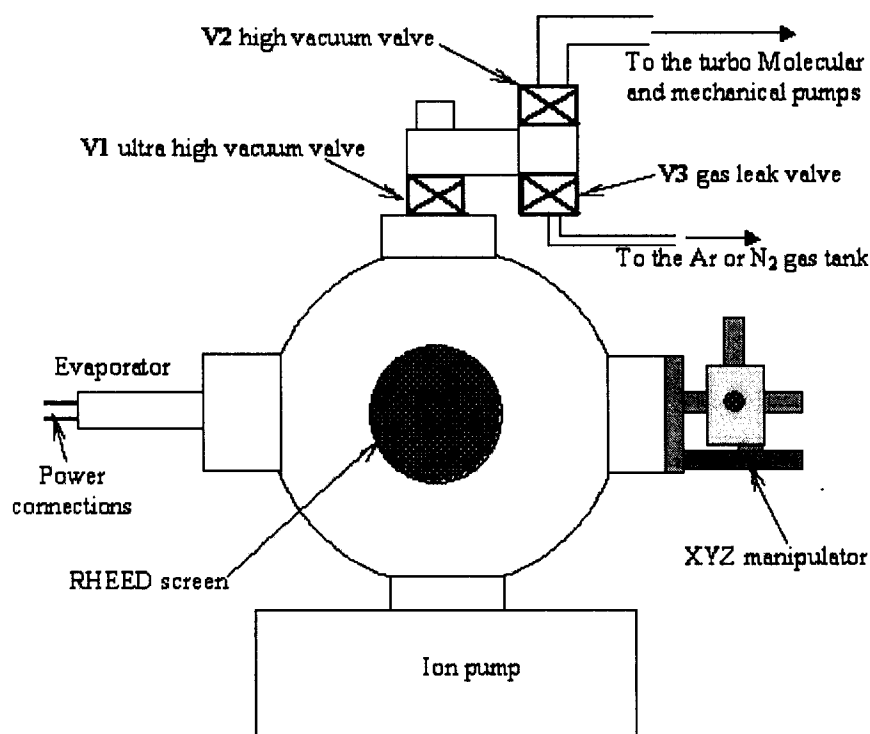
FIG. C.1. A schematic illustration of the used system.

C.1. Pumping the system down

1. Start up the mechanical pump and a few minutes later turn on the turbo molecular pump.

2. Make sure that V1 and V2 are opened and V3 is closed.

3. For better operation, make sure that the exhaust hose of the mechanical pump is not pended in anywhere.

4. Leaving the turbo pump packed by the mechanical pump working for couple of hours till the pressure decreases to a value between the mid to the low 10^{-7} Torr.

5. After reaching such vacuum, one might start bake the system for about 4-8 hours at a temperature between ~120 160° C.

6. After cooling the system to room temperature, 3-6 hours, close V1, and then start the ion pump.

7. Turn off the turbo pump and then the roughing pumps after making sure that the ion pump starts working properly.

8. Within 12-24 hours, the system should reach a value between mid and low 10^{-9} Torr and the vacuum will improve with time.

C.2. Opening the system

1. Shut off the ion pump and turn on the roughing pump followed by turning the turbo pump on while V1 is closed.

2. After reaching a considerably low pressure in the region above V1, open V1 gradually.

3. After a few minutes, close V2 and turn off the turbo and mechanical pumps.

4. Use V3 to allow a very small rate of argon or N_2 gas to get into the chamber.

5. Stop argon flow when the pressure inside the chamber reaches low 10^{-2} Torr. Do not over pressurize the chamber.

6. Open the chamber gradually and allow a gradual balance between the pressure inside and outside the chamber.

APPENDIX D

Image capture and analysis

Charged coupled devise (CCD) camera is used to capture the RHEED images. The camera is controlled through KSA300v5 software operated using a DOS operating system. An upgrade of this KSA, KSA400v5, is used for data analysis. Below is a step-by-step procedure to capture and perform analysis for RHEED pattern.

D.1. Focusing the camera

1. Restart the computer controlling the camera in MS-DOS mode, and run the KSA300v5 program by typing the command "cd\rheed" then hit enter and "ksa300v5" then hit enter twice.

2. From the header menu of the program select "(D)isplay\(p)assthru"

3. The camera monitor will show a black video of the captured view of the camera. An indirect faint light source can be used to help find the best image.

4. Use the telescope lens (in the camera) to adjust the aperture opening and the focus. Also, you may move the camera back and forth until the best image is obtained.

D.2. Image capture

The KSA 400 is an integrated hardware and software system designed for the acquisition, archiving, and analysis of RHEED and LEED diffraction patterns. Images can be captured manually as a single image or automatically as multi-image acquisition.

Single image mode

1. From the (A)cquistion menu, select "Single Image mode", then hit enter.

2. Select the integration time you want, based on the image quality, as integer numbers of (1/30) sec

3. After hitting enter twice, the captured image will appear on the monitor and the program will ask you if you want to save the image. Type Y, for yes, and N, for no.

4. Repeat the above steps for capturing another image.

Multiple-image mode

1. From the (A)cquistion menu, select "Multiple   Image mode", then hit enter.

2. Select the number of images, integration time, delay time between images, and final base name.

3. After hitting enter, the program will capture the image and save them automatically in the specified subdirectory.

D.3.   Image analysis

Line scan and spot profile

1. Run the program and open the image to make it the currently activated image.

2. Select Line Profile from the Analysis menu. A line will appear on the image, also a corresponding plot of the line profile as shown in Fig. D.1 will open in another window.

3. Move the line by dragging it with the mouse. As you move the line, the line profile is automatically updated. By dragging the ends of the line, the orientation and length of the line may be changed.

4. A specific line length, position, and angle may be specified by double clicking on the line, or right clicking the line and selecting Properties.

5. Any number of line profiles may be displayed on a given image.

6. The line profile plot may be copied to the Clipboard (by selecting Edit/Copy or <Ctrl-C>). Alternatively, the line profile data may be stored to an ascii-text file by selecting "Export" from the "File" menu to export the chart.
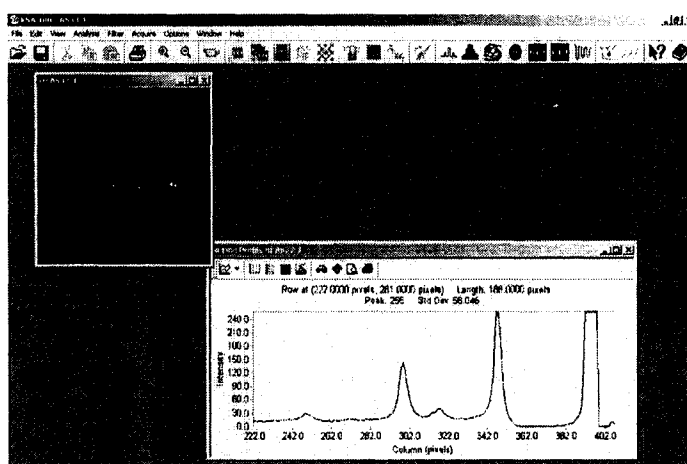

FIG. D.1. Typical line scan analysis window using KSA400 software. For the line length and position, one might drag the line it self or use the line "Properties" options.

Measuring the FWHM

This operation may be used to analyze both static diffraction images and movies.

1. Open the image to be analyzed.

2. Select the "FWHM/coherence length" from the "Analysis" menu.

3. The software will show a 2D graph of the FWHM versus the pixel number within the specified square. Drag the square to the spot location and/or use the "Properties" option of the square to make it coincide with the spot.

4. Measuring the FWHM of any RHEED spot can also be performed manually from the line scan across the spot.

D.4. Recording the temperature

The temperature is measured using a HH506R digital thermometer, which is compatible with either K, J, R temperature sensors. The device is interfaced with the computer through an RS 323-C optical interface. Very simple software is used to acquire the temperature data (one reading per sec minimum) and sort them in an Excel work sheet.

D.5. Semi-automated melting and solidification data collection

By synchronizing the image and the temperature acquiring while controlling the heating rate, two independent files can be extracted to relate the image and the temperature during the melting and solidification experiment in a semi-automated data collection. The heating and cooling rates must be controlled such that the total size of the acquired images during the experiment does not exceed the available space on the computer. Also, the time delay between accusations must be higher than the minimum time necessary to store the file, either temperature reading or RHEED image, on the computer. This time must be larger than 2 seconds. In case of no further analysis on the image is required, measuring the intensity of a particular spot during the experiment is efficient.

CURRICULUM VITAE
For
MOHAMED K. ZAYED

DEGREES:

Master of Science (Physics), Cairo University, Bani-Suef, Egypt, 1997

Bachelor of Science (Physics), Cairo University, Bani-Suef, Egypt, 1992

PROFESSIONAL CHRONOLOGY:

Department of Electrical and Computer Engineering, Old Dominion University, Norfolk, Virginia,
Research assistant, April 2000 – present
Department of Physics, Cairo University, Bani-Suef, Egypt
Assistant lecturer, November 1992 – present

HONORS AND AWARDS:

Doctoral dissertation stipend Award, Old Dominion University, 2005.

Dr. Stuart H. Russell memorial scholarship, Collage of engineering, Old Dominion University, 2003-2004.

Dr. Yahya Elsayed Award, Physics Department, Cairo University, Bani-Suef, Egypt, 1992-1993.

PUBLICATIONS

M. K. Zayed and H. E. Elsayed-Ali, "Melting and solidification of asdeposited and recrystallized bismuth nanocrystals," (in preparation).

M. K. Zayed and H. E. Elsayed-Ali, "Condensation on (002) graphite of liquid bismuth far below its bulk melting point," accepted in Physical Review B.

M. K. Zayed and H. E. Elsayed-Ali, "Melting behavior of asdeposited and recrystallized indium nanocrystal," Thin Solid Films 489, 42-49 (2005).

M. K. Zayed, M. S. Hegazy and H. E. Elsayed-Ali, "Melting and solidification of indium nanocrystals on (002) graphite," Thin Solid Films 449, 254-263 (2004).

S. A. El-Hakim, S. A. Nasser, H. H. Afify, and **M. K. Zayed**, "Characterization of cupper-zinc oxide films prepared by spray pyrolysis for gas sensing applications," The XXI conference on solid state science & workshop on silicon technology in Optoelectronics, Mansoura, Egypt. Feb-1999.

S. A. Nasser, H. H. Afify, S. A. El-Hakim, **M. K. Zayed**," Structural and physical properties of sprayed copper–zinc oxide films," Thin Solid Films 315, 327 (1998).